

NASA
TM
X-65952
c.1(1)

LOAN COPY: RETURN TO
AFWL TECHNICAL LIBRARY
KIRTLAND AFB, N. M.

X-524-72-125

REF ID: A65952

NASA TM X 65952



RESULTS OF THE BALLOON
ATMOSPHERIC PROPAGATION
EXPERIMENT FLIGHTS OF 1970
(BAPE I)

PETER O. MINOTT
JACK L. BUFTON
MICHAEL W. FITZMAURICE

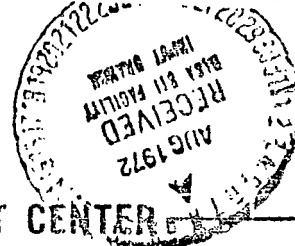
(NASA-TM-X-65952) RESULTS OF THE BALLOON
ATMOSPHERIC PROPAGATION EXPERIMENT FLIGHTS
OF 1970 (BAPE I) P.O. Minott, et al (NASA)
Mar. 1972 130 p CSCL 04A

N72-28354

Unclas
36046

G3/13

MARCH 1972



GODDARD SPACE FLIGHT CENTER
GREENBELT, MARYLAND





0152420

X-524-72-125

RESULTS OF THE BALLOON
ATMOSPHERIC PROPAGATION
EXPERIMENT FLIGHTS OF 1970
(BAPE I)

Peter O. Minott
Jack L. Bufton
Michael W. Fitzmaurice

March 1972

GODDARD SPACE FLIGHT CENTER
Greenbelt, Maryland

PRECEDING PAGE IS NOT FILMED

ACKNOWLEDGEMENTS

The work described in this report is the result of the joint efforts of the Laser Data Systems Branch of Goddard Space Flight Center, Sylvania Electronic Systems Western Division, and the Air Force Cambridge Research Laboratories of Laurence G. Hanscom Field. The experiment was funded by the Guidance and Optics Branch, Guidance Control and Information Systems Division, of the NASA Office of Advanced Research and Technology. Mr. Henry L. Anderton, Chief of the Guidance and Optics Branch, initiated the experiment and has followed it through to completion.

The experiment was the result of a proposal submitted by Sylvania Electronic Systems Western Division to the Office of Advanced Research and Technology. Mr. Arthur Kraemer, Dr. Paul J. Titterton, Mr. Tom Mulcahy, and Mr. Scott Overstreet were the principal authors of this proposal.

The experiment was performed jointly by the Laser Data Systems Branch of Goddard Space Flight Center, which provided the ground tracking system, and reduced the data; Sylvania Electronic Systems, which built the balloon payload and maintained it during the experiment; and the Balloon Research and Development Test Branch of Air Force Cambridge Research Laboratories, which provided the balloon launch facilities and services for the experiment.

Design of the balloon payload was performed under the direction of Dr. Douglas Woodman. Other major contributors to the design were Mr. Scott Overstreet, Mr. Clyde Brown, Mr. Connell Ward, and Mr. Michael Galus. Dr. J. Richard Kerr of the Oregon Graduate Center acted as program consultant.

Balloon launch services were provided by the Balloon Research and Development Test Branch through the office of Mr. Thomas Danaher at Air Force Cambridge Research Laboratories, Laurence G. Hanscom Field, Bedford, Mass. Detachment 1 of the Balloon Research and Development Test Branch under the command of Lt. Col. Robert J. Reddy at Holloman Air Force Base, New Mexico, performed the actual balloon launch and recovery operations. Members of his staff who were major contributors to the experiment were Mr. Glenn Richards and Captain Donald Brooks, who provided Hason and handled the launch preparations; Mr. Duke Gildenberg, who was responsible for meteorological support and navigation; and Major J. Koehly, who was launch officer on several of the flights. The authors also wish to express their thanks to Mr. Tenney

and Mr. Robert Blankenship, launch and recovery crews, for their work in handling the experiment payload.

Design and construction of the ground tracking station, and data analysis were performed by the authors. Members of our staff who deserve special note are Mr. Calvin Rossey for design of the ground tracking mount, Mr. Frank Dooley for design of the transmitter opto-mechanical system, and Mr. William Schaefer for design of the ground tracking mount servo system. Mr. David Grolemond and Mr. John Larmer of Bendix Corporation were also major contributors to the maintenance and operation of the ground station in the electro-optical systems area.

The authors would like to express their appreciation to Mr. Walter Carrion, Chief of the Laser Data Systems Branch, Dr. Henry Plotkin, Associate Chief of the Advanced Development Division, and Dr. Robert Coates, Chief of the Advanced Development Division, for their assistance and support throughout the experiment.

TABLE OF CONTENTS

<u>Paragraph</u>		<u>Page</u>
SECTION 1		
INTRODUCTION		
SECTION 2		
SUMMARY		
SECTION 3		
DESCRIPTION OF EQUIPMENT		
3.1	BAPE PAYLOAD	3-1
3.1.1	GENERAL DESCRIPTION OF PAYLOAD	3-1
3.1.2	ELEVATION AXIS AND OPTICAL DETECTOR SYSTEMS	3-5
3.1.3	QUADRANT STAR TRACKER	3-6
3.1.4	ATTITUDE STABILIZATION SYSTEM	3-11
3.1.5	GONDOLA	3-12
3.2	THERMOSONDE	3-16
3.3	FLIGHT VEHICLE	3-18
3.3.1	BALLOON CHARACTERISTICS	3-18
3.3.2	LOAD BAR AND RIGGING	3-21
3.3.3	EXPERIMENT SITE AND FLIGHT PROFILE	3-21
3.4	GROUND TRACKING STATION	3-29
3.4.1	LASER TRANSMITTER SYSTEM	3-29
3.4.2	TRACKING MOUNT	3-39
3.4.3	TELEMETRY, PAYLOAD COMMAND, AND DATA RECORDING SYSTEM	3-43
	REFERENCES	3-49
SECTION 4		
CHRONOLOGY OF EXPERIMENT		
SECTION 5		
DATA REDUCTION		
5.1	THERMOSONDE DATA	5-1
5.2	METHOD OF OPTICAL DATA REDUCTION	5-4

TABLE OF CONTENTS (Cont)

<u>Paragraph</u>		<u>Page</u>
5.3	OPTICAL DATA POINTS	5-6
SECTION 6		
DATA ANALYSIS		
6.1	VERTICAL PROFILE OF TURBULENCE	6-1
	REFERENCES	6-8
6.2	LOG-AMPLITUDE VARIANCE AND SCINTILLATION	6-9
	REFERENCES	6-22
6.3	CORRELATION COEFFICIENT	6-23
	REFERENCES	6-35
6.4	APERTURE AVERAGING OF SCINTILLATION	6-36
	REFERENCES	6-38
6.5	AUTOCORRELATION OF IRRADIANCE AND POWER SPECTRAL DENSITY*	6-39
	REFERENCES	6-46
SECTION 7		
CONCLUSIONS		
APPENDIX A		
UPPER A.R. DATA		
APPENDIX B		
EVALUATION OF LOG-AMPLITUDE CORRELATION COEFFICIENT		

*Data processed only for the argon wavelength.

1. INTRODUCTION

The intensive study of electromagnetic wave propagation through turbulent mediums began in the early 1950's. The first work of significance was performed in Russia by Kolmogorov¹, Chernov², and later Tatarski³. Although a great deal of work in this area was performed in the United States, intensive study did not begin until the early 1960's. One of the major driving forces which spurred interest in wave propagation through a turbulent medium was the advent of the laser, with its promise of data transmission bandwidths many orders of magnitude higher than possible with the highest frequency microwaves.

Although initially there was some interest in high-data-rate transmission between points on the earth's surface, it soon became apparent that the effects of weather and the line-of-sight nature of laser transmission would preclude high-data-rate laser communications except over short distances and under favorable weather conditions. The situation, however, for ground-to-space and space-to-ground communications is much more favorable, and therefore, work on this type of data link has been actively pursued by both NASA and the Air Force. Studies⁴ have shown that by the use of redundant earth-based transmitter/receiver sites, link outages can be reduced to a few tenths of a percent. Through the use of airborne transmitter/receiver systems, even these minor outages can be eliminated.

From the beginning of the study of atmospheric turbulence, the sophistication of the theoretician has far outpaced the experimentalist. There are good and sufficient reasons for this state of affairs. The mechanism for the generation of turbulence is beyond the control of the experimenter and, therefore, it is impossible to perform controlled experiments in which the state of turbulence can be fixed while measurements are performed. The problem is further exacerbated by the fact that the experimenter rarely has sufficient instrumentation to even specify the state of the atmosphere during his measurements.

Some of the earliest experiments in optical propagation were made by astronomers, who were concerned with the variations in seeing and scintillation because these effects masked their ability to study the characteristics of extraterrestrial sources. Although considerable time and effort was expended in their studies, most of their work was performed during a period when no adequate theory was available to explain the mechanism of the observed effects, and therefore much of the work is of a subjective nature

with inadequate supportive data to interpret the results. Notable exceptions to this state of affairs are the work of Mikesell and Heag⁵, Protheroe⁶, Young⁷, Ramsey⁸, Coulman⁹, and later, Rufton¹⁰. Except for the studies made using astronomical sources, nearly all of the experimental attempts to verify theory have been made over horizontal propagation ranges. If a review of the proportion of work performed on horizontal ranges compared to vertical propagation paths were made, it would reveal that while thousands of experiments have been performed over horizontal ranges, almost nothing has been done to measure the effects of atmospheric turbulence on a laser beam propagating over a vertical path.

When work on the study of atmospheric turbulence was started at GSFC, by the authors, it became apparent after a short amount of study that the theoretical predictions of turbulence effects were being adequately pursued by other agencies and organizations and that the area which was most in need of investigation was the experimental verification of existing theory. Because all of the theoretical predictions of the optical effects are based upon the state of atmospheric turbulence, a development program was started to build a sensory device capable of directly measuring the state of turbulence. The outcome of this effort was the thermosonde, a lightweight electronic device capable of being borne aloft by a small weather balloon to measure the state of turbulence at altitudes to 100,000 feet, well above the last significant turbulence. In 1968, interest in laser propagation was at its peak, and many groups were considering methods of measuring turbulence in the upper atmosphere. Because of their ability to reach high altitudes and because they generate no atmospheric turbulence, the authors were at this time considering measurements made from high-altitude research balloons. Because of our interest in balloons as a vehicle for turbulence measurements, the Office of Advanced Research and Technology forwarded to us a proposal by the Sylvania Electronic Systems, Western Division to perform a series of balloon-borne laser propagation experiments. The outcome of this proposal was the experiment described in this report.

The experiment, which was titled "Balloon Atmospheric Propagation Experiment" (BAPE), was performed at White Sands Missile Range in the fall of 1970, and is to this date the only controlled measurement of laser propagation over a vertical path. The experiment was repeated in 1971 at the same location and the two flight series have been named BAPE I and BAPE II to distinguish between them. This report will describe only the data obtained in BAPE I.

The experiment plan was to measure the optical effects of turbulence over a vertical path while at the same time measuring, with the thermosonde, the distribution of turbulence along the path. In this manner, the optical effects predicted by theory could be compared to the measured results in an effort to verify the validity of theory. The experiment has not uncovered any phenomena in contradiction to existing theory, but has confirmed many of the existing predictions. We feel that although some new and unexpected phenomenon might perhaps be more dramatic, our confirmation of existing predictions is actually more constructive.

To this date there have been only three successful attempts to measure the characteristics of laser propagation between ground and space. All of these have been performed by the authors, starting with the GEOS II Laser Detector Experiment and followed by the BAPE I and BAPE II experiments. The results of these experiments confirm the predictions of existing theory within the limits of the experiment. Because of the importance of this field of investigation to the development of the laser as a communications tool and because of the demonstrated success of balloon-borne instrumentation as a means of obtaining atmospheric propagation data, future experiments of this type are being planned.

The balloon-borne experiment described in the subsequent sections of this report constitutes the first definitive set of laser data on the effects of atmospheric turbulence over a vertical or near-vertical path. As such, the experiment provides the basis for meaningful predictions of laser system performance and data which establishes the utility and limitations of various propagation theories. Therefore, this was an important experiment with far-reaching consequences.

Basically the objective of the experiment was to propagate two laser beams, one argon (5145\AA^0) and one CO_2 (10.6μ), over a vertical path from the ground to receivers located above the atmosphere, and to measure the scintillation of the upgoing beams. Simultaneous measurements of the state of turbulence along the path allow the scintillation statistics to be compared on the basis of existing theory to the experiment results. This type of experiment has four important results:

1. The measurements of scintillation are directly applicable to estimation of scintillation of earth-to-space laser links.
2. The measurements of the state of turbulence provide new data on the state of atmospheric turbulence, no direct experimental data on turbulence above 3.5 km (10,000 ft) was available prior to the experiment.

3. By comparing the actual scintillation statistics with those based upon theory plus the turbulence profile, we can check the validity of existing propagation theories.
4. Knowing that these theories are correct (assuming that the theories check out), we can make far ranging predictions on the performance of laser communications systems with a high degree of confidence.

REFERENCES

1. Kolmogorov, A.N., The Local Structure of Turbulence in Incompressible Viscous Fluid for Very Large Reynolds Numbers, *Doklady Akad. Nauk SSSR*, Vol. 30 (1941), p. 391. German translation in *Sammelband zur Statistischen Theorie der Turbulenz*, Akademie-Verlag, Berlin (1958), p. 71.

Kolmogorov, A.N., Dissipation of Energy in Locally Isotropic Turbulence, *Doklady Akad. Nauk SSSR*, Vol. 32 (1941), p. 16. German translation in *Sammelband zur Statistischen Theorie der Turbulenz*, Akademie-Verlag, Berlin (1958), p. 77.
2. Chernov, L.A., Correlation of Amplitude and Phase Fluctuations of a Wave Propagating in a Medium with Random Inhomogeneities, *Akust. Zh.*, Vol. 1 (1955), p. 52.

Chernov, L.A., Correlation Properties of a Wave in a Medium With Random Inhomogeneities, *Akust. Zh.*, Vol. 2 (1956), p. 211.

Chernov, L.A., Correlation of Field Fluctuations, *Akust. Zh.*, Vol. 3 (1957), p. 132.
3. Tatarski, V.I., On Phase Fluctuations of Sound in a Turbulent Medium, *Izv. Akad. Nauk SSSR, Ser. Geofiz.*, No. 3 (1953), p. 232.

Tatarski, V.I., On the Theory of Propagation of Sound Waves in a Turbulent Flow, *Zh. Eksp. Teor. Fiz.*, Vol. 25 (1953), p. 74.

Tatarski, V.I., On the Criterion for the Applicability of Geometrical Optics in Problems of Wave Propagation in a Medium with Weak Refractive Index Inhomogeneities, *Zh. Eksp. Teor. Fiz.*, Vol. 25 (1953), p. 84.

Tatarski, V.I., On Amplitude and Phase Fluctuations of a Wave Propagating in a Weakly Inhomogeneous Atmosphere, *Doklady Akad. Nauk SSSR*, Vol. 197 (1956), p. 245.

Tatarski, V.I., Microstructure of the Temperature Field in the Layer of the Atmosphere Near the Earth, *Izv. Akad. Nauk SSSR, Ser. Geofiz.*, No. 6 (1956), p. 659.

Tatarski, V.I., *Wave Propagation in a Turbulent Medium*, McGraw-Hill Book Co., Inc., New York (1961).
4. Brintzenhoff, H.A., Cox, J.L., Williams, J.T., and Nuemann, C.J., Probability of Clear Line of Sight Through the Atmosphere for Satellite-based Laser Communications System, *NASA TM X-78-7* (March 1971).
5. Mikesell, A.H., Hoag, A.A. and Hall, J.S., The Scintillation of Starlight, *J. Optical Soc. Am.*, Vol. 41 (1951), p. 659.
6. Protheroe, W.M., Preliminary Report on Stellar Scintillation, *Contrib. Perkins Observ.*, Ser. 2, No. 4 (1955), p. 127.

7. Young, A. T., Photometric Error Analysis, VIII The Temporal Power Spectrum of Scintillation, Applied Optics, Vol. 8, No. 5 (May 1969), pp. 869-891.
8. Ramsey, J. V., and Kobler, H., A Stellar Image Monitor, Observatory, Vol. 82 (June 1952), pp. 107-111.
9. Coulman, C.E., Optical Image Quality in a Turbulent Atmosphere, J. Optical Soc. Am., Vol. 55, No. 7 (July 1965), pp. 806-812.
10. Bufton, J.L., An Investigation of Atmospheric Turbulence by Stellar Observations, NASA TR R-369 (Aug 1971).

2. SUMMARY

This section provides a brief synopsis of the results from the Balloon Atmospheric Propagation Experiment.

The vertical profile of turbulence in the first 6 km of the atmosphere was found to be approximately

$$C_N^2 = 4 \times 10^{-14} h^{-1/3} e^{-h/1000} m^{-2/3}$$

The log-amplitude variance at 45° from zenith had an average value of 0.198 at $0.5145 \mu m$ and 0.00510 at $10.6 \mu m$. Measured wavelength dependence of scintillation was found to be within 8% of that predicted by the 7/6 power law. The sample log-amplitude variance was itself a random variable with a log-normal distribution and a standard deviation of $\ln 2$. This indicates that the strength of turbulence varies with time in the same manner.

Log-amplitude covariance was measured and the correlation lengths were found to be, as predicted by theory, proportional to $\lambda^{1/2}$; the size of the correlation lengths was also found to be as predicted by theory. In order to test this last relationship, a method of approximating the atmosphere by a multilayer system of turbulence was developed and used to predict the correlation lengths. Both correlation length and the shape of the correlation coefficient predicted by this procedure show close correspondence to measured values.

Using the above method, aperture averaging for large apertures is computed and shown to be in close agreement with other methods of obtaining aperture averaging factors.

Autocorrelation of irradiance and power spectral density were measured and compared to predicted results. A close agreement between theoretical and measured values indicates that the temporal behavior of the scintillation can be obtained from a knowledge of the height of the turbulence layers and their wind speeds.

The results of the experiment represent a fairly complete investigation of the scintillation effects of atmospheric turbulence over a vertical path, although much remains to be measured. We have found no parameter which does not have the magnitude and behavior predicted by theory. Results of the experiment tend to confirm the validity of present predictions of the effects of atmospheric turbulence.

3. DESCRIPTION OF EQUIPMENT

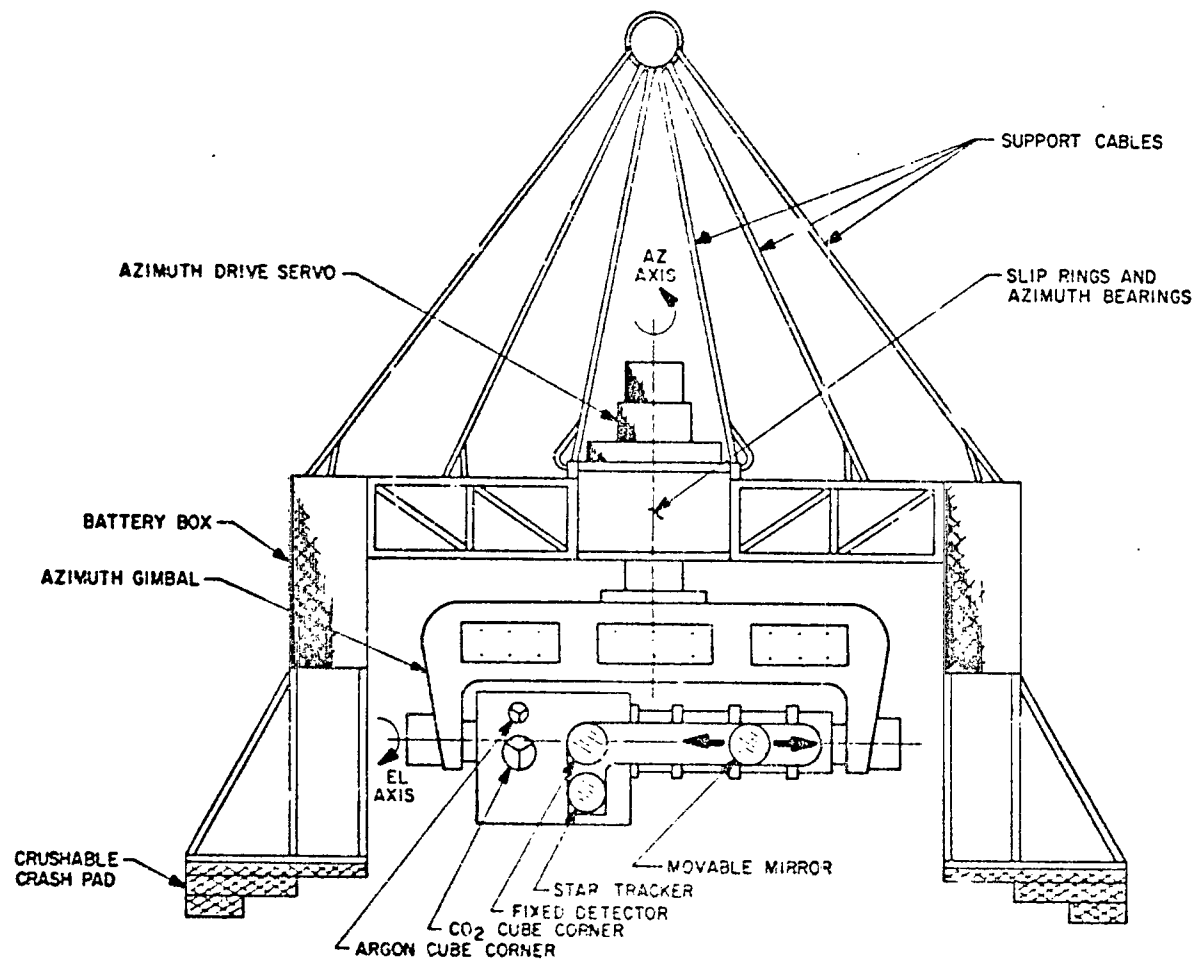
3.1 BAPE PAYLOAD

The following sections describe the design and construction of the BAPE payload which was the flight vehicle used to carry the optical detectors of the experiment above the atmosphere. The payload was fabricated by Sylvania Electronic Systems Western Division under contract NAS 5-11679. The material from the following sections is in part abstracted from the BAPE Phase I report of August 14, 1969, with changes and additions made where required. The principal authors of this report were Mr. Arthur Kraemer, Dr. Paul J. Titterton, Mr. Tom Mulcahy, and Mr. Scott Overstreet. Other contributors include Mr. Clyde Brown, Mr. Connell Ward, Mr. Michael Halus, and Dr. Douglas Woodman. Professor J. Richard Kerr of the Oregon Graduate Center acted as a program consultant.

The purpose of the material in the following sections is to familiarize the reader with the construction and operation of the payload so that he may better understand how the data was obtained and its significance.

3.1.1 GENERAL DESCRIPTION OF PAYLOAD

The BAPE payload shown in Figures 3-1 and 3-2 consisted of an optical receiver system in an inverted azimuth-elevation gimbal system. The elevation axis (see Figure 3-3) contains four optical receivers, a star tracker, servo electronics, and two cube corner retroreflectors. It is pivoted on bearings supported by the azimuth gimbal and driven by a dc torquer through elevation angles from -26 to -90 degrees. The azimuth gimbal supports the elevation axis and connects it to the azimuth axis. The large box-shaped section of the azimuth gimbal contains batteries, telemetry encoders, and other electronics for the operation of the servo system. These electronics are connected by a cable wrap to the elevation axis. Above the azimuth gimbal is the azimuth bearing and slip ring assembly which provides continuous rotation in the azimuth direction and electrical connection to the gondola. A dc torquer, tachometer, clutch, and azimuth encoder are attached to the top of the azimuth bearing and slip ring assembly to complete the azimuth drive system. The gondola (see paragraph 3.1.5) provides a framework for supporting the components attached below the azimuth axis and for supporting the battery boxes. It consists of three arms connected at their inner ends to the elevation axis and at their outer ends to the battery boxes. The battery boxes contain the



5528 3.1.2-1

Figure 3-1. BAPE Payload

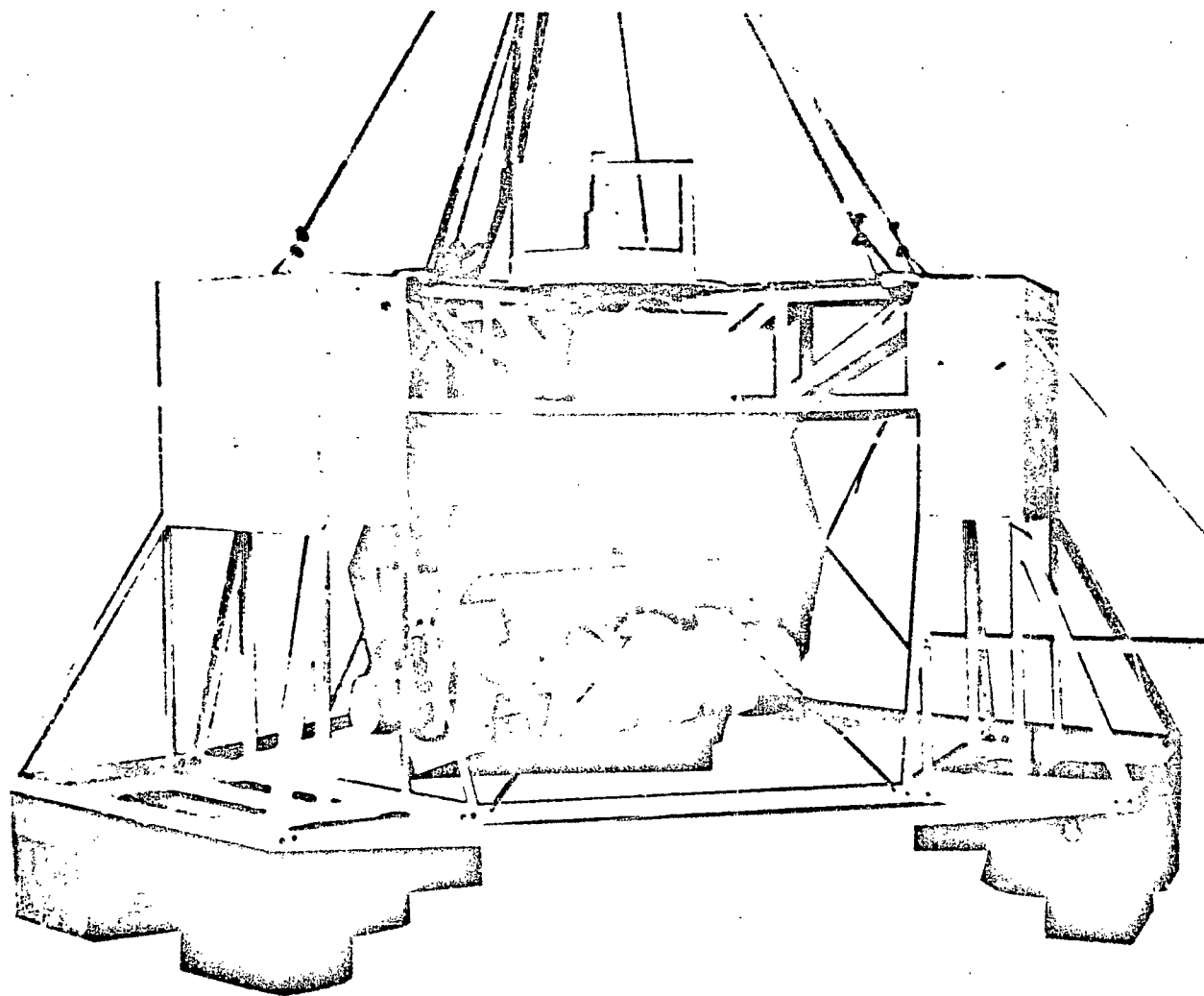


Figure 3-2. BAPE Payload

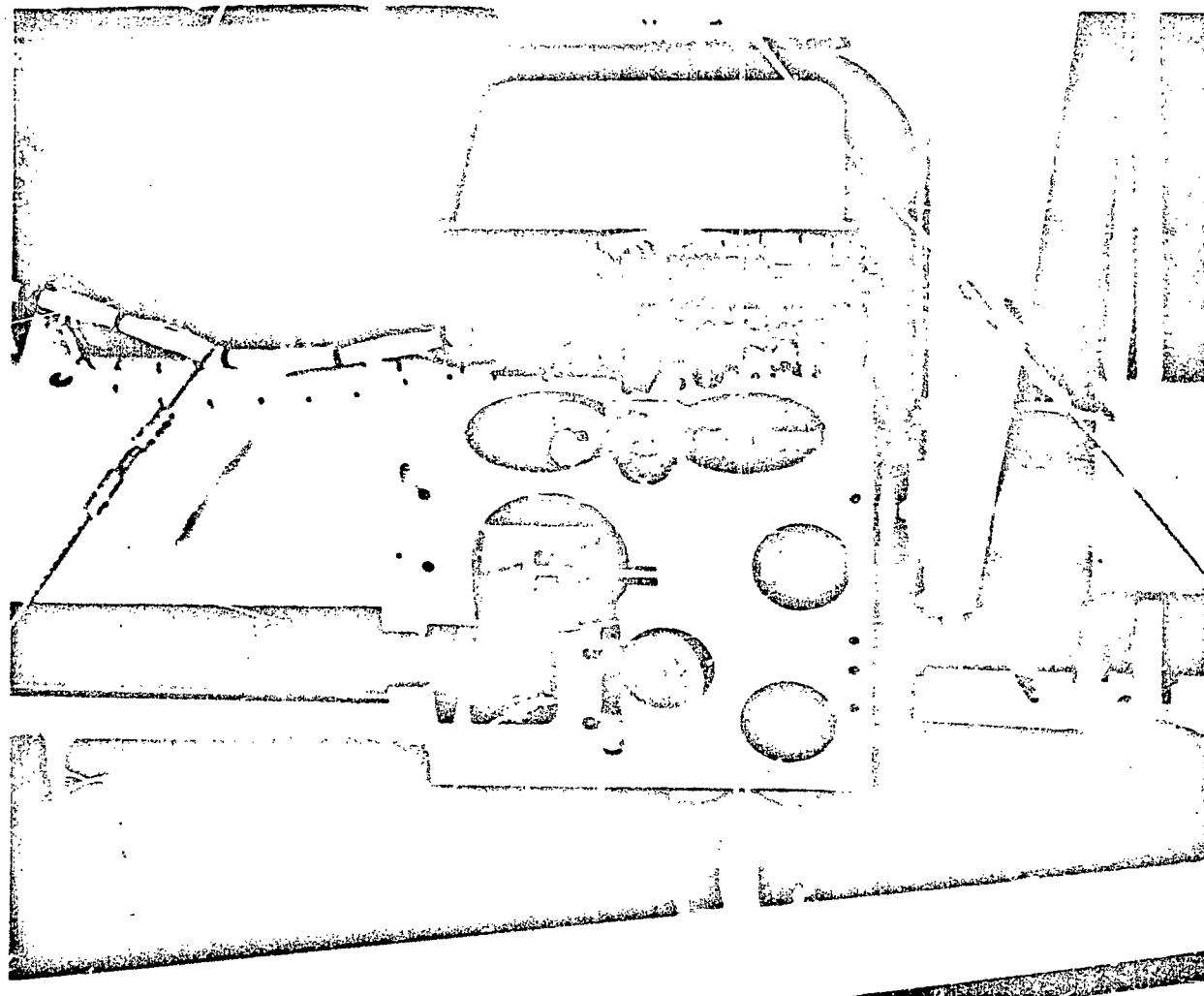


Figure 3-3. Elevation Axis

batteries necessary to power the payload as well as telemetry and electronics systems. The mass of the heavy batteries on the ends of the arms acts as an inertia flywheel against which the azimuth axis drives. Struts connected to the bottom of the battery boxes provide protection of the payload when it strikes the ground at the end of the parachute descent. Disposable, corrugated cardboard crush pads on the bottom of these struts are used to absorb the energy of the impact.

3.1.2 ELEVATION AXIS AND OPTICAL DETECTOR SYSTEMS

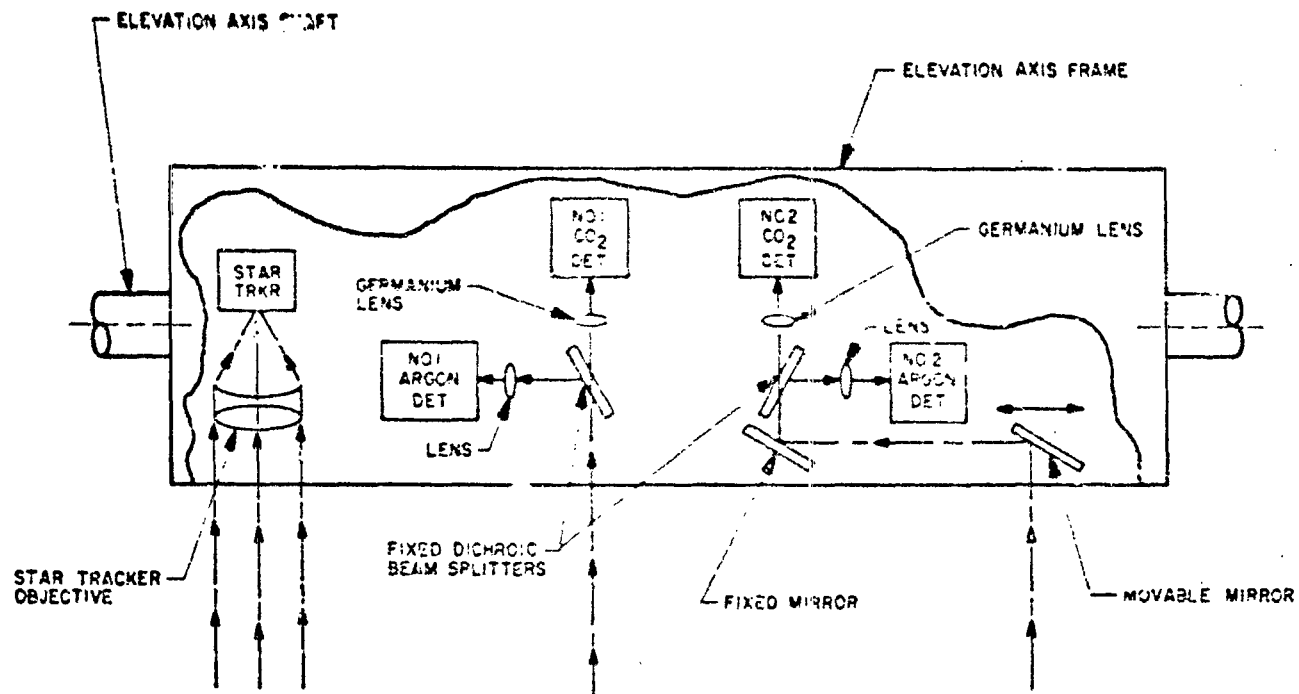
An optical schematic of the elevation axis and optical detector systems is shown in Figure 3-4. The elevation axis contained two detectors at each of the wavelengths 0.5145 μm and 10.6 μm . One system operated fixed and the second system operated with a movable input mirror. In system I, the received beam was received by the dichroic beam splitter, which was used to separate the argon (0.5145 μm) and the CO_2 (10.6 μm) beams. The dichroic reflected the 10.6- μm beam through a refractive f/1 germanium lens onto the HgCdTe detector mounted in a liquid nitrogen dewar. The 0.5145- μm beam passed through the dichroic and was reflected through a lens arrangement onto the photomultiplier detector.

In system II, the received beam was reflected off the movable input mirror and a fixed mirror prior to reaching the dichroic beam splitter. The optical arrangement for system II was identical to system I after the dichroic beam splitter. Additionally, a quadrant star tracker with an f/3 lens was located in the elevation axis.

Figure 3-5 shows the exterior of the elevation axis.

The movable mirror varied its position from 4 cm to 100 cm with respect to the fixed system. The movable mirror traveled on precision stainless steel rods using Thomson ball bushings to reduce frictional loading, and was driven by a gear head servo motor. The location of the movable mirror was controlled by an electrically operated system with readouts at the ground station to indicate mirror positions.

The electronic system for the optical receivers was designed to extract the atmospheric modulation on the laser beam and convert it to an analog signal of 1-kHz bandwidth. Since it was desirable to observe low-level signals accurately, it was necessary to eliminate the effects of background. Therefore, the laser beam was chopped with a 50% on-off duty cycle at the transmitter at a 5-kHz rate and transmitted through the atmosphere to the receiver, thus acquiring the atmosphere modulation. The laser



3520-3.1 3-1

Figure 3-4. Optical Schematic, Elevation Axis and Optical Detectors

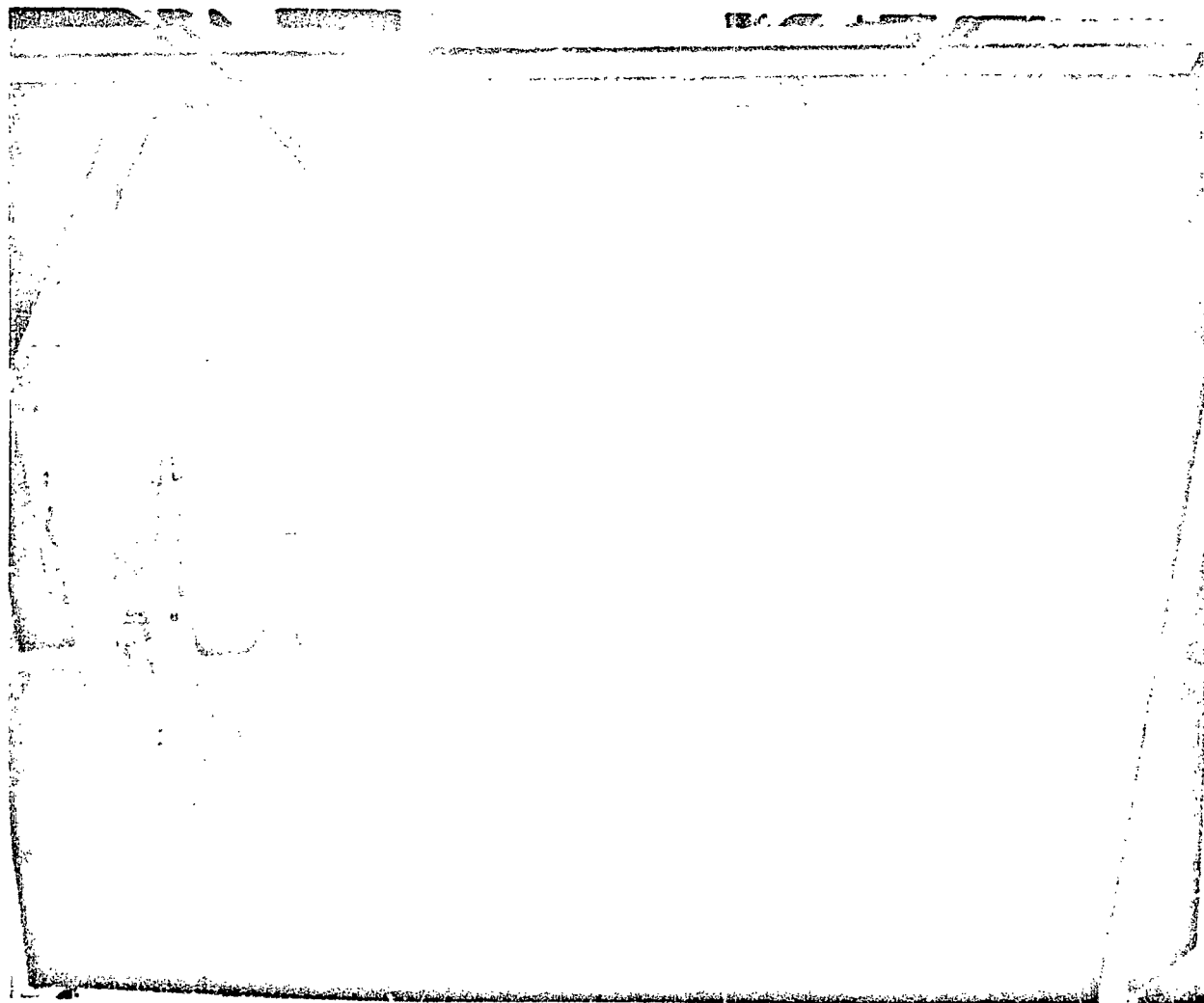


Figure 3-5. Elevation Axis. Exterior

receiver observed both the chopped laser beam (with atmospheric modulation) and a slowly varying background and rejected the background with a high-pass filter. The signal was returned to the ground (via the telemetry system). Figure 3-6 shows the optical receiver electronic system.

3.1.3 QUADRANT STAR TRACKER

A quadrant star tracker mounted on the elevation axis was used to track the 0.5145- μm laser beam from the ground transmitter to an accuracy of ± 1 milliradian. This information was relayed to the attitude stabilization system to point the elevation axis with its four optical receivers. Since the lens in front of the quadrant photodetector made such a small image that the range of the star tracker was less than that required, it was defocussed to provide a greater range of error signals.

The quadrant axes of the photodetector were positioned 45 degrees (see Figure 3-7) from the elevation and azimuth axes so that the error signal for each axis generated by differentially connecting the diagonal quadrants was

$$\Delta A = 2\sqrt{2} r \Delta x \quad \text{for } \Delta x \ll r$$

for uniform energy density, where

ΔA = increase in spot area in quadrant 1 minus decrease in spot area in quadrant 3

Δx = misalignment along x axis

r = spot radius

Positioning the instrument axes 45 degrees from the quadrant detector axes resulted in no crosstalk between the error signals for small misalignments.

The 1-inch useful photocathode surface allowed acquisition of the ground transmitter beam over a ± 12.5 -degree field of view.

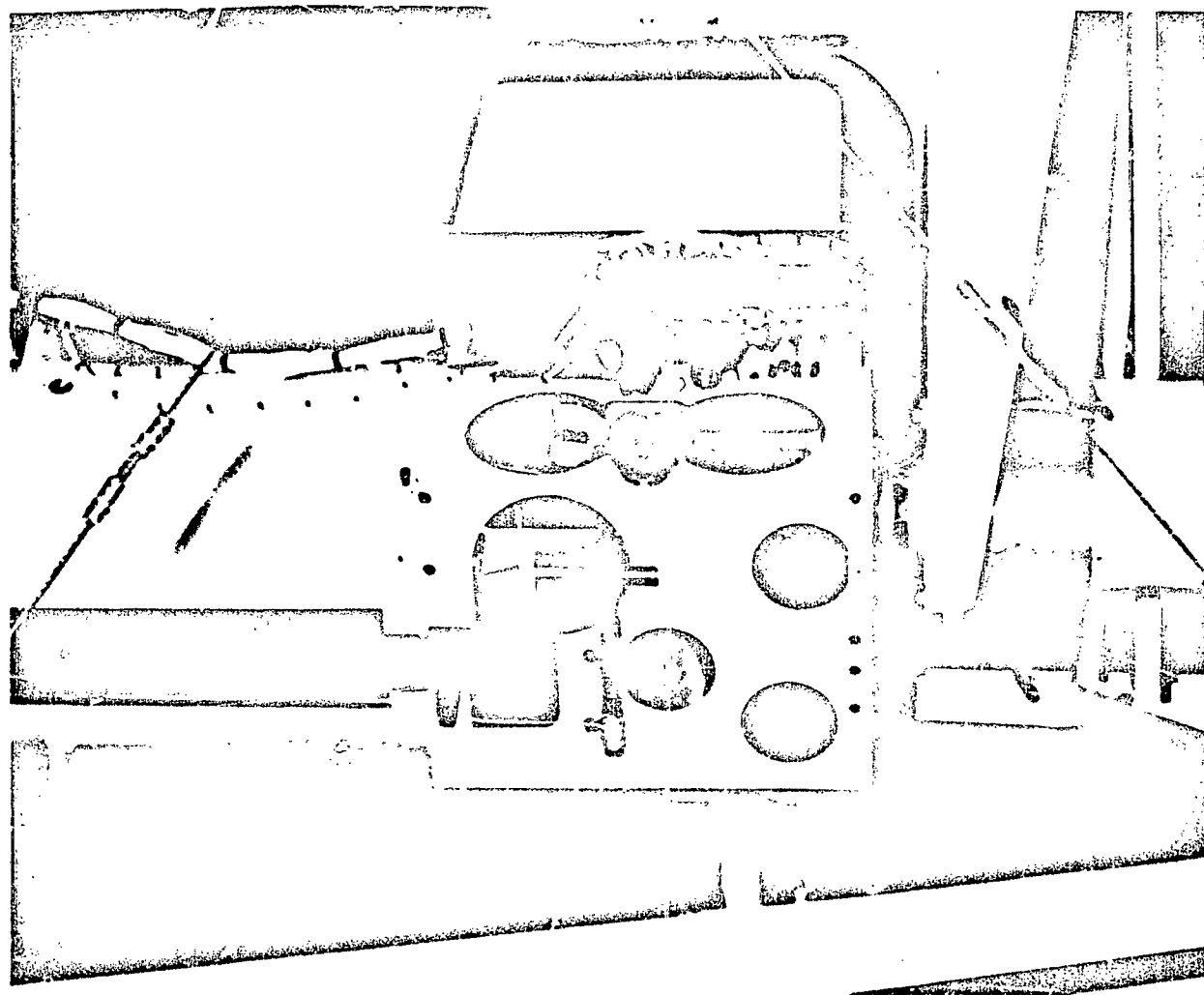
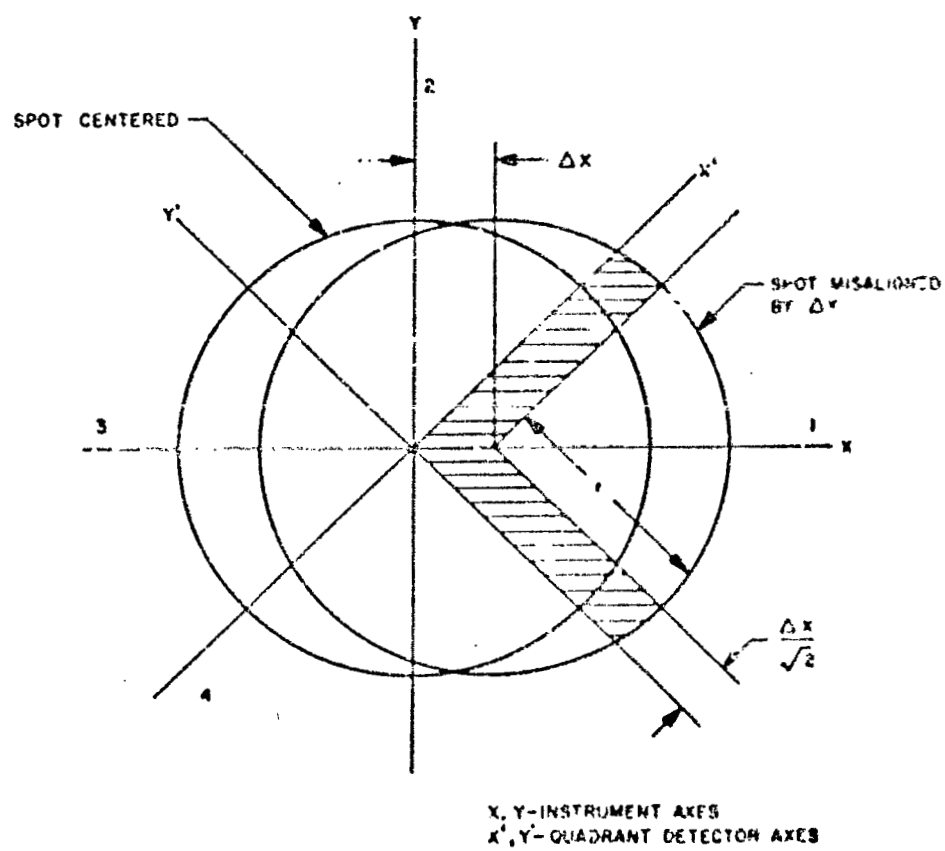


Figure 3-6. Optical Receiver Electronic System



$$\text{DIFFERENTIAL AREA} \approx 4 \cdot \frac{\Delta x}{\sqrt{2}} \cdot (\text{QUADRANT 1} - \text{QUADRANT 3})$$

Figure 3-7. Quadrant Detector Error Signal

3.1.4 ATTITUDE STABILIZATION SYSTEM

To keep the optical receivers continuously pointing at the upcoming beam, it was necessary to mount them within two controlled orthogonal axes of an elevation-under-azimuth configuration. These axes were controlled from the ground by way of the up telemetry link, and their positions were known at all times from data transmitted on the down telemetry link and displayed for the operator on the ground. Once the upcoming beam was acquired by the quadrant star tracker, it developed azimuth and elevation error signals which were amplified and applied to the axial drives in such a way as to maintain the instrument pointing at the beam. The positioning system is shown in Figure 3-8.

To acquire the beam initially, the operator utilized the elevation and true bearing data from the beam pointing equipment. He first commanded the elevation axis to depress by the same angle that the $0.5145\text{-}\mu\text{m}$ laser beam from the ground tracking system was elevated. Next, he commanded azimuth axis of the payload to look along a true bearing that was the reciprocal of the bearing from the ground tracking system to the balloon. When beam interception did not occur, the operator conducted a search through a small zone about this nominal position to effect intercept. An auto gate circuit automatically put the attitude stabilization system into the automatic tracking mode when the beam was detected. An override command was provided in order to break track on any undesired energy sources.

The relationship of the gondola to magnetic north was measured with a flux gate transmitter of the type used in gating aircraft directional gyroscopes. For best accuracy and consistent operation, the device was located as far away from the rest of the equipment as possible. For this reason, it was placed at an outboard location on one of the gondola arms. Thus, the flux gate transmitter measured the relationship of the gondola with respect to the earth. The optical receiver system was positioned in azimuth with respect to the gondola and the angle between the two was measured by a synchro differential transformer which was driven electrically from the flux gate transmitter. The output of the synchro differential was then the bearing of the optical receiver system with respect to magnetic north. This output was converted to a dc analog voltage which fed a voltage-controlled oscillator (VCO) in the telemetry system. A servo repeater shown in Figure 3-8 accomplished this function.

Each axis was driven by a dc servo motor and amplifier combination. The amplifier inputs were either the amplified signals from the quadrant star tracker in the automatic tracking mode or a constant velocity (dc level) input that was applied when manual control was being exerted from the ground station. The ground controller could also override all other controls by actuating the standby mode. This mode was employed to break track from any undesired energy sources. At any time that control was not being exerted on the axes, they were held in position by electro-mechanical energize-to-release type brakes.

When the optical receiver system was positioned by either axis, the remainder of the equipment (including the balloon) reacted in the opposite direction. The amount of the reaction was proportional to the ratio of the moments of inertia of the optical receiver system and the remainder of the equipment. When the equipment reacted to an elevation change, the restoring force of gravity quickly restored the original orientation. The restoring forces in azimuth were less dependable and of lesser magnitude, however, consisting of wind effects and friction between the equipment and the surrounding air. To keep the apparatus relatively stable then, it was important to minimize the reaction to azimuth motion. This was accomplished by utilizing the gondola as a reaction wheel. As little equipment as possible and practical was contained within the positionable portion of the payload, and the remainder was packaged at the extremities of the gondola. In this manner it was possible to keep the ratio of the azimuthal moment of inertia of the parts below the azimuth axis lower than one-tenth that of the remainder of the equipment, a condition that assured relatively smooth operation. The arms of the gondola also served the purpose of protecting the centrally located optical receiver system (the most expensive part of the equipment) upon landing.

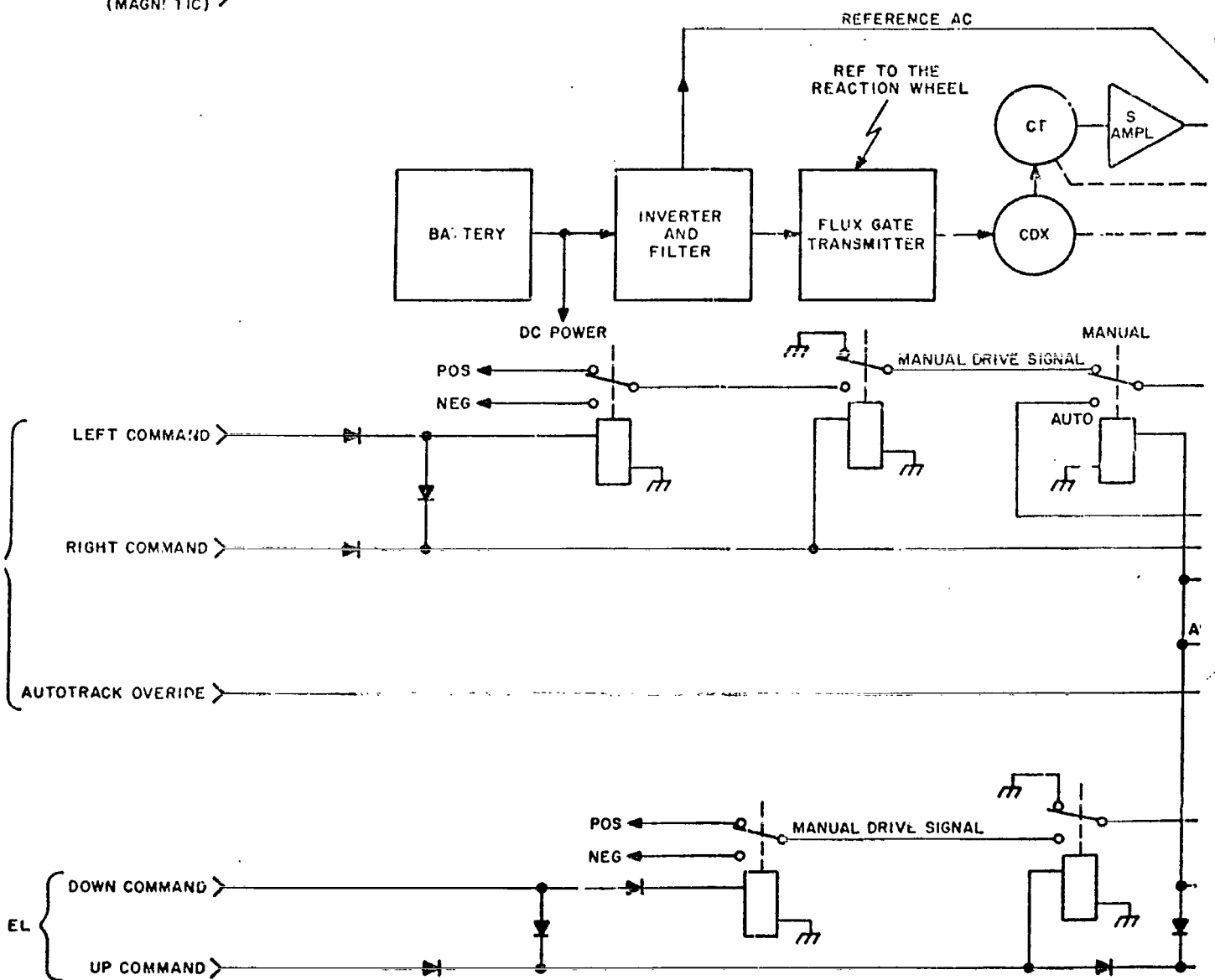
3.1.5 GONDOLA

The gondola (Figure 3-9) was the basic framework for supporting the remainder of the systems of the balloon payload. It consisted of an aluminum girder frame supporting the azimuth axis and slip ring at its center, and the three battery boxes at its extremities. In addition to its role as a framework and a container for the batteries, the gondola also acted as a reaction wheel for the servo system and as a protective cage for the more delicate systems of the payload. Because of its function as a protective cage, it normally sustained some damage in each flight and was therefore constructed as simply as possible to facilitate repair. Corrugated cardboard crush pads below

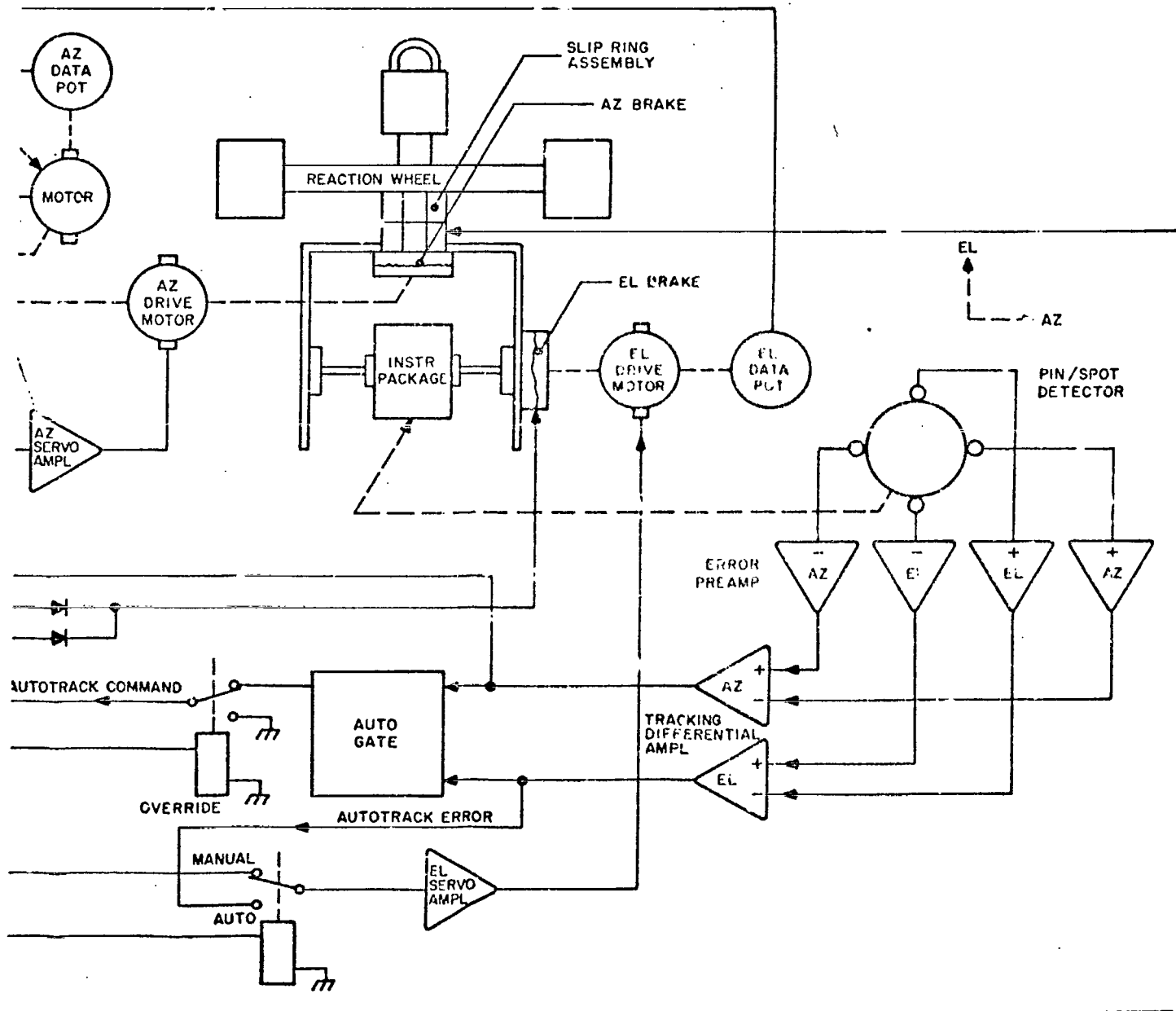
ALDOUT FRAME 1

EL POSITION DATA >

TRUE BEARING
(MAGNETIC) >



FOLDOUT FRAME 2



5520-3.1.5-

Figure 3-8. Positioning System

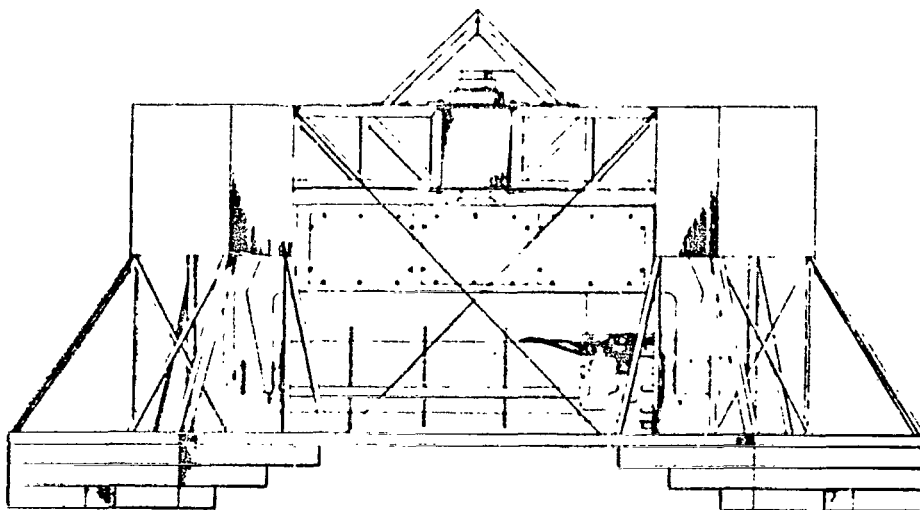
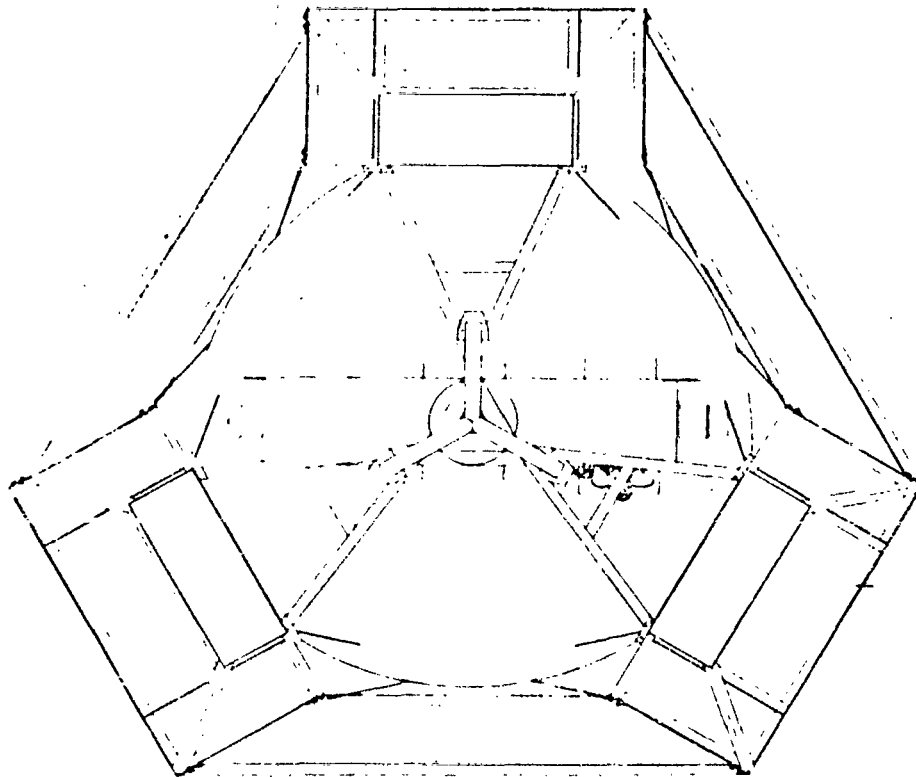


Figure 3-9. Gondola Framework

each battery box absorbed most of the landing impact and were replaced after each flight. The top of the gondola was equipped with a roll cage to protect the azimuth servo in the event of a rollover, and with sheet metal covers to act as sun shades as well as deflectors for ballast dropped from the balloon.

The gondola was basically a hexagonal parallelepiped with a height of approximately 5 feet and width across the flats of the hexagon of slightly less than 10 feet. It weighed (including the parts of the azimuth and elevation axes) approximately 750 lbs. Batteries were capable of operating the payload for 6 hours. The gondola was suspended in flight by nine steel cables (three from each arm) which were fastened to a steel O-ring approximately 15 feet above the azimuth axis (see Figure 3-1).

This method of support eliminates the bending loads which would be incurred by a two- or three-point support, and protects the payload from damage by the shock of the parachute opening.

3.2 THERMOSONDE

The optical measurements performed have value only for the ad hoc conditions present during the experiments unless the atmospheric conditions are known well enough to allow a full understanding of the turbulence effects and provide a real comparison with vertical propagation theory. This implies that not only the macro-meteorological variables such as wind speed and temperature as a function of altitude must be known, but that micro-meteorological variables such as the fluctuations in the temperature must also be known. The purpose of this section is to discuss the measurement basis, techniques, and apparatus for the fast temperature fluctuations.

For "clear" weather, the single parameter that describes the atmosphere's adverse effects on light propagation is the structure parameter of the index of refraction¹. This structure parameter characterizes the index of refraction fluctuations and enters into the theoretical description of the atmosphere's effects on light propagation¹⁻⁵; that is, variance and covariance of scintillations, aperture averaging, transmitter aperture dependence, beam wander, beam spread, and the phase-front effects.

Being a property of a gas (air), the index of refraction fluctuations can depend on its constituents, its pressure, and its temperature. Experimentally, it has been shown that the only dependence on the constituents is via the density⁶, which is well known. In addition, the pressure fluctuations are negligible⁶ relative to those of the temperature. Therefore, the temperature fluctuations are directly related to those of the index of refraction.

Formally, the Obukhov-Kolmogorov theory⁷ of turbulence states that the structure function of the index of refraction behaves as

$$D_N(\rho, h) \equiv \langle (N(x_1) - N(x_2))^2 \rangle = C_N^2(h) \rho^{2/3} \quad (1)$$

for $\rho \equiv x_1 - x_2$ and C_N^2 the index of refraction structure parameter, where h is the altitude, and is valid only with $l_0 \ll \rho \ll L_0$, and the line joining the measurement points is perpendicular to the wind direction.

In like manner, the temperature structure function⁷ is

$$D_T(\rho, h) = C_T^2(h) \rho^{2/3} \quad (2)$$

and⁷

$$C_N^2(h) = \left[\frac{77.6P}{T^2} \left(1 + \frac{0.0075}{\lambda^2} \right) \right] C_T^2(h) \times 10^{-12} \quad (3)$$

for pressure (P) in millibars, temperature (T) in degrees K., and wavelength (λ) in μm .

A measurement technique that suggests itself (and is widely used in ground systems⁹⁻¹³) is to mount two fast, sensitive sensors in a bridge configuration at a known distance apart. By suitably squaring and averaging the output, the temperature structure function is obtained. With ρ known, equation (2) is used to obtain $C_T^2(h)$ and equation (3) is used to obtain $C_N^2(h)$, using density tables⁸ and a simultaneous measurement of the temperature.

Sensitivity, speed, and uniformity of the two fast sensors was of prime importance. High signal levels were required to accurately measure D_T^2 and the sensors had to have matched temperature-resistance curves over the entire range of temperatures to be measured¹⁴. With thin-wire sensors, speed was no problem, and uniformity of length and cross-section was relatively easy to obtain. Sensitivity was the main questionable feature of thin-wire sensors.

The responsivity of a metallic wire sensor can be calculated from the applicable resistance-versus-temperature equation

$$R_T = R_0 (1 + \alpha T) \quad (4)$$

where $R_0 = \rho L/s$ (ρ being the resistivity, L the length, and s the cross-section) and α is the temperature-resistance coefficient.

The value ρ for platinum-rhodium¹⁵ is of order 20×10^{-16} ohms per cm, and α is of order¹² 1.3×10^{-3} per $^{\circ}\text{C}$. Therefore, for a 1-mm long, $2\text{-}\mu$ diameter platinum-rhodium wire, $R_0 \approx 64\Omega$ and $\Delta R \approx 8.3 \times 10^{-2}$ ohms per $^{\circ}\text{C}$. Therefore, demanding a sensitivity of 5×10^{-1} $^{\circ}\text{C}$ means a resistance difference of $41.5 \mu\text{ohms}$ must be discernible.

Too much current cannot be fed through the wire because the self-heating will mask and distort the turbulence effects the wire is supposed to measure.

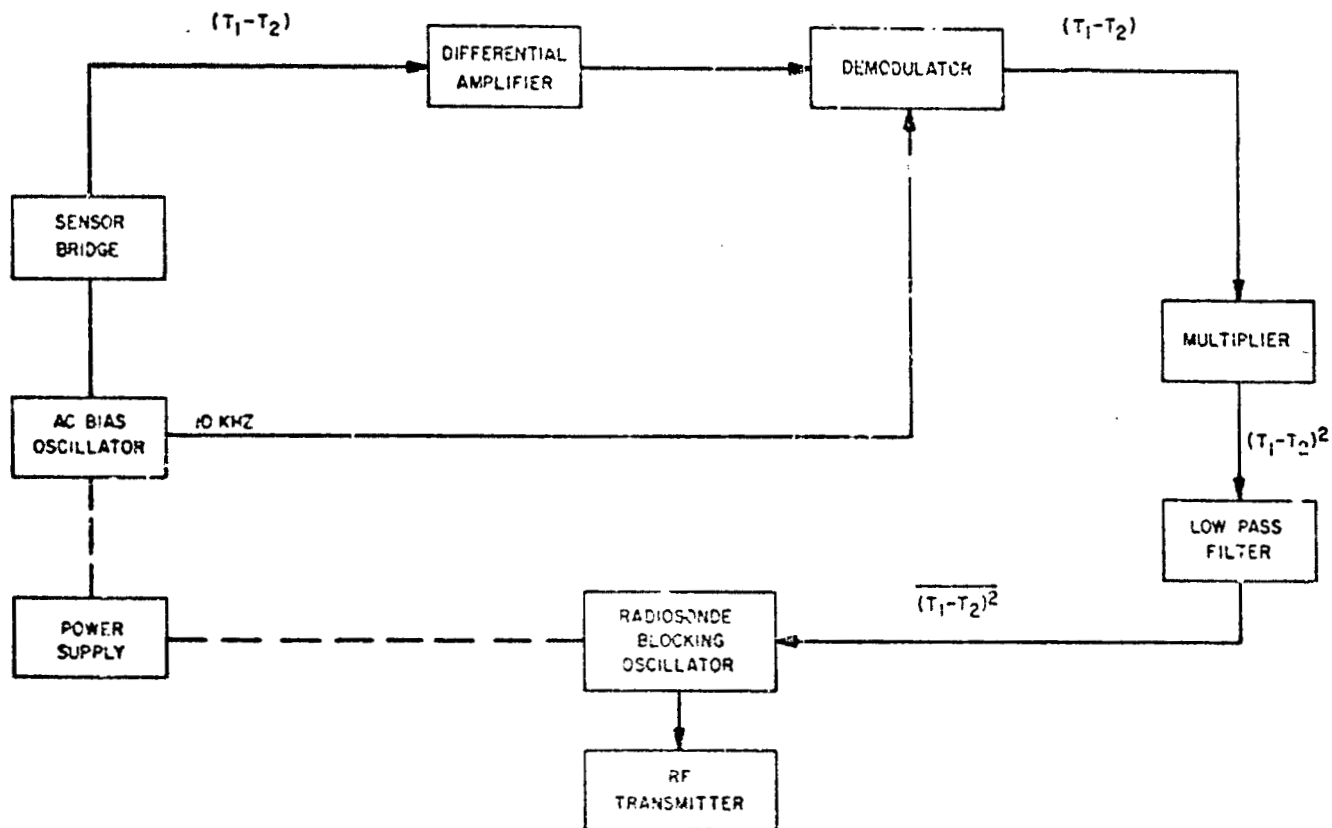
Therefore, with these design restrictions and the fact that a temperature difference was desired and amplifiers that do not extend down to dc have much lower noise, the circuit used is as shown¹⁶ in the block diagram, Figure 3-10.

The thermosonde is the box shown on the right hand side of Figure 3-13 suspended from the load bar. The rather large bulk is due to the large battery supply required to run the system for 8 hours and to keep it warm for that period. The actual circuitry and instrumentation weighed less than 20 lbs. In order to eliminate the effects of balloon wake in the C_T^2 measurement, the thermosonde was suspended from a reel hung from the load bar of the balloon. When the balloon reached an altitude of 330 m (1000 ft), the reel was released allowing the thermosonde to descend. A hydraulic drag mechanism in the reel limited the rate of descent to 17 ms^{-1} (50 ft s^{-1}) giving a deployment time of approximately 20 sec. This deployment technique allowed error-free measurements to start at an altitude of about 60 m ($\approx 200 \text{ ft}$). The reel mechanism and the sonde can be seen in Figure 3-14.

3.3 FLIGHT VEHICLE

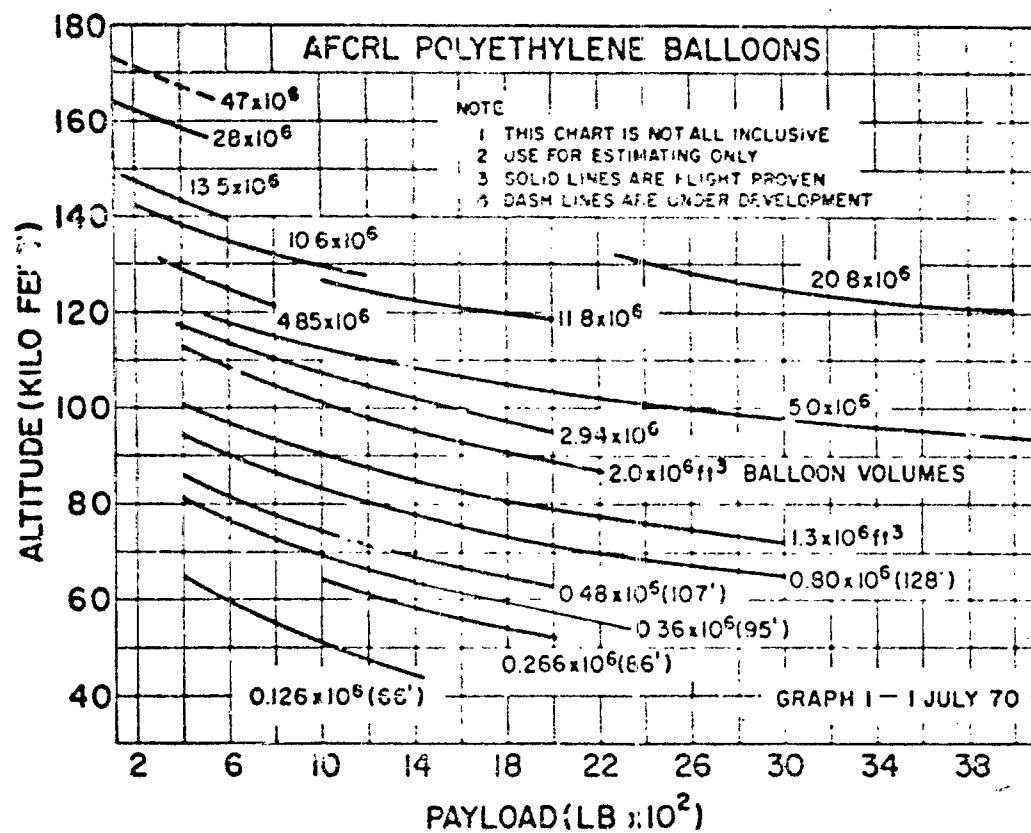
3.3.1 BALLOON CHARACTERISTICS

The balloon selected for the BAPE flights was a $2.0 \times 10^6 \text{ ft}^3$ polyethylene balloon. This selection was based upon a requirement of an altitude of about 90,000 feet (27.4 km) and the gross weight of the BAPE payload ($\approx 750 \text{ lbs}$) plus the weight of Air Force balloon control and navigation equipment ($\approx 1000 \text{ lbs}$). The total weight of approximately 1750 lbs plus the altitude of 90,000 feet makes the $2 \times 10^6 \text{ ft}^3$ balloon the proper choice for this type of flight (see Figure 3-11). Launch, navigation, recovery and all other aspects of the flight vehicle were handled by Detachment 1, Air Force Cambridge Research Laboratories — Balloon Research and Development Test Branch, Holloman Air Force Base, New Mexico, under the command of 1st Col Robert J. Reddy.



1062 3.2-1

Figure 3-10. Preliminary Sensor Electronics Design, Block Diagram



1062-331-1

Figure 3-11. Balloon Requirements

3.3.2 LOAD BAR AND RIGGING

The experiment flight configuration is shown in Figure 3-12. The BAPE payload is supported by nine steel cables which converge at a central point (Figure 3-13). This point is attached by an explosive shackle to the Air Force load bar which supports the Air Force navigation and flight control system as well as the thermosonde system and reel. In Figure 3-13 the components supported on the load bar are, from left to right: ballast hopper, command receiver and telemetry system, backup navigation transmitter, ballast hopper, and reel and thermosonde assembly. Flight configuration (reel not released) is shown in Figures 3-14 and 3-15*. The load bar, as shown in these figures, is supported by a second set of steel cables which converge on a ring at the bottom of the parachute shrouds. The load is supported on the shrouds of the open parachute and attached to the bottom of the balloon. The balloon is of the zero-pressure type, meaning that the bottom of the balloon is open and the helium is trapped only by its own buoyancy.

Vertical control of the balloon is controlled by the ballast hopper, shown in Figure 3-13, which drops iron filings to ascend, and a poppet valve about 18 inches in diameter (Figure 3-16) which releases helium to descend. Horizontal control of the balloon is obtained by ascending or descending into wind layers blowing in the desired direction.

Upon termination of the flight, the balloon is destroyed by an explosive device and the payload descends on the parachute (Figure 3-17). Upon impact the chute and load bar are disengaged from the payload by the explosive shackle so that ground winds do not drag the payload.

3.3.3 EXPERIMENT SITE AND FLIGHT PROFILE

The experiment was performed at the SCAT site on Holloman Air Force Base which is part of the White Sands Missile Range in New Mexico. The position of the site is shown in Figure 3-18. The site was on a level plain with semidesert vegetation approximately 7 miles northwest of Alamogordo, New Mexico. The plain is a valley floor with an altitude of 4000 ft (1.2 km) above sea level. The San Andres mountain range with peaks of about 8000 feet (2.1 km) lies approximately 30 miles to the west, and the Sacramento range with peaks to 11,000 feet (3.3 km) lies 10 miles to the east. During the early morning hours, cold air trapped in the valley during the night drains southward.

*The balloon in Figure 3-15 is a 60-ft-diameter balloon much smaller than the balloon used for the flights. It was used for tethered tests.

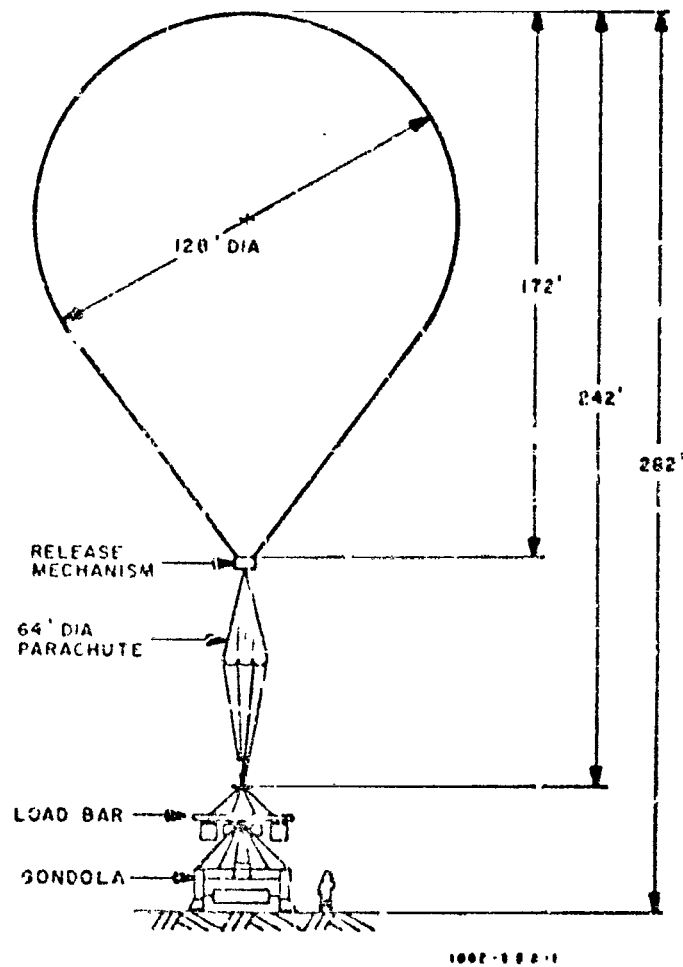


Figure 3-12, Flight Configuration

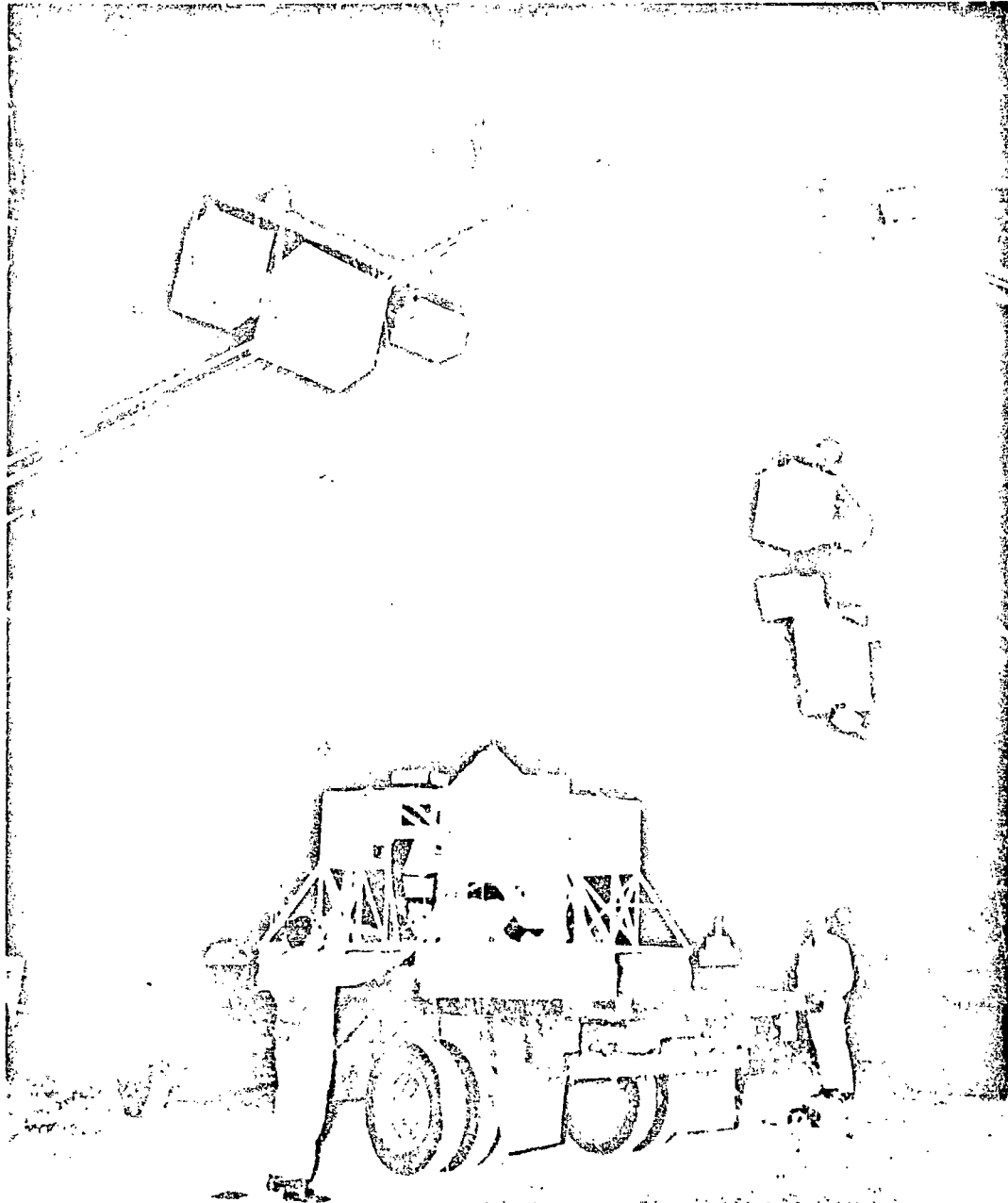


Figure 3-13. BAPE Payload Suspension

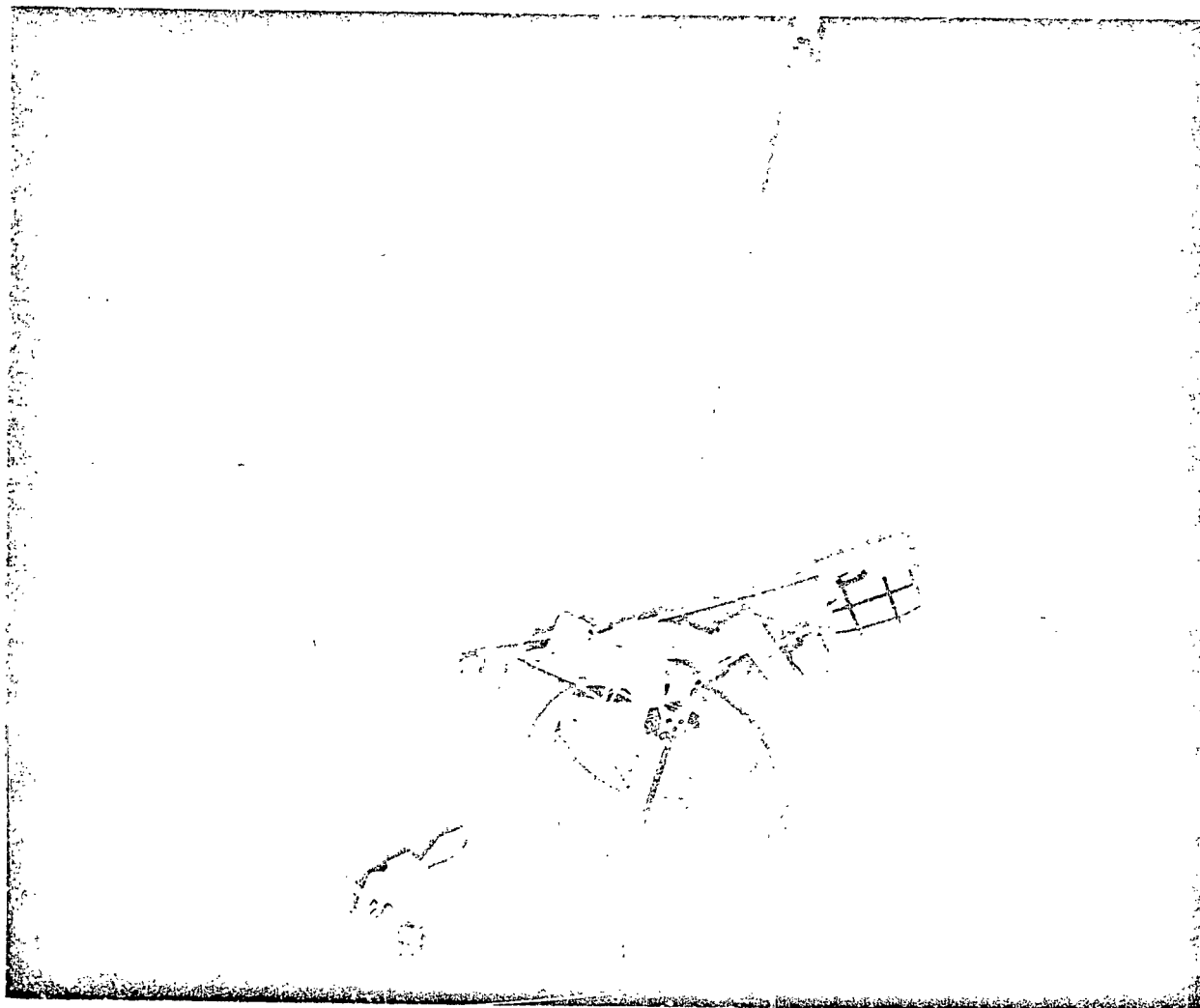


Figure 3-4. BAPE Flight Configuration

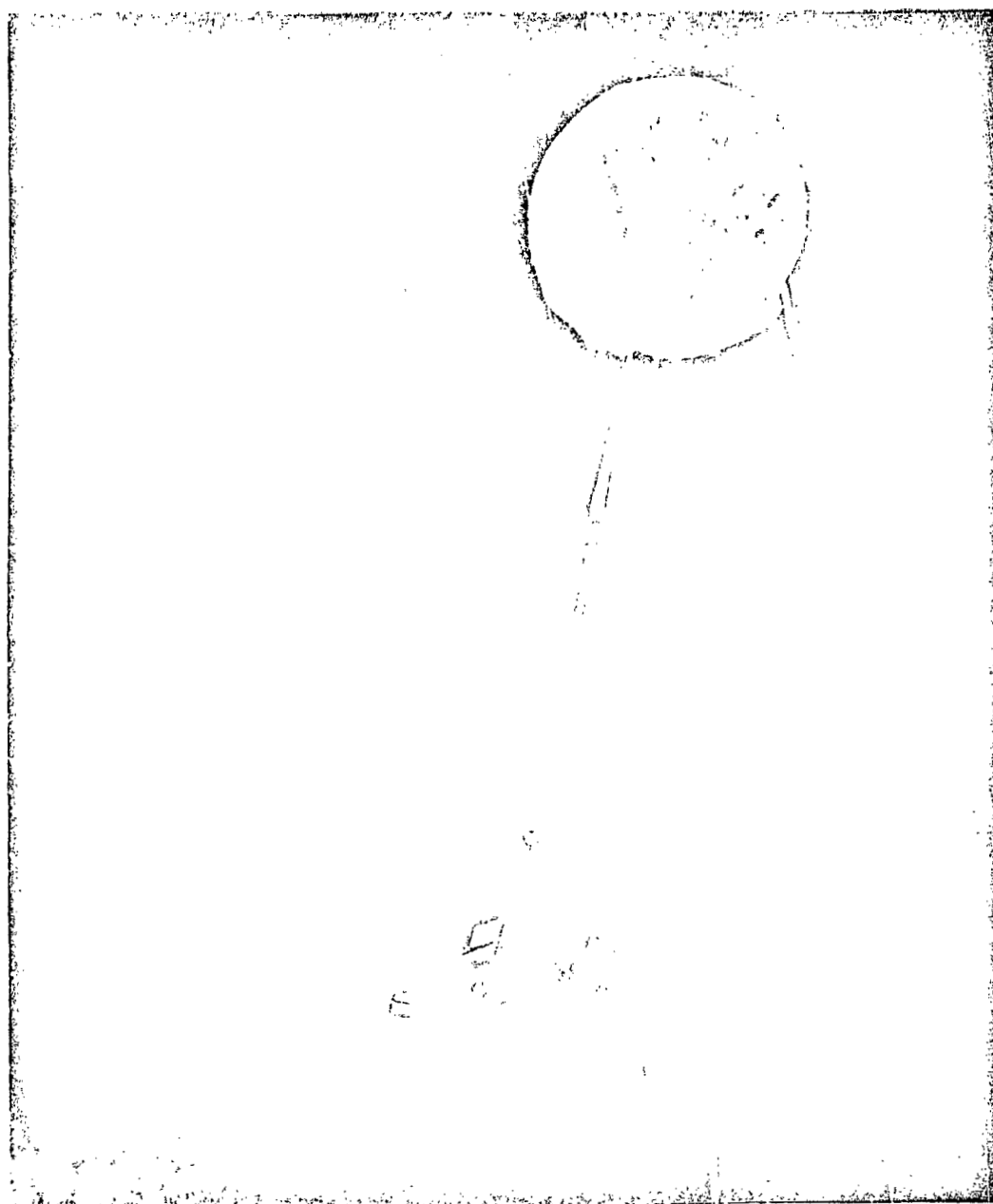


Figure 3-15. BAPE Flight Configuration

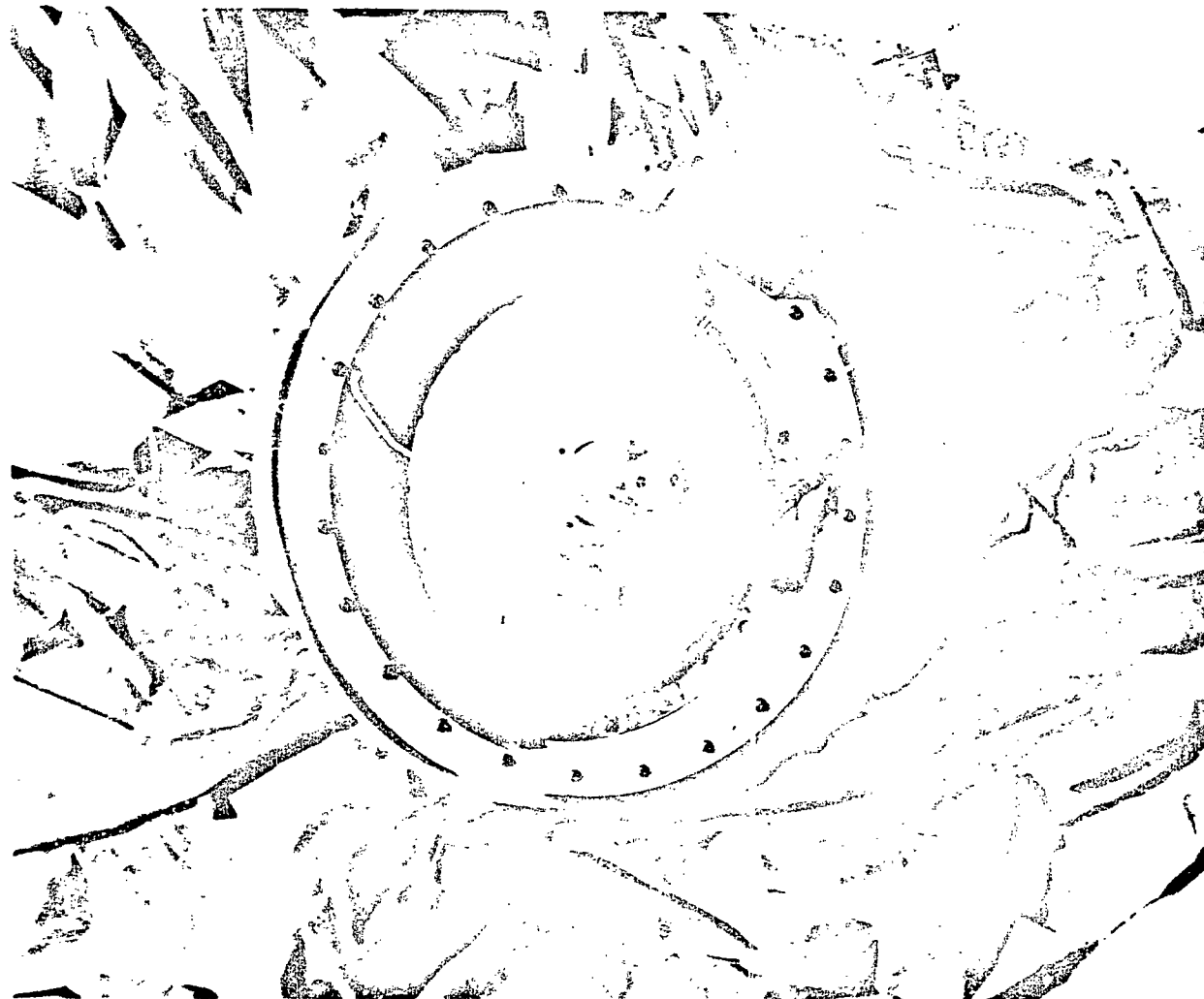


Figure 3-16. Poppet Valve



Figure 3-17. BAPE Parachute

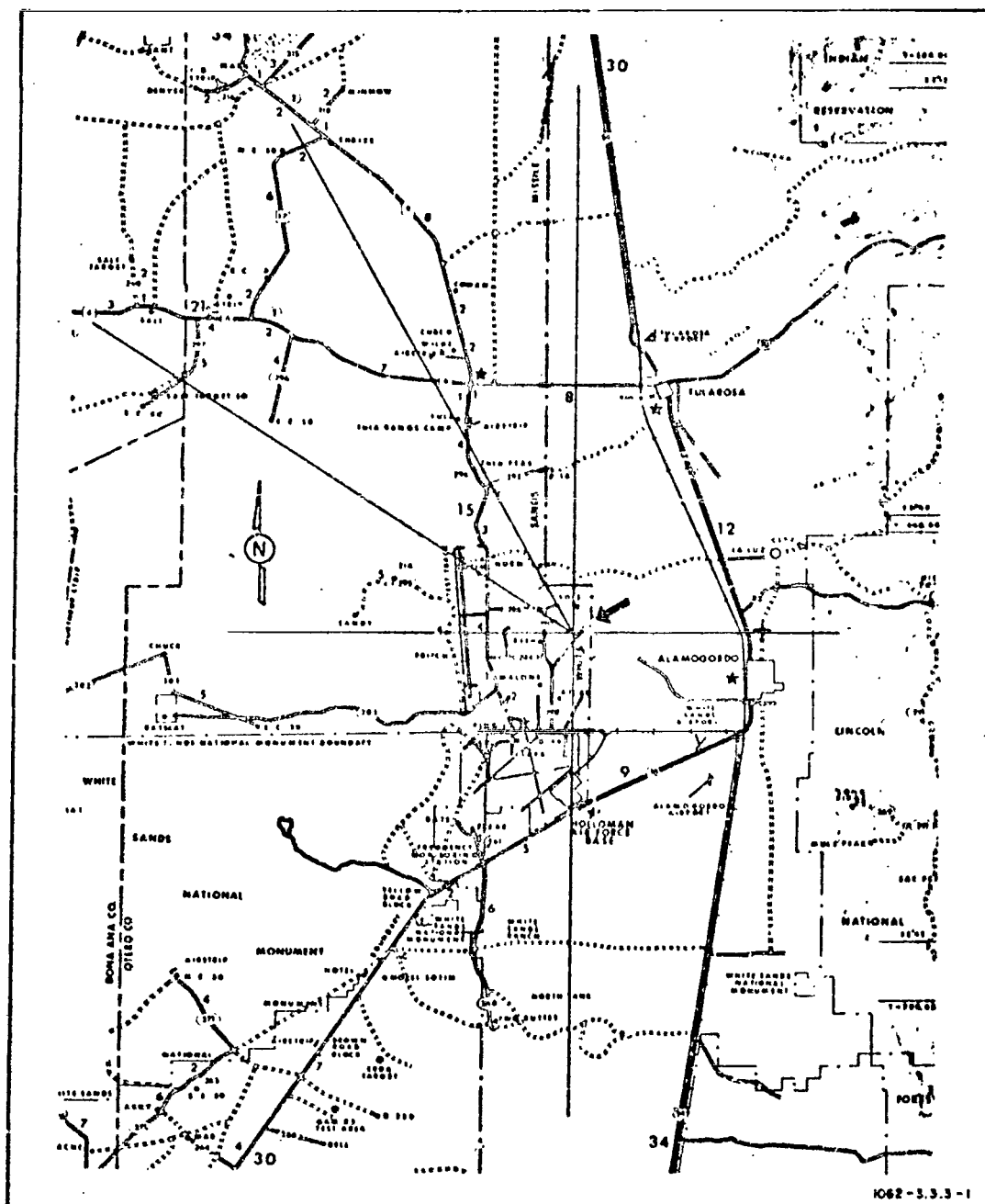


Figure 3-18. BAPE Ground Site

The balloon was launched at 0613Z (12:15 AM MST) from a point near Upham, New Mexico (50 miles west of the tracking site) and slowly drifted eastward arriving over the tracking site at about 1041Z (4:44 AM MST). Tracking commenced at about 1130Z (5:30 AM MST) and was completed at 1415Z (8:15 AM MST). The horizontal flight profile is shown in Figures 3-19 and 3-20. Altitude, zenith angle, and slant range are shown in Figures 3-21 and 3-22 and tabulated in Table 3-1.

3.4 GROUND TRACKING STATION

The following sections describe the mobile laser tracking station which was used to track the balloon-borne payload, with laser beams. The system consisted of three basic units which were transported to the site in three trailers (see Figure 3-23). An artists conception of the system is shown in Figure 3-24. The right-hand trailer as shown in the cutaway contains the lasers, modulators power supplies and other equipment necessary to operate the laser beams. The output is transmitted through a series of mirrors in the tracking mount towards the target. The second trailer contains the tape recorders, balloon control system telemetry, and other instrumentation necessary for the experiment. In actual operation the main optics of the telescope were used only for reception purposes, and the laser beams were transmitted from a port to the right of the main telescope. The artists conception is incorrect in this aspect. The system was developed for the BAPE experiment at GSFC Code 524.

3.4.1 LASER TRANSMITTER SYSTEM

The laser transmitter system, which was housed in the instrumentation trailer shown in Figure 3-23, projected its output through a tube into the tracking mount where a series of mirrors directed the radiation to the target. The transmitter system, as shown in Figure 3-25, consisted of two lasers: an RCA Model J-15268 and a Sylvania Model 948-1. Table 3-2 lists the characteristics for each of the lasers.

The lasers, which were bolted to a steel table inside the instrumentation van, remained stationary throughout the experiment. The laser beams, after being passed through collimation and alignment optics, were projected coaxially into the tracking mount. The output characteristics for the transmitter are shown in Table 3-3.

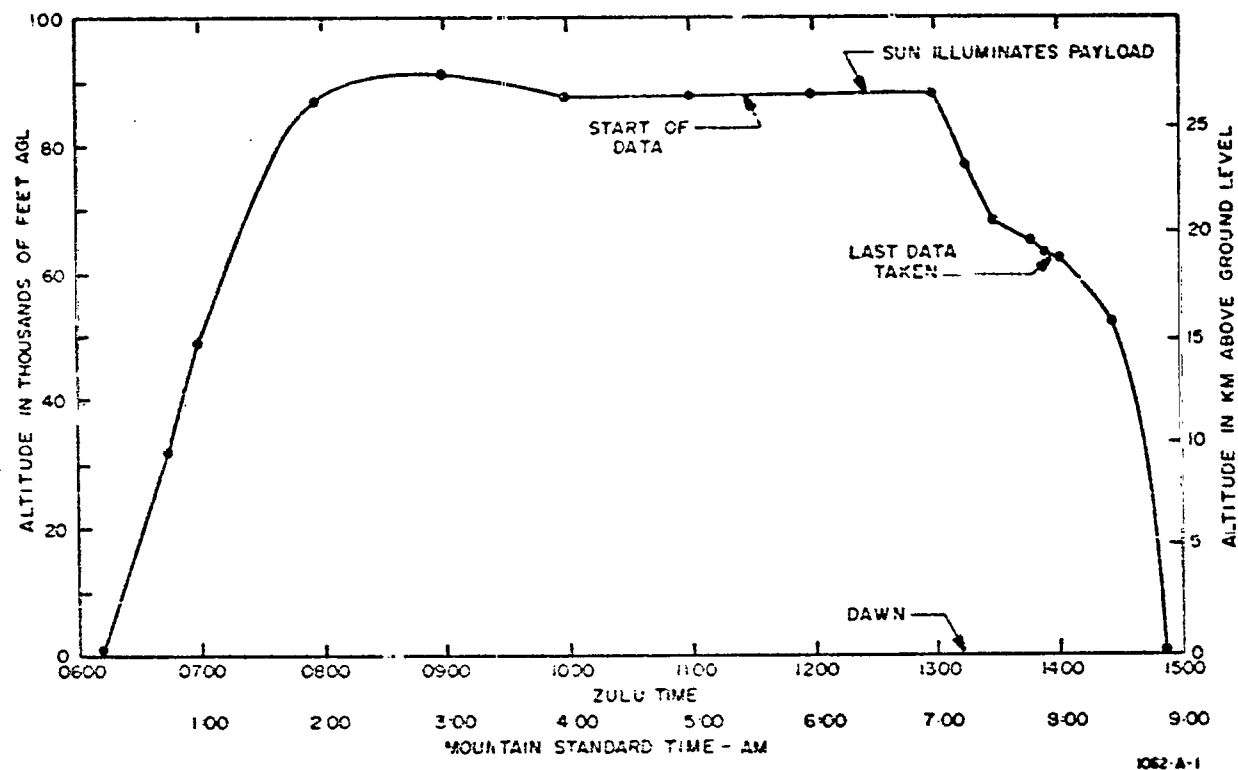
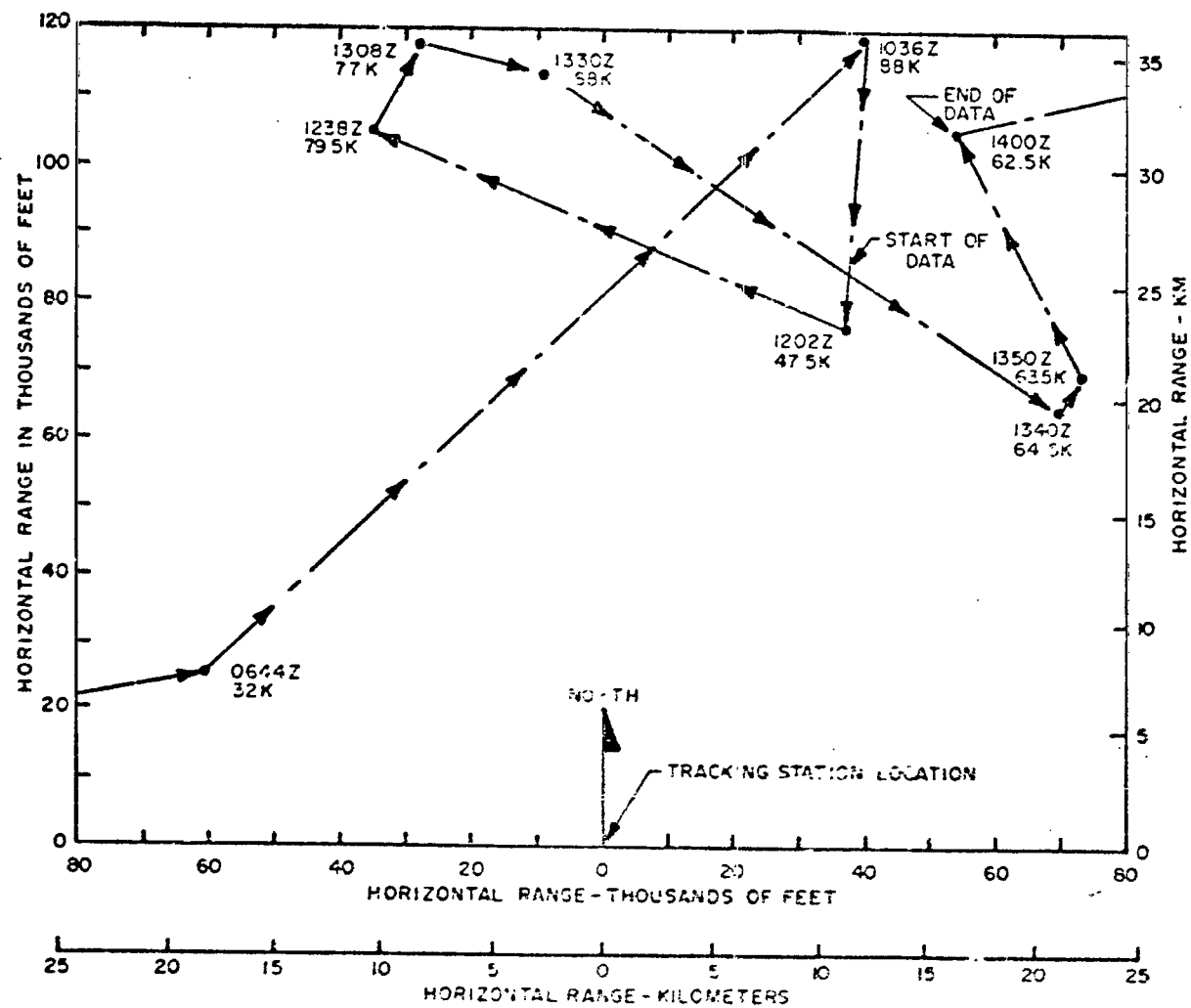
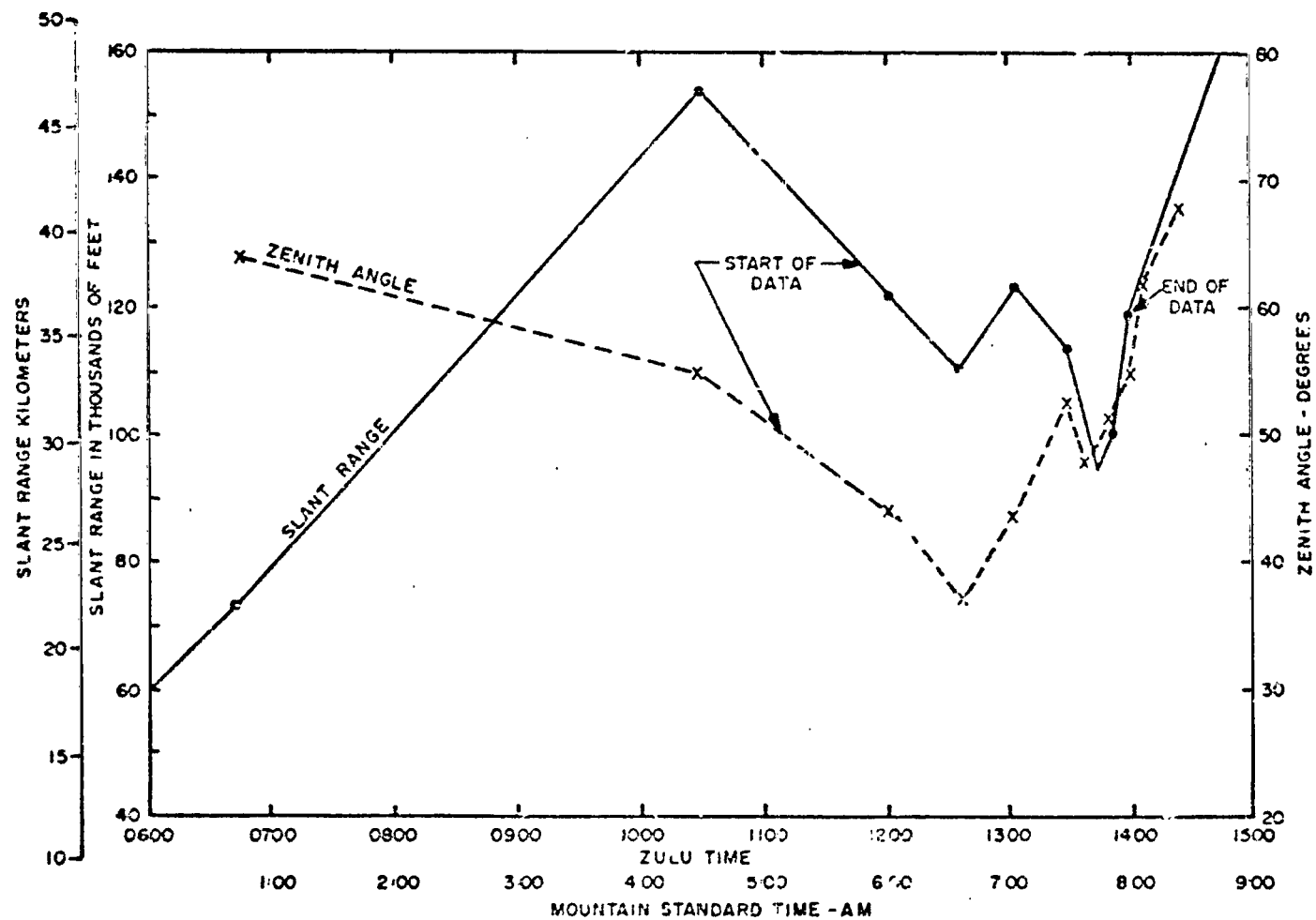


Figure 3-19. Vertical Flight Profile



1062-A-2

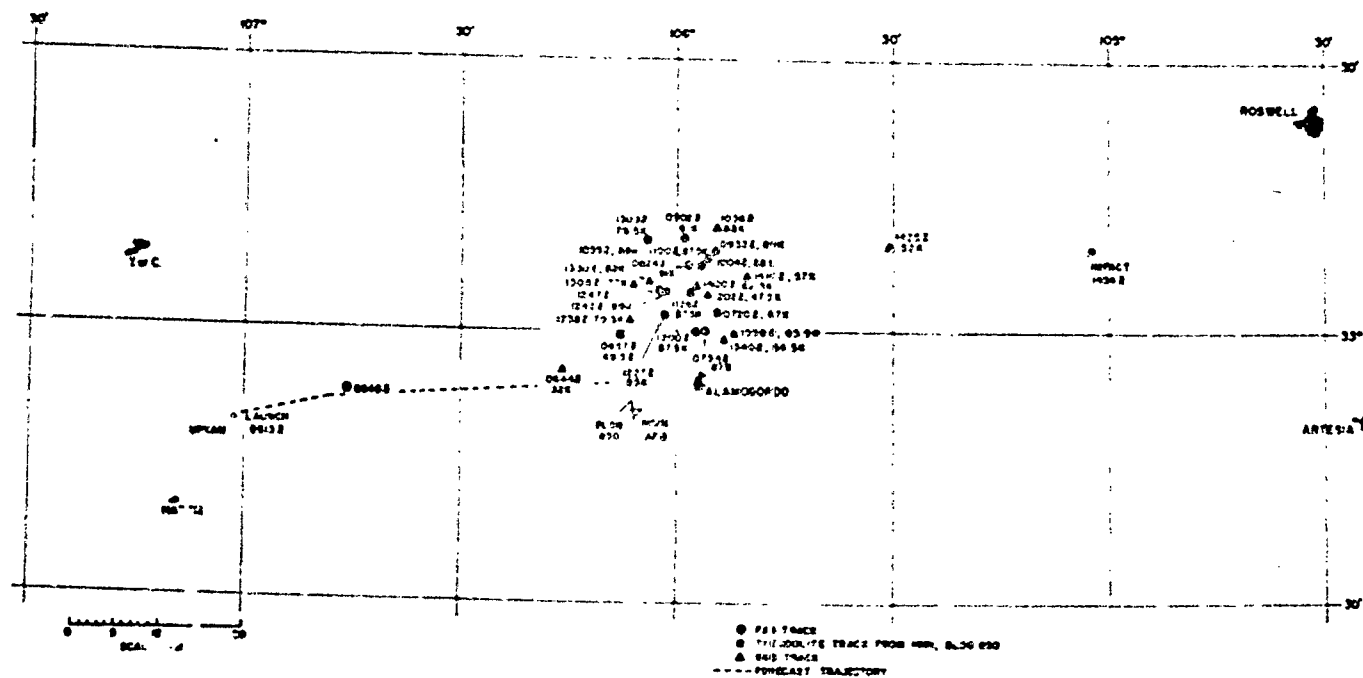
Figure 3-20. Horizontal Flight Profile.



1062-A-3

Figure 3-21. Altitude, Zenith Angle, and Slant Range

TRAJECTORY FLT. NO. H70-63
DATE 21 OCT 70



1062-3.3.3-2

Figure 3-22. Trajectory

Table 3-1
Parameters of Balloon Trajectory, October 21, 1970

Time (Z)	H	R _H	R	ϕ	Θ
0644	32,000	66,000	73,000	292°	64°
1034	88,000	127,000	154,000	19°	55°
1202	88,000	85,000	122,000	26°	44°
1238	88,000	67,000	111,000	342°	37°
1309	88,000	85,000	122,000	347°	44°
1330	68,000	81,000	114,000	356°	53°
1340	64,500	79,000	95,000	47°	47°
1350	63,500	79,000	101,000	47°	51°
1400	62,500	91,000	119,000	27°	55°
1410	57,000	109,000	12 ,000	35°	62°
1425	52,000	134,000	144,600	57°	68°

H - Altitude in thousands of feet

R_H - Horizontal Range in thousands of feet

R - Slant Range in thousands of feet

ϕ - True azimuth in degrees

Θ - Zenith angle in degrees

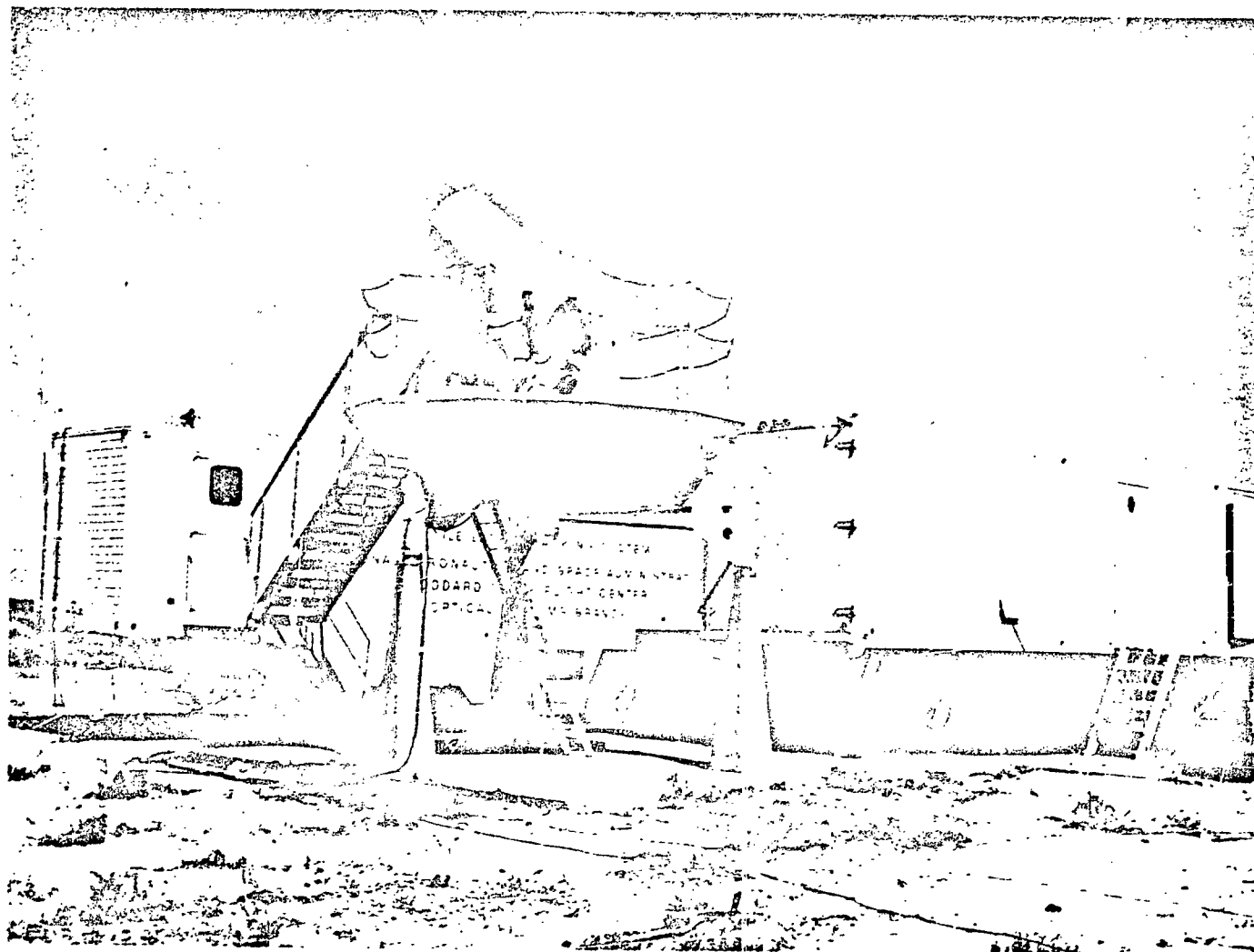
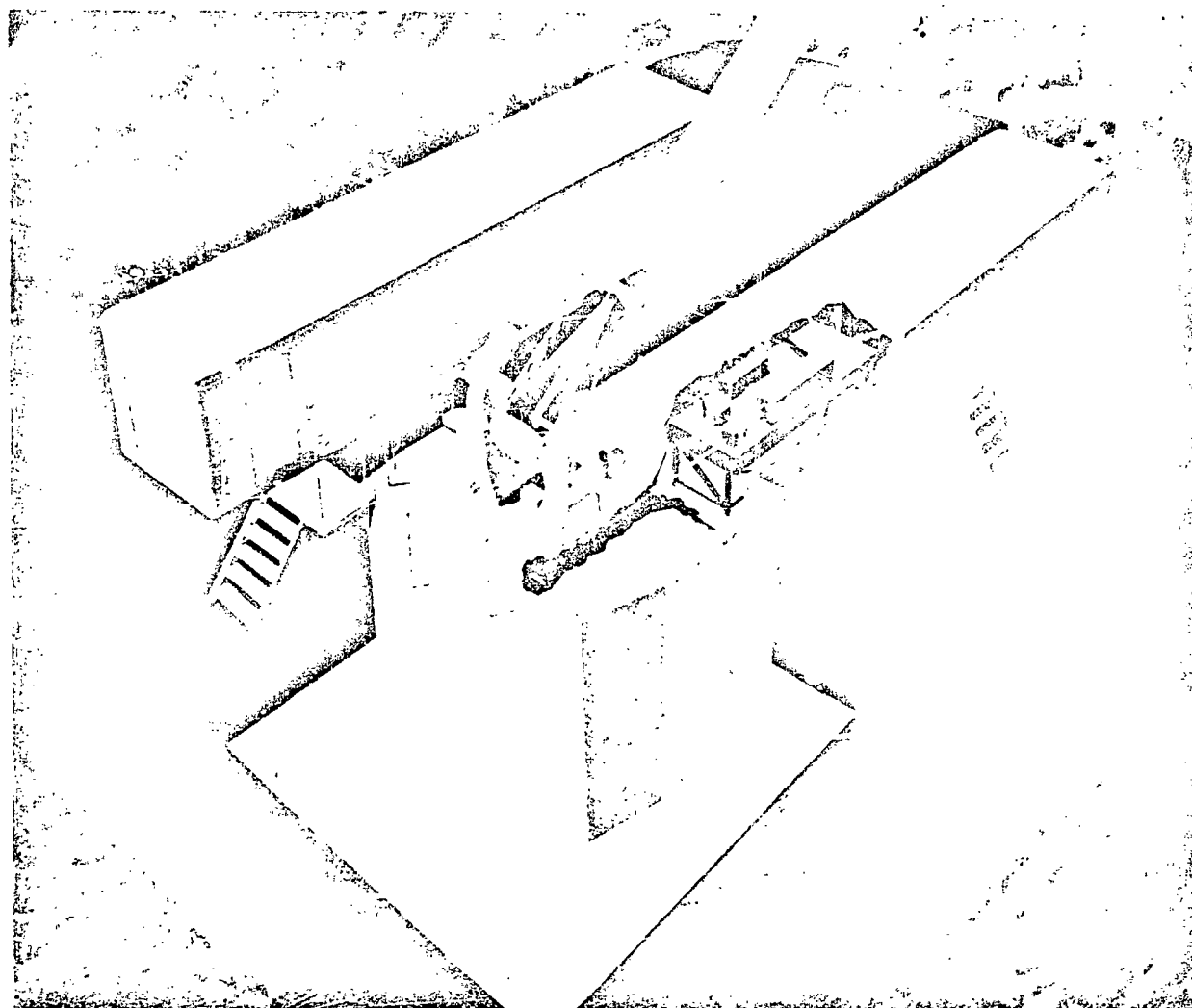
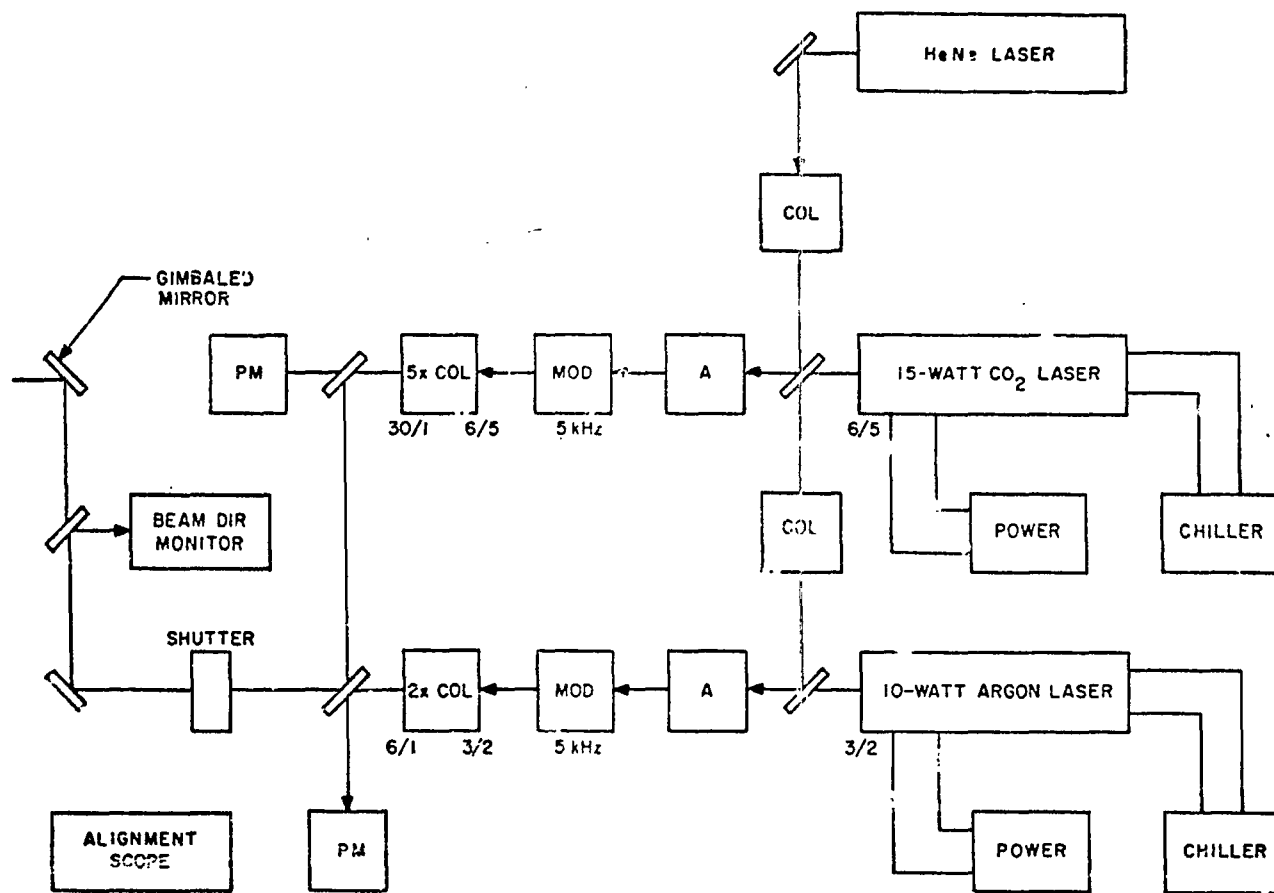


Figure 3-23. BAPE Instrumentation Trailer



NASA G-70-3960

Figure 3-24. BAPE Mobile Tracking Station



552B - 3.4.2-1

Figure 3-25. BAPE Transmitter System Block Diagram

Table 3-2
Laser Characteristics

Characteristic	Value	
	RCA Model J-15268	Sylvania Model 948-1
Type	Argon ion	CO ₂ molecular
Mode	CW	CW
Wavelength (microns)	0.5145	10.6
Maximum output (watts)	4.3	15
Beam divergence (milliradians)	2.0	5
Beam diameter (millimeters)	4	6

Table 3-3
Transmitter Characteristics

Characteristic	Value	
	Argon	CO ₂
Wavelength (microns)	0.5145	10.6
Mode (sine wave modulated)	5 kHz	5 kHz
Power out (mean watts)	1.0	5
(peak watts)	2.0	10
Divergence (milliradians)	1.0 (1/e ²)	1.0 (1/e ²)
Near-field diameter (millimeters)	6 (1/e ²)	30 (1/e ²)

The CO₂ and argon laser beams, as shown in Figure 3-25, passed through a dichroic beam splitter, an attenuator, a 5-kHz modulator, and a collimator (5x for the CO₂ beam, 2x for the argon beam) to dichroic beam combining mirror. The combined beams then passed through a safety shutter to the two mirrors that aligned the beams to the tracking mount. The first of these mirrors was slightly transparent in the visible range, which allowed a target alignment scope to view a direction parallel and coincident to the outgoing laser beams. A beam direction monitor, located between the alignment mirrors, allowed alignment of the target alignment scope to the laser beams, but was removed when the system was in operation. The target alignment scope had a protective filter for the eyepiece which allowed the operator to view the target during laser operation. During tracking, the operator could view the target in the alignment scope through the coelostat of the tracking mount to ensure that the laser beams were on target. The operator adjusted the alignment scope crosshairs onto the target by means of the last alignment mirror in the transmitter system.

Power monitors, mounted in the system, monitored the output power of the lasers and the modulation frequency. Because of the difficulty and danger involved in aligning the

transmitter optical components with CO₂ and argon lasers, a helium-neon laser, also mounted on the transmitter table, was used as an alignment tool for the optics.

3.4.2 TRACKING MOUNT

The tracking mount, shown in Figure 3-26, received the radiation from the laser transmitter system and directed the radiation through a coelostat system to the target. A diagram of the coelostat system is shown in Figure 3-27. Radiation from the lasers traveled horizontally through a pipe from the laser van to a mirror at the bottom of the azimuth axis. (The pipe from the van to the tracking mount is shown in Figure 3-24.) This mirror deflected the laser beams to a second mirror at the top of the azimuth axis, which then deflected the beams to a third mirror at the end of the elevation axis. The third mirror deflected the laser beams to a fourth mirror located slightly to the right of the main telescope. This mirror directed the laser beams through a small tube which is, as shown in Figure 3-26, to the right and parallel to the line of sight of the main telescope. The laser beams were directed through this tube without being collimated by the receiver optics.

The receiver optics, a 450-inch (11.4 m) focal length, 30-inch (76 cm) diameter cassegrain, were used to collect laser radiation reflected from the cube corners mounted in the balloon payload, and to focus the radiation on a star tracker at the back of the telescope (see Figure 3-26). The collected radiation was used by the star tracker as a signal for automatic tracking of the target.

The tracking accuracy of the star tracker was approximately 5 arc seconds rms; however, because of intermittent loss of autotrack due to severe scintillation during the experiment, the target had to be manually tracked by the observer (shown in Figure 3-28). Manual tracking was accomplished by observing the target through a guide telescope and adjusting the main telescope by means of a joy-stick control mounted on the manual control panel. Details for the guide scope and control panel are shown in Figures 3-26 and 3-28. Tracking accuracy in the manual mode was approximately 30 arc seconds rms.

In the autotrack mode, the star tracker intermittently lost track and went into the search mode because of insufficient integration time in the star tracker circuitry. After this experiment, modifications were made to correct this problem with the star tracker circuitry, and the star tracker tracked perfectly for BAPE II flights during September of 1971.



1062-3.4.3-1

Figure 3-26. BAPE Tracking Mount

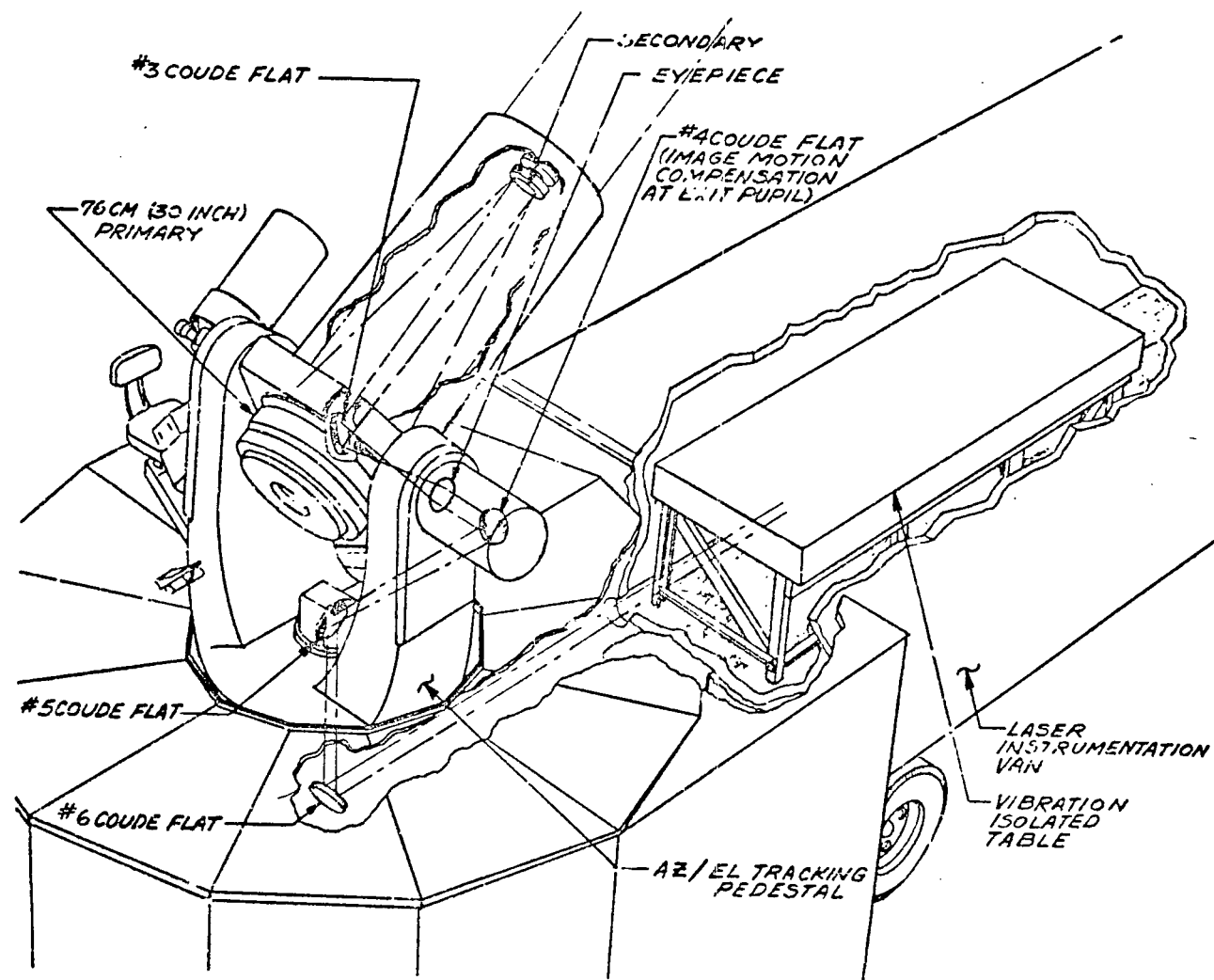


Figure 3-27. Coelostat System Diagram

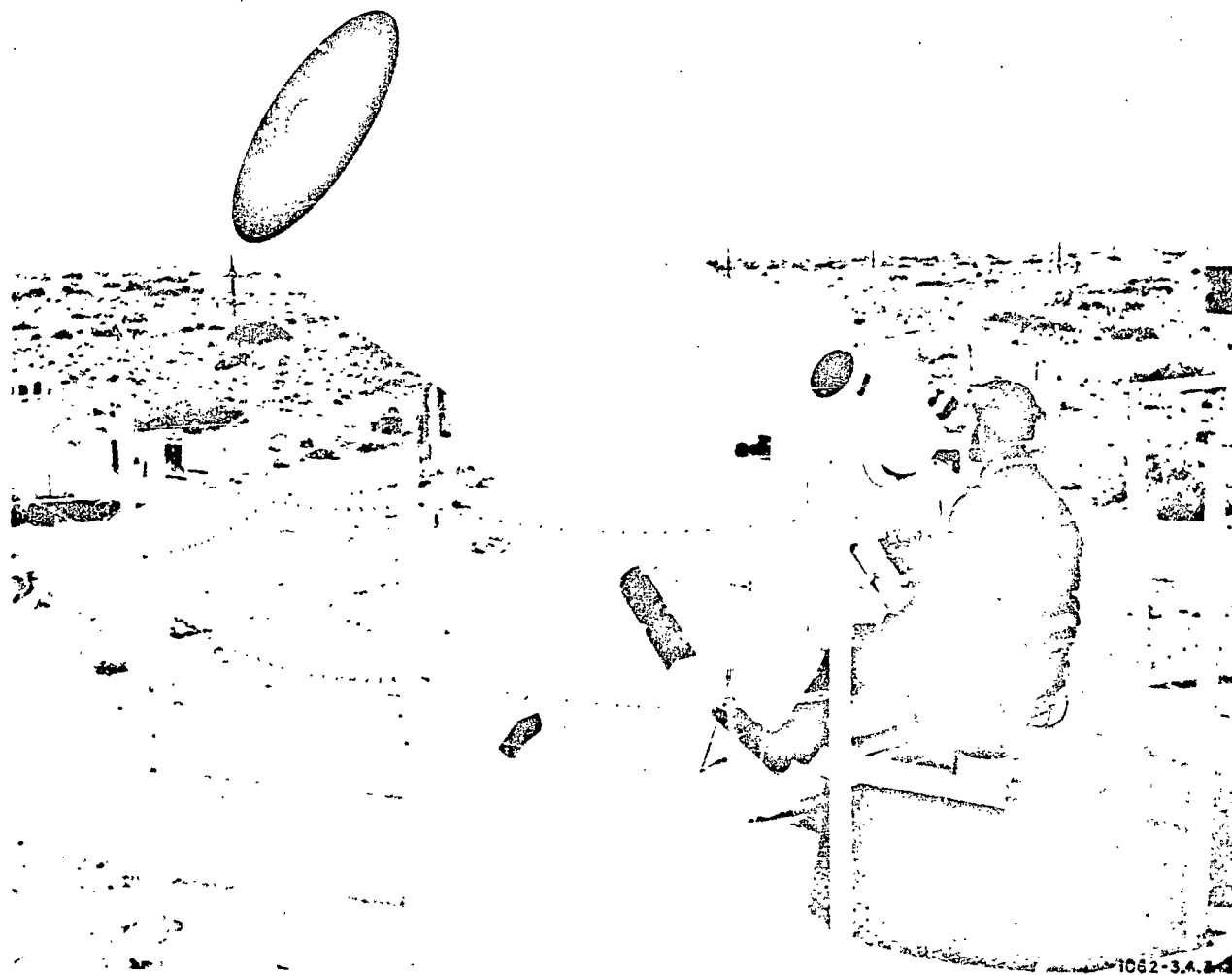


Figure 3-28. BAPE Tracking Mount

The tracking mount is a converted NIKE-AJAX tracking pedestal to which the 30 inch telescope and coelostat system have been added. During operation, the tracking mount is elevated by the aluminum legs shown in Figure 3-24 so that the elevation axis is 15 feet (5 meters) above ground level. The tracking mount is elevated for the following reasons:

- To give a clear view of the horizon over trailers and buildings in the surrounding area
- To provide a safety factor by keeping the laser beams well above personnel in the area
- To keep the laser beams above the low level ground turbulence which does not follow the normal Kolmogorov spectrum of turbulence

3.4.3 TELEMETRY, PAYLOAD COMMAND, AND DATA RECORDING SYSTEM

Command of the balloon payload and data from the balloon payload were obtained through an L- and S-band telemetry system. A console (Figure 3-29) in the instrumentation van allowed an operator on the ground to control the azimuth elevation, and operational status of the payload. Two small parabolic telemetry antennas (Figure 3-30) transmitted the information to and received information from the payload. In addition to the command and telemetry system for the payload, a standard radiosonde transmitter operating between 1660 and 1700 MHz was used to transmit data from the thermosonde to the ground. Telemetry characteristics are listed in Table 3-1.

Table 3-1
Experiment Payload Command and Telemetry

Characteristic	Value
1431-MHz command system	Conic Corp. Model CTM-UHF-305
Output	5 watts
Antenna	4-foot paraoblic, 10-inch primary beamwidth
2241.5-MHz telemetry	Conic Corp. Model CTM-UHF-305
Output	5 watts
Antenna	Hemispherical pattern, omnidirectional
1660- to 1700-MHz telemetry	Viz Mfg. Model 1091, military Model
Output	No. AN/AMT-12A
Bandwidth	400 milliwatts
Modulation	500 Hz
	100%, audio

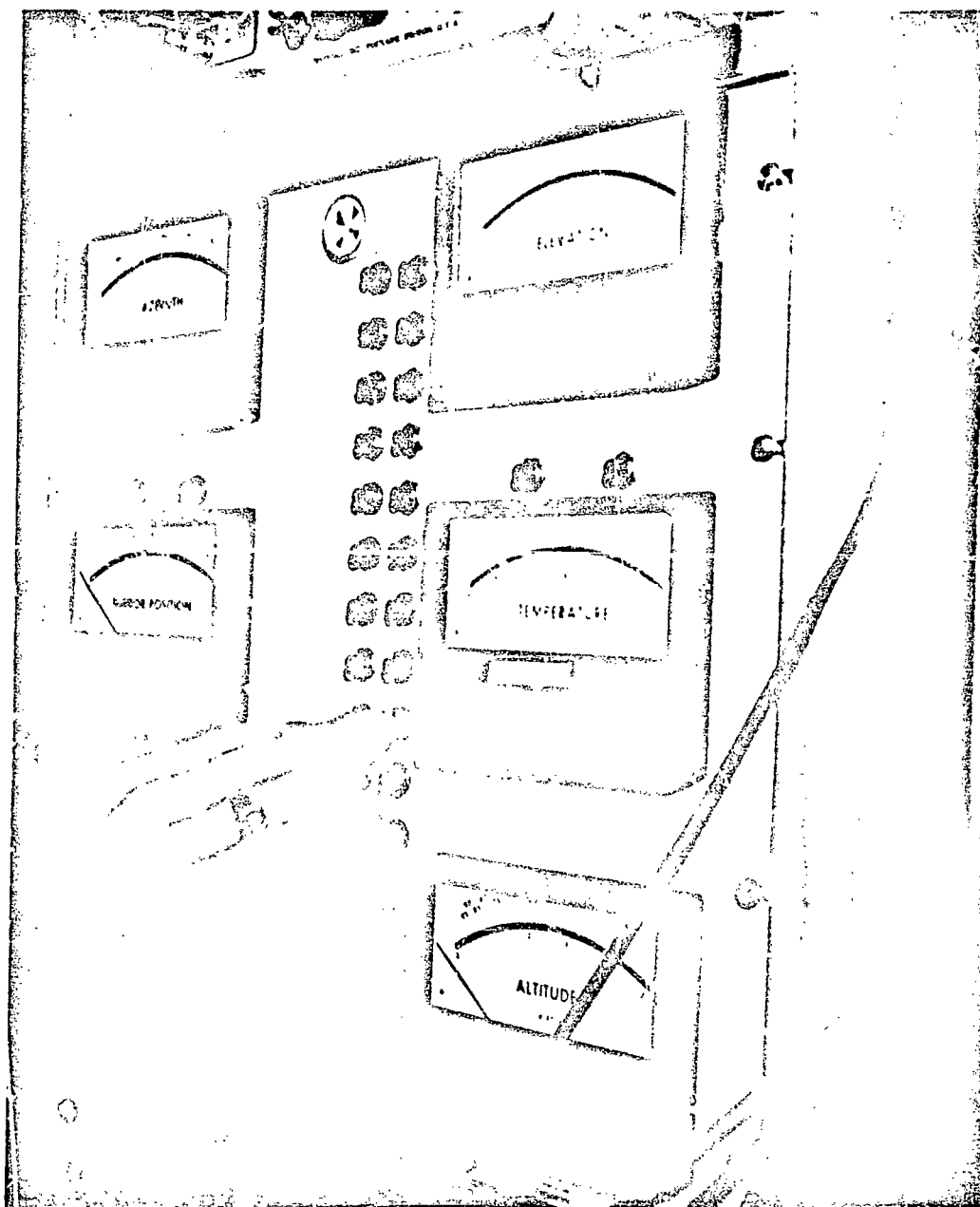


Figure 3-29. Control Console

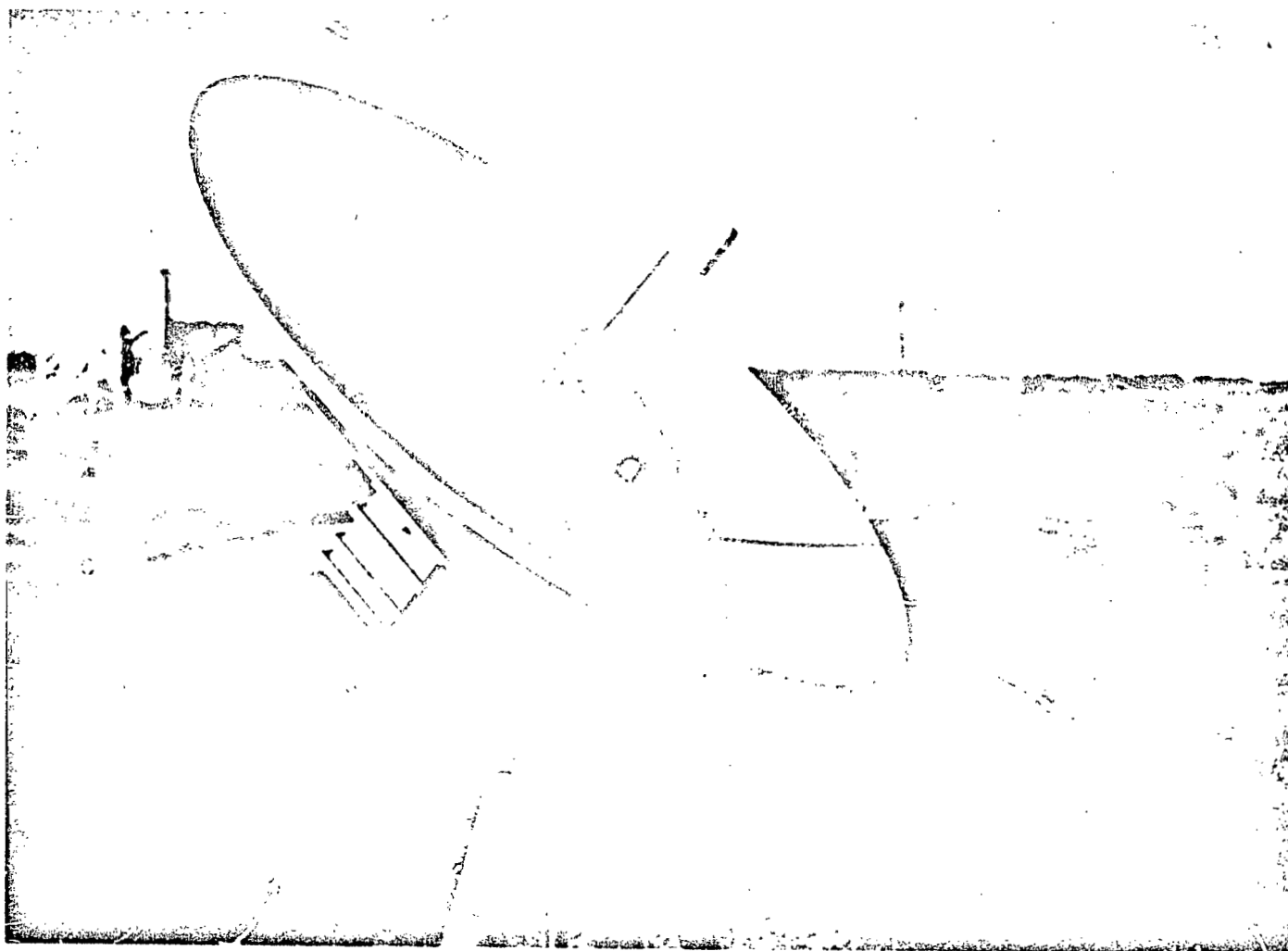


Figure 3-30. Telemetry Antenna

Downlink telemetry carrier assignments are shown in Table 3-5. The outputs of these channels were recorded on an FM tape recorder. Data recording assignments and recording circuits are shown in Table 3-6 and Figure 3-31, respectively.

Table 3-5
Downlink Telemetry Carrier Assignments

Channel	Function	Bandwidth
3B	Spare	1-kHz constant bandwidth
5B	Spare	
11B	Argon movable	
13B	CO ₂ fixed	
7B	Spare	
9B	Argon fixed	
15B	CO ₂ movable	Proportional bandwidth
4	Tracker acquisition indicator	
5	Pressure	
6	Balloon receiver AGC	
7	Commuted temperatures	
8	Mirror position	
9	Azimuth	
10	Elevation	
11	Spare	
12	Azimuth error	Proportional bandwidth
13	Elevation error	

Table 3-6
Data Recording Channels

T.R. Channel	Signal	Bandwidth	Record Module
#1	Argon A fixed	1 kHz	FM
#2	Argon B movable	1 kHz	FM
#3	CO ₂ A fixed	1 kHz	FM
#4	CO ₂ B movable	1 kHz	FM
#5	36-bit BCD time (1-kHz carrier)		Direct
#6	Balloon pack az error	DC	FM
#7	Balloon pack el error	DC	FM
#8	Star track az error	DC	FM
#9	Star track el error	DC	FM
#10	Ground rec argon demod	1 kHz	FM
#11	Ground rec CO ₂ demod	1 kHz	FM
#12	Ground comm data	DC	FM { 4 1. Track acq ind
#13	Trans power out (argon)	(5 kHz sin)	Direct 5 2. Press
#14	Trans power out (CO ₂)	DC	FM 6 3. Ball rec AGC
#1	BAPE commutated temp	DC	FM 8 4. Mirror position
#2	36-bit BCD	(1-kHz carrier)	Direct 9 5. Balloon pack.az
#3	Grd thermal sensor sig	1 kHz	FM 10 6. Balloon pack.el
#4	Grd thermal sensor sig	1 kHz	FM M 7. N/A position az
#5	Wind velocity	1 kHz	FM M 8. N/A position el
#6	rec argon	5 kHz ± 1 kHz	Direct 9. Calib
#7	Grd rec CO ₂	5 kHz ± 1 kHz	Direct 10.

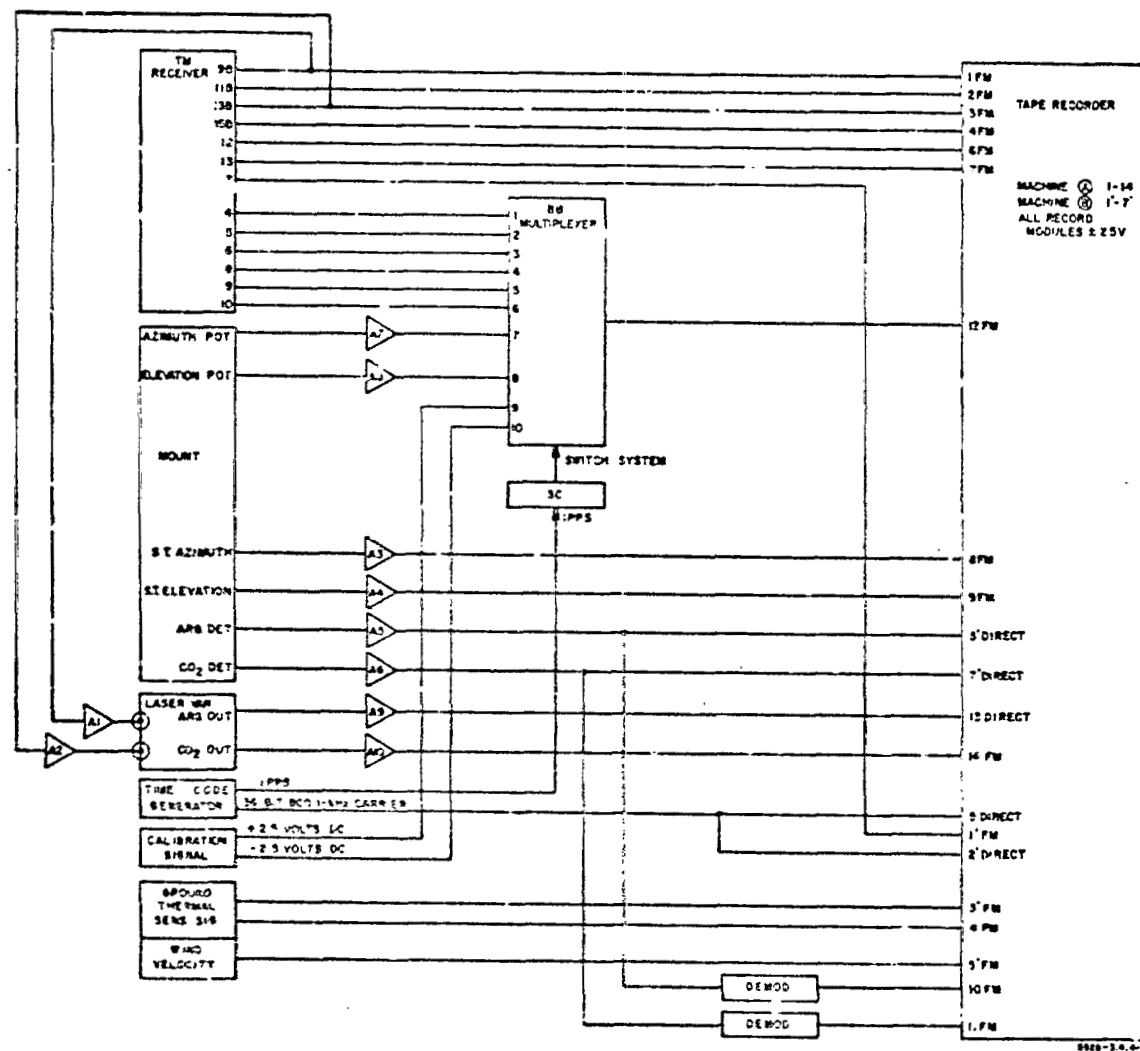


Figure 3-31. Data Recording Assignments and Circuits

REFERENCES

1. V.I. Tatarski, Wave Propagation in a Turbulent Medium, Dover Publications, Inc., New York, Chapters 6, 7, 8, 9 (1967).
2. D.L. Fried and J.D. Cloud, J. Optical Soc. Am., Vol. 56 (1966), p. 1667.
3. D.L. Fried; J. Optical Soc. Am., Vol. 57 (1967), p. 268.
4. D.L. Fried and J.B. Seidman, J. Optical Soc. Am., Vol. 57 (1967), p. 181.
5. D.L. Fried, J. Optical Soc. Am., Vol. 57 (1967), p. 989.
6. E.E. Gossard, IRE Trans. on Antennas and Propagation, Vol. 10 (1960), p. 186.
7. J.L. Lumley and H.A. Panofsky, The Structure of Atmospheric Turbulence, McGraw-Hill Book Company, Inc., New York (1961).
8. U.S. Air Force Handbook of Geophysics, The MacMillan Co., New York (1960), p. 13-2.
9. N.J. Wright and R.J. Schultz, Ballistic Research Laboratory, MR 1885 (Dec 1967).
10. G. R. Ochs, ESSA Technical Report IER 47-ITSA 46 (Oct 1967).
11. Private Communication, Ray Urtz, RADC.
12. Private Communication, Michael Fitzmaurice, GSFC.
13. J. R. Kerr, N0014-68-A-0461-0001 (July 1969).
14. Calibration will account for whatever non-uniformities remain.
15. Ed. Charles D. Dodgman, Handbook of Chemistry and Physics, Chemical Rubber Pub. Co., Cleveland, Ohio (1956), pp. 2364, 2368.
16. This circuit is the result of a collaboration with Professor J. Richard Kerr of the Oregon Graduate Center.

4. CHRONOLOGY OF EXPERIMENT

This section explains the time sequence of events which occurred during the experiments and gives a chronological description of the events.

The balloon was launched at 12:13 AM MST from Upham, New Mexico, a point nearly 50 miles west of the tracking site. The balloon ascent rate was set at approximately 1000 feet per minute. At approximately 12:15 AM MST when the balloon had risen to an altitude of 1000 feet, the reel supporting the thermosonde was released and about 20 seconds later the sonde was fully deployed 1000 feet below the main payload. At 12:30 AM MST the flashing strobe lights of the balloon were spotted from the tracking station and from that time on until termination of the experiment the tracking station was in visual contact with the balloon. The weather was clear with no clouds in sight during the experiment. High winds in the 40,000 to 80,000 ft altitude range drove the balloon quickly eastward at speeds of up to 90 knots, and by 1:00 AM MST the payload was close enough to command by telemetry. A check of payload operation was made and everything was found to be in order. During ascent, a radiosonde receiver at the launch site was able to receive data from the thermosonde to an altitude of about 20,000 feet. A second receiver, located at the tracking site with a higher gain antenna was supposed to pick up the data collection at this point but due to a malfunction was unable to operate. A baroswitch on the thermosonde automatically shut it off at 45,000 feet. After reaching a float altitude of about 92,000 feet, the balloon was slowly maneuvered towards the tracking station by slightly changing altitude to allow the prevailing winds to drive the balloon towards the tracking station. Because of the low velocity of the winds, the balloon was not within tracking range until about 5:30 AM. At 5:37 AM tracking and data taking was started and continued until 6:10 AM, at which time, data taking was stopped in order to make a quick analysis of the data to make sure that all systems were working correctly. At 7:05 AM tracking was resumed and continued until the balloon went out of range at 8:00 AM. Dawn occurred at 7:13 AM, and therefore most of the data was taken during the dawn calm, the period of lowest turbulence. At about 7:00 AM a slow descent of the balloon was started as shown in paragraph 3.3.3 and at 8:30 AM the flight was terminated. The payload descended by parachute from an altitude of 45,000 feet and landed near Roswell, New Mexico.

5. DATA REDUCTION

The following sections discuss the method of data reduction used in reducing the experiment data from raw form to final results.

5.1 THERMOSONDE DATA

Table 5-1 lists the strength of turbulence versus height as obtained from the thermosonde. Figure 5-1 shows the product of strength of turbulence, and height to the 5/6 power versus height. This product controls the strength of scintillation and therefore the figure shows that the bulk of the scintillation caused by turbulence below 6 km was caused by a layer at approximately 700 meters above the ground.

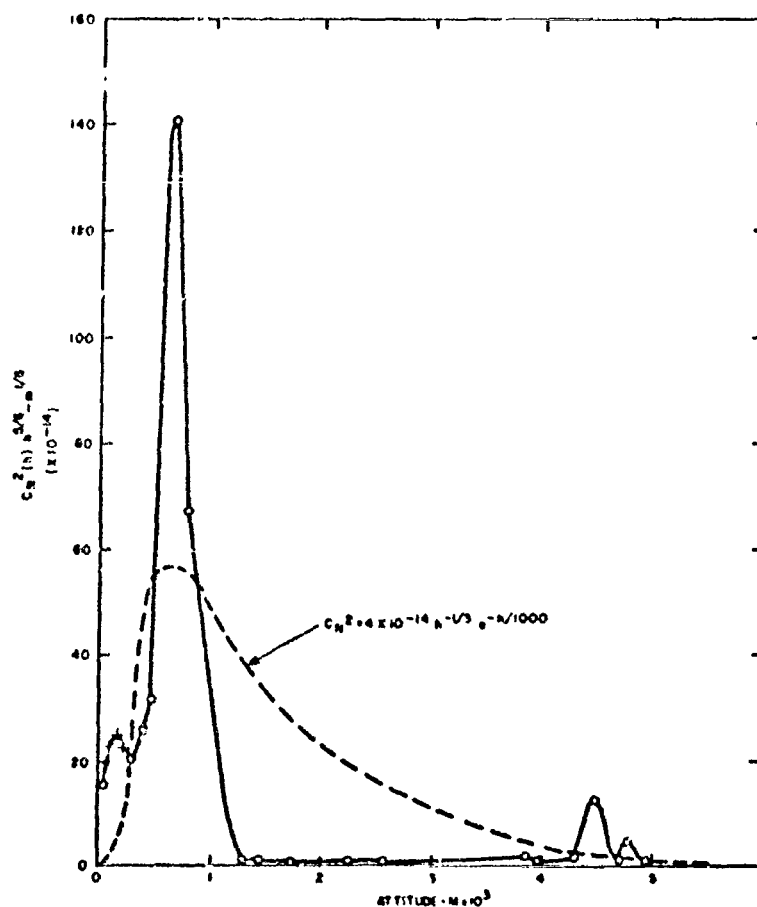


Figure 5-1

Table 5-1
Thermosonde Data

h	(h-hg)	(h-hg) ^{5/6}	(h-hg) ^{5/3}	C _N ²	C _N ² (h) (h-hg) ^{5/6}	C _N ² (h) (h-hg) ^{5/3}
Units						
m	m	m ^{5/6}	m ^{5/3}	m ^{-2/3}	m ^{1/6}	m
1490	290	113	1.28 x 10 ⁴	0.18 x 10 ⁻¹⁴	20.3 x 10 ⁻¹⁴	2.30 x 10 ⁻¹¹
1560	360	134	1.80 x 10 ⁴	0.19 x 10 ⁻¹⁴	25.6 x 10 ⁻¹⁴	3.4 x 10 ⁻¹¹
1650	450	164	2.69 x 10 ⁴	0.19 x 10 ⁻¹⁴	31.2 x 10 ⁻¹⁴	5.11 x 10 ⁻¹¹
1850	650	210	4.84 x 10 ⁴	0.64 x 10 ⁻¹⁴	141 x 10 ⁻¹⁴	3.10 x 10 ⁻¹⁰
1980	780	260	6.76 x 10 ⁴	0.26 x 10 ⁻¹⁴	67.8 x 10 ⁻¹⁴	1.76 x 10 ⁻¹⁰
2370	1270	380	1.44 x 10 ⁵	0.39 x 10 ⁻¹⁶	1.48 x 10 ⁻¹⁴	5.63 x 10 ⁻¹²
2590	1390	410	1.68 x 10 ⁵	0.24 x 10 ⁻¹⁶	0.98 x 10 ⁻¹⁴	4.03 x 10 ⁻¹²
2900	1700	500	2.50 x 10 ⁵	0.18 x 10 ⁻¹⁶	0.90 x 10 ⁻¹⁴	4.50 x 10 ⁻¹²
3400	2200	600	3.60 x 10 ⁵	0.12 x 10 ⁻¹⁶	0.72 x 10 ⁻¹⁴	4.32 x 10 ⁻¹²
3740	2540	680	4.62 x 10 ⁵	0.15 x 10 ⁻¹⁶	1.02 x 10 ⁻¹⁴	6.9 x 10 ⁻¹²
5070	3870	980	9.60 x 10 ⁵	0.21 x 10 ⁻¹⁶	2.06 x 10 ⁻¹⁴	2.02 x 10 ⁻¹¹
5145	3945	1000	1.00 x 10 ⁶	0.17 x 10 ⁻¹⁶	1.70 x 10 ⁻¹⁴	1.70 x 10 ⁻¹¹
5455	4285	1050	1.12 x 10 ⁶	0.10 x 10 ⁻¹⁶	1.06 x 10 ⁻¹⁴	1.12 x 10 ⁻¹¹
5670	4470	1100	1.21 x 10 ⁶	1.2 x 10 ⁻¹⁶	13.2 x 10 ⁻¹⁴	1.45 x 10 ⁻¹⁰
5875	4675	1130	1.28 x 10 ⁶	0.079 x 10 ⁻¹⁶	0.80 x 10 ⁻¹⁴	1.01 x 10 ⁻¹¹
5950	4750	1140	1.30 x 10 ⁶	0.41 x 10 ⁻¹⁶	4.66 x 10 ⁻¹⁴	5.33 x 10 ⁻¹¹
6090	4890	1190	1.42 x 10 ⁶	0.097 x 10 ⁻¹⁶	1.15 x 10 ⁻¹⁴	1.37 x 10 ⁻¹¹

5.2 METHOD OF OPTICAL DATA REDUCTION

Data reduction for the two channels of argon detector data and the two channels of CO₂ detector data yielded the important statistics of probability density function, cumulative density function, variance, autocorrelation, power spectral density, and cross-correlation. With the exception of power spectral density, all statistics were obtained by playing back the tape-recorded analog data into a Hewlett Packard Model 3721A correlator. This instrument is a digital signal analyzer which derives the desired statistics by sampling the input data and operating on the digital result with hardwired statistical functions. All statistics were calculated in the summation mode in which N regularly spaced samples of data are used to compute the desired statistic and the result is divided by N. The sampling rate was set at 10^3 sec^{-1} for the argon detector data and 10^2 sec^{-1} for the CO₂ detector data. These were chosen from estimates of signal bandwidths to be small enough so that no aliasing errors were present. The value of N was set at 3.2×10^4 or 6.4×10^4 which provides, for example, a statistical average over 32 or 64 seconds of data when a 0.001-second sampling interval is used. The resultant statistic was displayed as an X-Y plot on a CRT display or hard-copied on a standard X-Y ink recorder. The output display had a resolution of 100 points equally spaced across the horizontal axis.

Resolution was 200 levels for the full vertical axis and was complemented by interpolation between points on the display.

The first processing of the data was done in the autocorrelation mode. First, the dc level of the input analog data was removed and then the autocorrelation was computed. Argon detector data analysis employed the ac coupling capability of the correlator with its 1-Hz cutoff frequency. CO₂ detector data was first passed through an external high-pass filter with a 0.1 cutoff frequency and then into the dc-coupled correlator. This was done to preserve more of the typically low frequency CO₂ detector data.

The value of the autocorrelation function at time lag zero (mean square value) was read from the CRT display and written down as a function of detector number. Simultaneous data segments were analyzed for each pair of detectors. Then the cross-correlation between like detectors was computed and its value at time lag zero recorded. This value divided by the square root of the product of both individual mean square values from the autocorrelation analysis was the desired correlation coefficient. All scale factors between input irradiance at the detector and tape recorder output voltage

cancelled out when the coefficient was formed. The correlation coefficient was computed for several detector separations and the correlation function for each wavelength was determined.

The mean square values obtained above were just the data variances since the dc or average value was zero in each case. The variances were in terms of tape recorder output voltage squared. It was desirable to normalize the variances by the appropriate dc values squared in order to have a standard summary statistic for the strength of irradiance fluctuations. The dc value for each data record was obtained from the 50% level of the cumulative density function as the data was once again played back into the correlator (this time, dc coupled). It was also necessary to compute the dc value of the background (signal from detector in absence of laser irradiance) and subtract this from the data dc value before the final ratio was computed. Several cumulative density functions were also plotted on the X-Y recorder and then transferred to probability paper to test for log-normality.

The autocorrelation function was transferred to the X-Y recorder in the same manner as above and the 100 function points were fed into a digital computer. The computer was programmed to perform a Fourier transformation of each input autocorrelation function. The result was the desired power spectral density function.

Definitions of the terms used in reducing the optical data are listed below:

N — Sample time in seconds

ρ — Separation of sensors - cm

$$R_1(0) = \overline{(S_1 - \bar{S}_1)^2}$$

$$R_2(0) = \overline{(S_2 - \bar{S}_2)^2}$$

$$R_{12}(0) = \overline{(S_1 - \bar{S}_1)(S_2 - \bar{S}_2)}$$

$$\rho_{12} = \frac{R_{12}(0)}{\sqrt{R_1(0) R_2(0)}}$$

5.3 OPTICAL DATA POINTS

ARGON SCINTILLATION DATA

Start Time	N	ρ	$R_1(0)$	$R_2(0)$	$R_{12}(0)$	Rate	ρ_{12}
113700	32	6	.270	.520	.275	1 MS	.739
113825	16	6	.575	.375	.365	1 MS	.786
114005	32	8	.645	.440	.375	1 MS	.704
114150	32	12	.610	.420	.261	1 MS	.516
114420	16	16	.375	.288	.160	1 MS	.487
114443	16	16	.350	.262	.125	1 MS	.413
114624	32	26	.303	.228	.059	1 MS	.221
114805	32	33	.450	.326	.070	1 MS	.183
115122	32	50	.480	.337	.039	1 MS	.097
115513	32	50	.420	.290	.029	1 MS	.085
115910	32	50	.440	.332	.051	1 MS	.128
120497	32	35	.098	.073	.026	1 MS	.307
120930	16	20	.100	.081	.033	1 MS	.367
133336	64	16	.012	.088	.013	1 MS	.400
131315	16	14	.180	.158	.061	1 MS	.362
131255	32	12	.153	.153	.073	1 MS	.477
131450	64	8	.160	.150	.103	1 MS	.665
131710	32	6	.171	.156	.125	1 MS	.772
132010	32	4	.153	.146	.120	1 MS	.803
132100	64	3	.118	.148	.120	1 MS	.811
132545	32	2	.124	.124	.116	1 MS	.921
132708	32	2	.110	.124	.114	1 MS	.919
132916	64	2	.116	.120	.112	1 MS	.949
133212	32	3	.211	.163	.168	1 MS	.906
133440	32	4	.298	.185	.173	1 MS	.741
133540	32	5	.318	.185	.168	1 MS	.693
133800	32	5	.320	.191	.200	1 MS	.809
133900	32	6	.295	.165	.155	1 MS	.703
134013	32	7	.360	.189	.183	1 MS	.702
134115	32	8	.365	.202	.180	1 MS	.663
134210	64	10	.470	.240	.154	1 MS	.459
134330	32	12	.430	.242	.128	1 MS	.397
134455	64	14	.280	.200	.088	1 MS	.372
134615	32	16	.202	.171	.058	1 MS	.317
134730	32	22	.218	.171	.041	1 MS	.212
135120	32	50	.263	.197	.018	1 MS	.079
135500	64	60	.306	.213	.016	1 MS	.062
135720	32	70	.310	.210	.020	1 MS	.078
135900	32	80	.280	.187	.014	1 MS	.061

5.3 OPTICAL DATA POINTS (Cont)

CARBON-DIOXIDE SCINTILLATION DATA

Start Time	N	ρ	$R_1(0)$	$R_2(0)$	$R_{12}(0)$	Rate	ρ_{12}
113825	1	8	.0200	.0355	.0184	3.33 MS	.691
114005	8	10	.0253	.0185	.0191	3.33 MS	.860
114150	8	14	.0311	.0240	.0191	3.33 MS	.725
114420	16	18	.0279	.0191	.0089	1 MS	.386
114443	16	18	.0202	.0100	.0110	1 MS	.774
114631	32	28	.0290	.0161	.0084	1 MS	.359
114905	32	37	.0220	.0194	.0133	1 MS	.644
115132	32	52	.0268	.0240	.0160	1 MS	.631
115320	32	52	.0240	.0195	.0110	1 MS	.506
115850	32	52	.0180	.0198	.0079	1 MS	.416
120810	32	37	.0140	.0080	.0002	1 MS	.019
120930	32	28	.0109	.0110	.0070	1 MS	.639
130830	32	14	.0710	.090	.075	1 MS	.938
131015	32	14	.0209	.0150	.0152	1 MS	.851
131310	32	14	.067	.0460	.050	1 MS	.901
131450	64	10	.070	.054	.053	1 MS	.895
131710	32	8	.122	.135	.121	1 MS	.943
132010	32	6	.086	.090	.087	1 MS	.949
132310	32	5	.078	.0480	.059	1 MS	.964
132555	32	4	.064	.047	.054	1 MS	.985
132710	31	4	.076	.053	.063	1 MS	.993
132930	64	4	.113	.070	.082	1 MS	.922
133240	16	5	.073	.092	.075	1 MS	.915
133445	32	6	.064	.0485	.046	1 MS	.826
133545	32	7	.052	.078	.057	1 MS	.895
133800	32	7	.082	.090	.077	1 MS	.896
133900	32	8	.061	.092	.061	1 MS	.863
134025	32	9	.037	.064	.040	1 MS	.822
134115	32	10	.071	.128	.080	1 MS	.839
134210	64	12	.083	.081	.051	1 MS	.714
134330	32	14	.075	.110	.069	1 MS	.760
134455	64	16	.078	.093	.070	1 MS	.813
134615	32	18	.087	.075	.067	1 MS	.829
134730	32	24	.069	.080	.058	1 MS	.781
134845	32	28	.074	.089	.064	1 MS	.789
135000	32	32	.063	.061	.047	1 MS	.758
135320	32	.048	.048	.041	.0168	1 MS	.379
135500	64	.05	.035	.051	.021	1 MS	.397
135720	32		.071	.086	.044	1 MS	.563
135900	32		.155	.102	.075	1 MS	.581

6. DATA ANALYSIS

6.1 VERTICAL PROFILE OF TURBULENCE

Most of the estimates of the vertical profile of turbulence have been based upon measurements of stellar scintillation and astronomical seeing. Hufnagel and Stanley¹ proposed one of the first and best-known profiles and in 1968 Hufnagel² revised the profile (Figure 6-1). Fried³ proposed a mathematical model of the profile of atmospheric turbulence and has used it extensively in his numerous papers on optical propagation (Figure 6-2).

Due to the presence of a sharp temperature gradient at the tropopause, most authors have assumed that the tropopause is the major source of stellar scintillation effects. Analysis by Tatarski⁴ based upon measurements of aperture averaging by Protheroe⁵ and stellar covariance measurements by Keller⁶ tend to substantiate this hypothesis. Tatarski⁷ and Brookner⁸ have pointed out that Fried's model of the atmosphere overestimates the strength of turbulence in the first few kilometers of the atmosphere while not properly accounting for turbulence near the tropopause. The major points of evidence indicating a narrow band of high turbulence at or near the tropopause are the size of the correlation length of stellar scintillation and the correlation of the power spectral density of scintillation to wind speed at the tropopause. However, wide variations in the size of the stellar scintillation correlation distance (from 3 to 10 cm) make the determination of the altitude of the scintillation generating layers of turbulence difficult.

The strength of turbulence is normally specified by the refractive index-structure constant

$$C_N^2 = \frac{D_N(\rho)}{\rho^{2/3}} = \frac{\langle (N_1 - N_2)^2 \rangle}{\rho^{2/3}} \quad l_0 < \rho < L_0 \quad (1)$$

where N_1 and N_2 are the refractive indices at two points separated by a distance ρ . Here we have assumed the Kolmogorov⁹ similarity theory of turbulence to hold for separation (ρ) between the inner (l_0) and outer scale (L_0). The refractive index of air at optical frequencies may be expressed as a function of the properties of a gas and the wavelength through the relation

$$N = 1.0 + \frac{77.6 P}{T} \left[1 + \frac{0.0075}{\lambda^2} \right] \times 10^{-6} \quad (2)$$

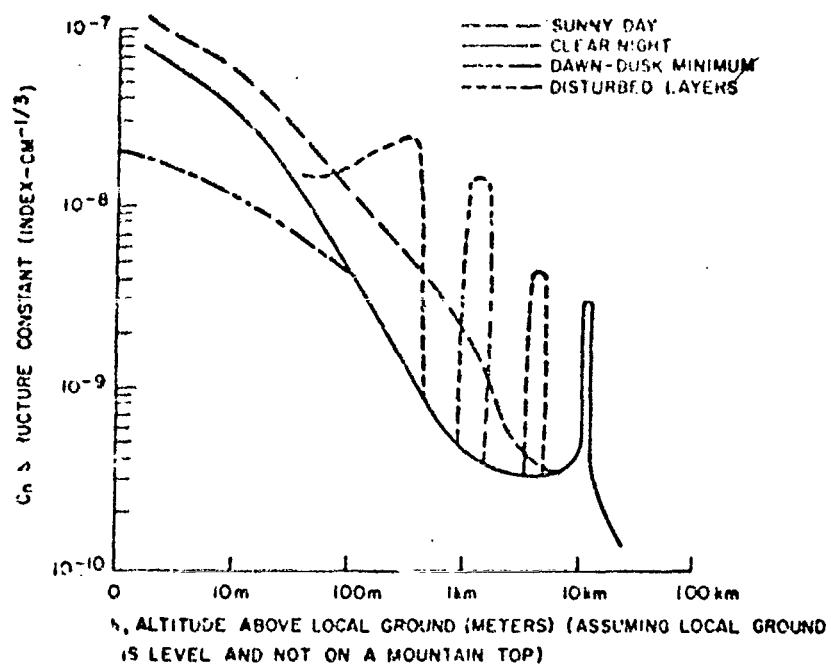


Figure 6-1. Hufnagel and Stanley Profile, Revised 1966

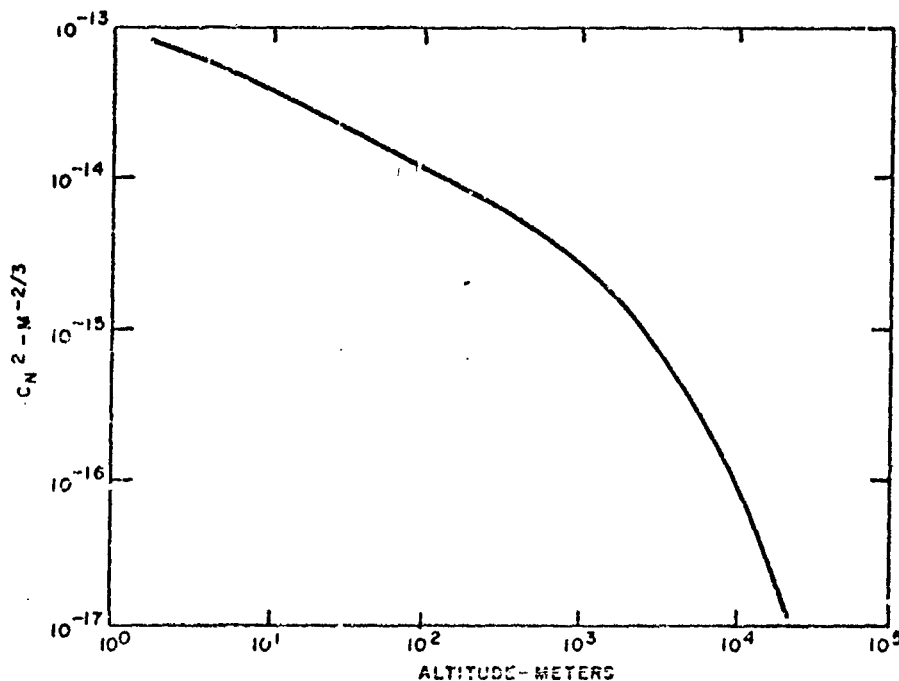


Figure 6-2. Fried's Model

where P is pressure in millibars, T is absolute temperature in $^{\circ}K$, and λ is wavelength in μm . Pressure fluctuations are rapidly damped out¹⁰ and, therefore, refractive index changes are mainly due to microthermal fluctuations.

Defining the temperature structure constant as

$$C_T^2 = \frac{D_T(\rho)}{\rho^{2/3}} = \frac{\langle (T_1 - T_2)^2 \rangle}{\rho^{2/3}} \quad l_0 < \rho < L_0 \quad (3)$$

we see that it can be easily converted to C_N^2 ;

$$C_N^2 = \left[\frac{77.6P}{T^2} \left(1 + \frac{0.0075}{\lambda^2} \right) \right]^2 C_T^2 \times 10^{-12} \quad (4a)$$

$$\approx \left[\frac{80P}{T^2} \right]^2 C_T^2 \times 10^{-12} \quad (4b)$$

Equations 3 and 4a provide the most direct method by which to obtain the vertical profile of turbulence. The temperature structure constant can be measured with a pair of low-inertia-resistance thermometers which are part of a Wheatstone bridge. The output voltage of the bridge, which is proportional to the temperature difference between the thermometers, may be amplified and the mean square obtained with suitable electronic circuits. $D_T(\rho)$ combined with data on mean pressure and temperature may then be used to compute C_N^2 . Krechmer¹¹, Tatarski¹², and Lawrence¹³ have used this method to obtain data in the first few kilometers of the atmosphere employing both aircraft and tethered balloons to elevate their instruments. Unfortunately the data extends only up to 3.5 km.

In order to compare the results of the optical measurements with theory, an instrument to measure the vertical profile of turbulence was constructed and flown as part of the balloon payload*. The device consists of a pair of low-inertia-resistance thermometers in a Wheatstone bridge with suitable processing electronics to derive C_T^2 . The device was attached to a standard MD-317A/AMT-12A radiosonde which was suspended on a 300-m cable below the main payload to avoid the turbulence effects caused by the rising balloon. The output of the resistor thermometer system was connected to one of the data channels of the radiosonde and data was telemetered to the ground in a standard telemetry format. Mean pressure and temperature were obtained from the standard radiosonde sensors**. The profile of C_N^2 obtained is shown in Figure 6-3.

Because of the rapid ascent of the balloon (1000 ft/min or 3 m/sec) the radiosonde provided only a few data points within the first few hundred meters. Therefore, Tatarski's¹⁴ method of mean temperatures was used to supplement the thermosonde data. From Figure 16 of Reference 10 we have approximated Tatarski's data by the following equations:

Stable Stratification (Temperature Inversion - Increase of mean temperature with height)

$$C_T^2 = 4 \times 10^{-2} \left| K^{2/3} h^{-1/3} T_* \right| \quad (5)$$

Unstable Stratification (Decrease of mean temperature with height)

$$C_T^2 = 5.76 K^{4/3} h^{-2/3} T_*^2 \quad (6)$$

*See Section 3.2

**See Appendix A

Where $T_1 = \bar{T}_1 - \bar{T}_2$

$$\log_{10} \left[\frac{h_1}{h_2} \right] \quad (7)$$

$$K = 0.4$$

Therefore

Stable Stratification

$$C_T^2 = 2.17 \times 10^{-2} \left| h^{-1/3} T_* \right| \quad (8)$$

$$C_N^2 = 1.47 \times 10^{-14} \left| h^{-1/3} T_* \right| \quad (P = 876 \text{ mb, } T = 280^\circ \text{K}) \quad (9)$$

Unstable Stratification

$$C_T^2 = 1.73 z^{-2/3} T_*^2 \quad (10)$$

$$C_N^2 = 1.17 \times 10^{-12} z^{-2/3} T_*^2 \quad (P = 876 \text{ mb, } T = 280^\circ \text{K}) \quad (11)$$

The experiment was performed under conditions of stable stratification with an inversion at about 180 m, as shown by the vertical dashed line of Figure 6-3. Therefore, equation 5 was used to calculate C_N^2 up to an altitude of about 80 m. The results of this analysis are shown in Table 6-1 and as crosses in Figure 6-3.

Table 6-1

h (m)	log h	$h^{-1/3}$	$T_* (^\circ \text{K})$	$C_T^2 (\text{Km}^{2/3})$	C_N^2
10	1.00	0.464	1.40	1.47×10^{-2}	1.60×10^{-14}
20	1.30	0.368	2.92	2.34×10^{-2}	1.59×10^{-14}
40	1.60	0.293	5.92	3.77×10^{-2}	2.56×10^{-14}
60	1.78	0.255	10.3	5.70×10^{-2}	3.88×10^{-14}
80	1.90	0.231	12.7	6.35×10^{-2}	4.31×10^{-14}

The profile of turbulence has been approximated by a mathematical model shown by the dashed line, which obeys the equation

$$C_N^2 = C_{N0}^2 h^{-1/3} e^{-h/h_0} \quad (12)$$

REFRACTIVE-INDEX-STRUCTURE CONSTANT AS A
FUNCTION OF HEIGHT ABOVE GROUND LEVEL.
1:00 AM MST 21 OCTOBER 1970 AT HOLLomanAFB
NEW MEXICO. BAPE I EXPERIMENT

- + DATA POINTS OBTAINED BY TATARSKI'S
METHOD OF MEAN TEMPERATURES
- DATA POINTS OBTAINED FROM THERMOSONDES
MEASUREMENT

— EXPERIMENTAL DEPENDENCE OF C_n^2 UPON
ALTITUDE

--- MATHEMATICAL MODEL USED TO REPRESENT
EXPERIMENTAL DATA

$$C_n^2 = C_{n0}^2 h^{-1/3} e^{-h/h_0}$$

$$C_{n0}^2 = 4.0 \times 10^{-14} \text{ m}^{-2/3} \quad h_0 = 1000 \text{ m.}$$

GROUND LEVEL $1.2 \times 10^3 \text{ m. ABOVE MSL}$

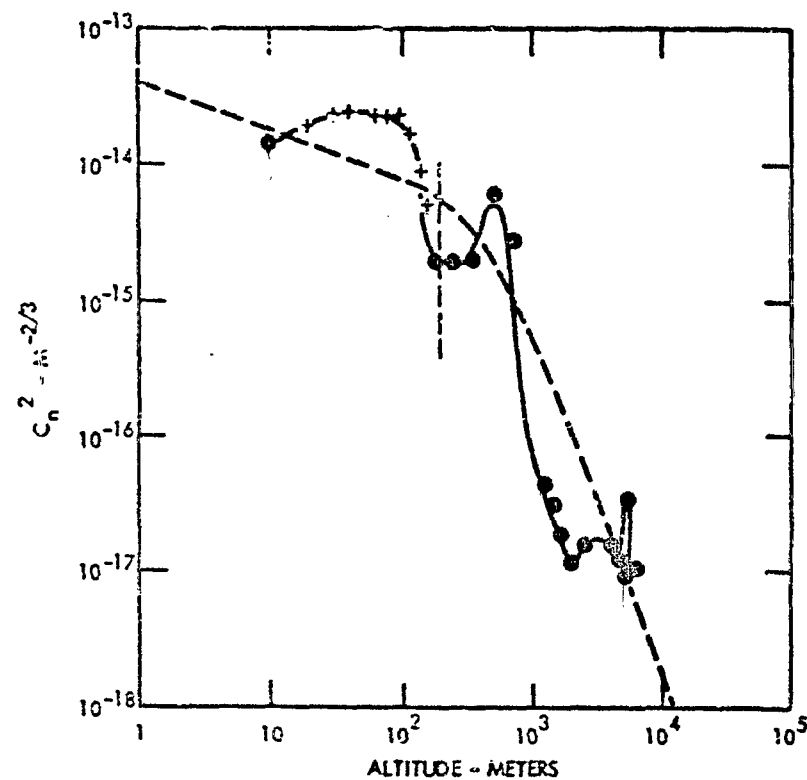


Figure 6-3

where $C_{No}^2 = 4 \times 10^{-14} \text{ m}^{-2/3}$

$$h_o = 1000 \text{ m.}$$

The value of C_{No}^2 represents the ordinate of the model at $h = 11.1$, although it has no physical significance since the refractive-index structure constant is not reliable so close to the ground. The scale height is the break point in the model, which for stable stratification normally occurs at the temperature inversion.

Two integrals of C_N^2 which will be of importance in later calculations of the scintillation statistics are

$$\int_0^\infty C_N^2(h) dh = C_{No}^2 h_o^{2/3} \Gamma(2/3) = 1.30 C_{No}^2 h_o^{2/3} (\text{m}^{1/3}) \quad (13)$$

$$= 5.20 \times 10^{-12} \text{ m}^{1/3}$$

and

$$\int_0^\infty C_N^2(h) h^{5/6} dh = C_{No}^2 h_o^{3/2} \Gamma(3/2) = 0.89 C_{No}^2 h_o^{3/2} (\text{m}^{7/6}) \quad (14)$$

$$= 1.13 \times 10^{-9} \text{ m}^{7/6}$$

Wind speed and mean temperature as a function of altitude are shown in Appendix A. No thermosonde data is available above 6 kilometers; therefore, Hufnagel's model for the tropopause turbulence is used with the integral over the tropopause equal to

$$\int_{\text{trop}} C_N^2(h) dh = 4.31 \times 10^{-13} \text{ m}^{1/3}$$

The final model of the atmosphere used for calculation of optical propagation statistics becomes

$$C_N^2 = C_{No}^2 h^{-1/3} e^{-h/h_o} + \delta(h-h_p) C_{Np}^+ \quad (15)$$

where

$$C_{No}^2 = 4.0 \times 10^{-14} \text{ m}^{-2/3} \quad h_o = 1000 \text{ m.}$$

$$C_{Np}^+ = 4.3 \times 10^{-13} \text{ m}^{1/3} \quad h_p = 13.2 \times 10^3 \text{ m}$$

REFERENCES

1. Hufnagel, R.E., and Stanley, N.R., Modulation Transfer Function Associate with Image Transmission Through Turbulent Media, J. Optical Soc. Am., Vol. 54, No. 1 (Jan 1964), pp. 52-61.
2. Hufnagel, R.E., Optical Propagation Study, Technical Report (RADC-TR-65-511, ASTIA No. AD 476244), Perkin-Elmer Corp. (Jan 1965).
3. Fried, D.L., and Cloud, J.B., Propagation of an Infinite Plane Wave in a Random Inhomogeneous Medium, J. Optical Soc. Am., Vol. 56, No. 12 (Dec 1966), pp. 1667-1676.
4. Tatarski V.I., Wave Propagation in a Turbulent Medium, McGraw-Hill, New York, Chap. 13 (1961).
5. Protheroe, W.M., Preliminary Report on Stellar Scintillation, Scientific Report 4 (AF 19 (604) - 41, ASTIA No. AD 56040), Physics and Astronomy Dept., Ohio State Univ. (Nov 1954).
6. Keller, G., Relation between the Structure of Stellar Shadow Band Patterns and Stellar Scintillation, J. Optical Soc. Am., Vol. 45 (1955), p. 845.
7. Titterton, P.J., J. Optical Soc. Am., Vol. 60 (1970), p. 417.
8. Brookner, E., Applied Optics, Vol. 10 (1971), p. 1969.
9. Kolmogorov, A.N., Dissipation of Energy in Locally Isotropic Turbulence, Doklady Akad. Nauk SSSR, Vol. 32 (1941).
10. Lumley, J. L., and Panofsky, H.A., The Structure of Atmospheric Turbulence, John Wiley and Sons, New York (1964), pp. 208-210.
11. Krechmer, S.I., Investigations of Microfluctuations of the Temperature Field in the Atmosphere, Doklady Akad. Nauk SSSR, Vol. 84 (1952), p. 55.

Krechmer, S.I., Methods for Measuring Microfluctuations of Wind Velocity and Temperature in the Atmosphere, Trudy Geofiz. Ins., Akad. Nauk SSSR, No. 24 (1954), p. 43.

Krechmer, S.I., Experimental Determination of the Characteristics of Temperature Fluctuations in the Atmosphere, Trudy Tsent. Aerolog. Observ., No. 16 (1956), p. 39.
12. Tatarski, V.I., Micro-inhomogeneities of the Temperature Field and Fluctuation Phenomena of Waves Propagating in the Atmosphere, Dissertation, Akust. Inst. Akad. Nauk SSSR, Moscow (1957).
13. Lawrence, R.S., Ochs, G.R., and Clifford, S.F., J. Optical Soc. Am., Vol. 60, pp. 826-830.
14. Ibid, Reference 4, Chapter 10.

6.2 LOG-AMPLITUDE VARIANCE AND SCINTILLATION

The strength of scintillation is often specified by the normalized power variance at the receiver;

$$\sigma_p^2 = \frac{\langle (P - \bar{P})^2 \rangle}{\bar{P}^2} \quad (1)$$

While this is a simple parameter to measure, it is not a convenient term to handle statistically. Because the power is log-normally distributed (that is the logarithm of power is normally distributed) as a consequence of the central limit theorem, it is more convenient to make calculations based on

$$\ln \frac{P}{P_0}$$

which has a normal distribution. This parameter, sometimes referred to as log-power or log intensity, may be analyzed using the normal distribution tables, and its variance is simply related to the normalized power variance

$$\langle (\ln P/P_0)^2 \rangle = \ln(1 + \sigma_p^2) \quad (2)$$

Since most of the theoretical analysis of optical propagation is done in terms of phase and amplitude, the analyst uses the term log-amplitude

$$\ln \frac{A}{A_0}$$

which also has a normal distribution. The variance of this parameter is easily related to the log-power (or log-intensity) variance

$$\langle (\ln A/A_0)^2 \rangle = \frac{1}{4} \langle (\ln P/P_0)^2 \rangle = \frac{1}{4} \ln(1 + \sigma_p^2) \quad (3)$$

In the case where $\sigma_p^2 \ll 1$, then

$$\ln(1 + \sigma_p^2) \approx \sigma_p^2 \quad (4)$$

and we can make the approximation

$$\langle (\ln A/A_0)^2 \rangle \approx \frac{\sigma_p^2}{4} \quad (5)$$

Log-amplitude variance has been represented by numerous different symbols by various authors, but we will use the terminology of Fried¹ and use $C_1(0)$ or σ_1^2 . Small letter l will be used to represent log-amplitude.

If a laser beam is transmitted from an optical system which allows for the adjustment of the aperture and radius of curvature of the emergent wavefront, the scalar wave function at the optical system output ($z = 0$) is

$$\mu_0(r)|_{z=0} = \exp \left[-\frac{\rho^2}{2\sigma_0^2} + i k \rho^2 / 2R \right] \quad (6)$$

where $k = 2\pi/\lambda$, ρ is the radial component of r , and z is the axial component of r . Let the beam have a central amplitude of unity and a normal radial distribution with variance σ_0^2 ; then from Schreitzer²

$$C_1(0) = - (k^2/8\pi) \operatorname{Re} \left(\int_0^z ds \int_0^\infty d\sigma \phi(\sigma^{1/2}; s) \right. \\ \times \exp \left[(\sigma/4) \gamma(z, s) \right] \left\{ \exp \left[(c/4) \gamma(z, s) \right] \right. \\ \left. \left. - \exp \left[(c'/4) \gamma'(z, s) \right] \right\} \right) \quad (7)$$

R has been chosen such that a positive R means a divergent laser beam, and the integration is along the propagation path from $s=0$ at the source to $s=z$ at the receiver. From the Kolmogorov theory of turbulence³

$$\phi(\sigma; s) = 8.16 C_N^2 \sigma^{-11/3} \quad (8)$$

The gamma function is defined

$$\gamma(z, s) = \left[2(z-s)/ik \right] \left[(s - ik\alpha^2)/(z - ik\alpha^2) \right] \quad (9)$$

$$\text{where } \frac{1}{\alpha^2} = \frac{1}{\sigma_0^2} - \frac{ik}{R} \quad (10)$$

Combining equation 7 and equation 8 to obtain an expression for log-amplitude variance

$$C_1(0) = \frac{8.16}{8\pi} k^2 \operatorname{Re} \left\{ \int_0^z ds C_N^2(s) \int_0^\infty d\sigma \sigma^{-11/3} \left(\exp \left\{ (\sigma/2) \operatorname{Re} \left[\gamma(z, s) \right] \right\} - \exp \left[(\sigma/2) \gamma(z, s) \right] \right) \right\} \quad (12)$$

$$\text{For } \alpha_0 = 0 \quad \gamma(z, s) = \frac{2(z-s)}{ik} \left(\frac{s}{z} \right) \quad (13)$$

$$\begin{aligned} C_1^s(0) &= \frac{8.16}{8\pi} \Gamma(-5/6) k^2 \text{Re} \left\{ \int_0^z ds C_N^2(s) \left[-1/2 \text{Re} \gamma(z, s) \right]^{5/6} \left[-1/2 \gamma(z, s) \right]^{5/6} \right\} \\ &= \frac{8.16}{8\pi} \Gamma(-5/6) k^{7/6} \text{Re} \left\{ \int_0^z ds C_N^2(s) \left[(z-s) \left(\frac{s}{z} \right) \right]^{5/6} \right\} \end{aligned} \quad (14)$$

$$\text{For } \Gamma^{5/6} = 0.259 + 0.965i \quad \Gamma(-5/6) = 6.68$$

$$C_1^s(0) = 0.56 k^{7/6} \int_0^z ds C_N^2(s) \left[(z-s) \left(\frac{s}{z} \right) \right]^{5/6} \quad (15)$$

The maximum value of $\left[(z-s) \left(\frac{s}{z} \right) \right]$ occurs when $s = z/2$ indicating turbulence halfway between source and receiver is most effective in causing scintillation. When $z \gg s_m$ where s_m is the distance at which $C_N^2(s) \rightarrow 0$.

$$C_1^s(0) = 0.56 k^{7/6} \int_0^{s_m} C_N^2(s) s^{5/6} ds \quad (16)$$

If the propagation is in a vertical direction to a receiver at altitude H and zenith angle Θ , the log-amplitude variance becomes

$$C_1^s(0) = 0.56 k^{7/6} \sec^{11/6} \Theta \int_0^H C_N^2(h) \left[(H-h) \frac{h}{H} \right]^{5/6} dh \quad (17)$$

Or for $H \gg h_m$ where h_m is the altitude at which

$$C_N^2(h) \rightarrow 0$$

$$C_1^s(0) = 0.56 k^{7/6} \sec^{11/6} \Theta \int_0^{h_m} C_N^2(h) h^{5/6} dh \quad (18)$$

It should be noted that there is a reciprocity between plane wave space to earth propagation and spherical wave earth to space propagation. Because of this reciprocity, the scintillation of a star is the same as that of a ground-based laser source viewed from space, and equation 18 is the same as Tatarski's⁴ equation 8.17. This fact was used in the GEOS-II laser detector experiment in order to relate upward propagation to downward propagation. This reciprocity is also an important factor in the analysis of this experiment.

For nonpoint sources ($\alpha_0 > 0$) the expression for log-amplitude variance is more complex. This problem has been analyzed by Fried⁶ who finds that the spherical-wave, log-amplitude variance may be modified by a correction factor (Figure 6-4) which is a function of the normalized source size Ω .

$$\Omega = k \alpha_0^2 / h_0 \sec \Theta \quad (19)$$

The sources used in the experiment could not be made true point sources. Therefore, the normalized source size was made equal for both transmitters. This required that the standard deviations of beam profiles have the ratio

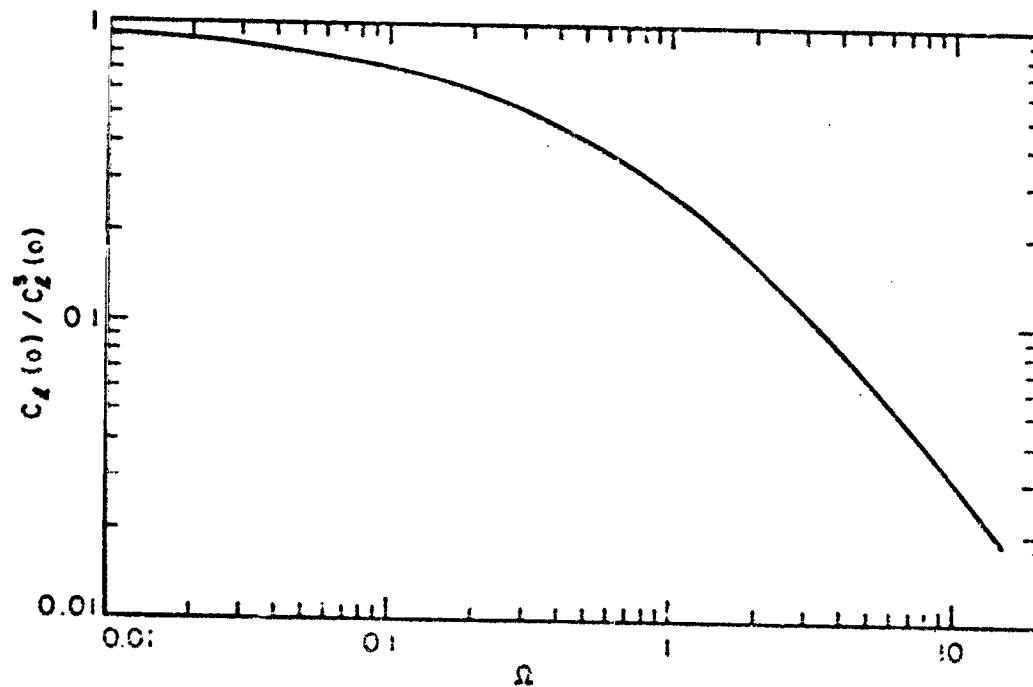
$$\frac{\sigma_{oa}}{\sigma_{ob}} = \left[\frac{k_a}{k_b} \right]^2 = \left[\frac{\lambda_b}{\lambda_a} \right]^2 = \left[\frac{10.6 \times 10^{-6}}{0.5145 \times 10^{-6}} \right]^2 = 4.55 \quad (20)$$

where subscript a refers to the argon laser ($\lambda = 0.5145 \times 10^{-6}$ m) and b to the carbon-dioxide laser ($\lambda = 10.6 \times 10^{-6}$ m). The laser outputs were made 6 mm (argon) and 30 mm (carbon-dioxide) by passing them through optical systems which were adjusted to also provide a divergence of approximately one milliradian. The optical transmitter system is described in section 3.4.1.

The normalized source size for both transmitters for the turbulence profile of the experiment at a zenith angle of 45° was

$$\Omega = k \alpha_0^2 / h_0 \sec \Theta = \frac{5.92 \times 10^5 (0.03)^2}{1000 \times 1.4} = 0.381 \quad (21)$$

which resulted in an aperture averaging correction factor of 0.5. The balloon was flown at an altitude of 28.0 km above ground level, and was at a zenith angle of approximately 45° during the period data was taken. The transmitter was located on a level plain 1.2 km above mean sea level.



1062 6.2-1

Figure 6-4. Fried's Aperture Correction Factor

Using these factors and the turbulence profile of the previous section we get (altitude of the receiver was 28.0 km above ground level) the spherical wave log-amplitude variances

$$\begin{aligned}
 C_l(0) &= 0.56 k^{7/6} \sec^{11/6} \Theta \int_0^\infty C_N^2(h) \left[(H-h) \frac{h}{H} \right]^{5/6} dh \\
 &\approx 0.56 k^{7/6} \sec^{11/6} \Theta \int_0^\infty C_{No}^2 h^{-1/3} e^{-h/h_0} h^{5/6} dh \\
 &= 1.10 k^{7/6} \left[0.89 C_{No}^2 h_0^{3/2} \right] = 1.10 k^{7/6} \left[1.13 \times 10^{-9} \right] \\
 &= 1.24 \times 10^{-9} k^{7/6} \\
 &= 1.24 \times 10^{-9} \times 1.81 \times 10^8 = 0.224 \text{ (argon)} \quad (22a)
 \end{aligned}$$

$$= 1.24 \times 10^{-9} \times 5.44 \times 10^6 = 0.00674 \text{ (carbon-dioxide)} \quad (22b)$$

After correction for aperture averaging

$$C_l(0) = 0.59 (0.224) = 0.112 \text{ (argon)} \quad (23a)$$

$$C_l(0) = 0.50 (0.00674) = 0.00337 \text{ (carbon-dioxide)} \quad (23b)$$

To these variances we must add the scintillation caused by the tropopause

$$\begin{aligned}
 C_{l(0)_{trop}} &= 0.56 k^{7/6} \sec^{11/6} \Theta C_{np} \left[(H-h_p) \frac{h_p}{H} \right]^{5/6} \\
 &= 1.10 k^{7/6} \times 4.3 \times 10^{-13} \left[(28.0 \times 10^3 - 13.2 \times 10^3) \frac{13.2 \times 10^3}{28.0 \times 10^3} \right]^{5/6} \\
 &= 6.62 \times 10^{-10} k^{7/6} \\
 &= 6.62 \times 10^{-10} \times 1.81 \times 10^8 = 0.120 \text{ (argon)} \quad (24a)
 \end{aligned}$$

$$= 6.62 \times 10^{-10} \times 5.44 \times 10^6 = 0.00360 \text{ (carbon-dioxide)} \quad (24b)$$

The total log-amplitude variance due to the turbulence near the ground plus the turbulence at the tropopause becomes

$$C_l(0) = 0.112 + 0.120 = 0.232 \text{ (argon)} \quad (25a)$$

$$= 0.00337 + 0.0036 = 0.00697 \text{ (carbon-dioxide)} \quad (25b)$$

A pair of sensors aboard the balloon payload were used to monitor the irradiance caused by the lasers. Instantaneous irradiance levels were telemetered to the ground and recorded on magnetic tape. Later, the tape was played back in 30-second intervals into a Hewlett-Packard correlator from which sample values of σ_p^2 were obtained. Normalized power variances were converted to log-amplitude variances by equation 3. Hufnagel⁷ has predicted that the strength of scintillation as measured by log-amplitude variance should itself be a log-normal parameter. Therefore, $\ln C_1(0)$ was plotted versus cumulative probability on normal graph paper to check the distribution of $C_1(0)$. A normal distribution plotted in this manner will appear as a straight line. Results are shown in Figures 6-5 and 6-6. The parameters of the distributions are listed below:

	<u>0.5145 μm</u>	<u>10.6/μm</u>
$\overline{\ln C_1(0)}$	-1.8	-5.4
$\sigma_{\ln C_1(0)}$	0.6	0.6

The magnitude of $C_1(0)$ should, from equation 15, be proportional to the 7/6 power of the wavenumber. Therefore

$$\frac{[C_1(0)]_{0.5145 \mu\text{m}}}{[C_1(0)]_{10.6 \mu\text{m}}} = \left[\frac{10.6 \times 10^{-3}}{0.5145 \times 10^{-6}} \right]^{7/6} = 34.1 \quad (26)$$

From the measured log-amplitude variances

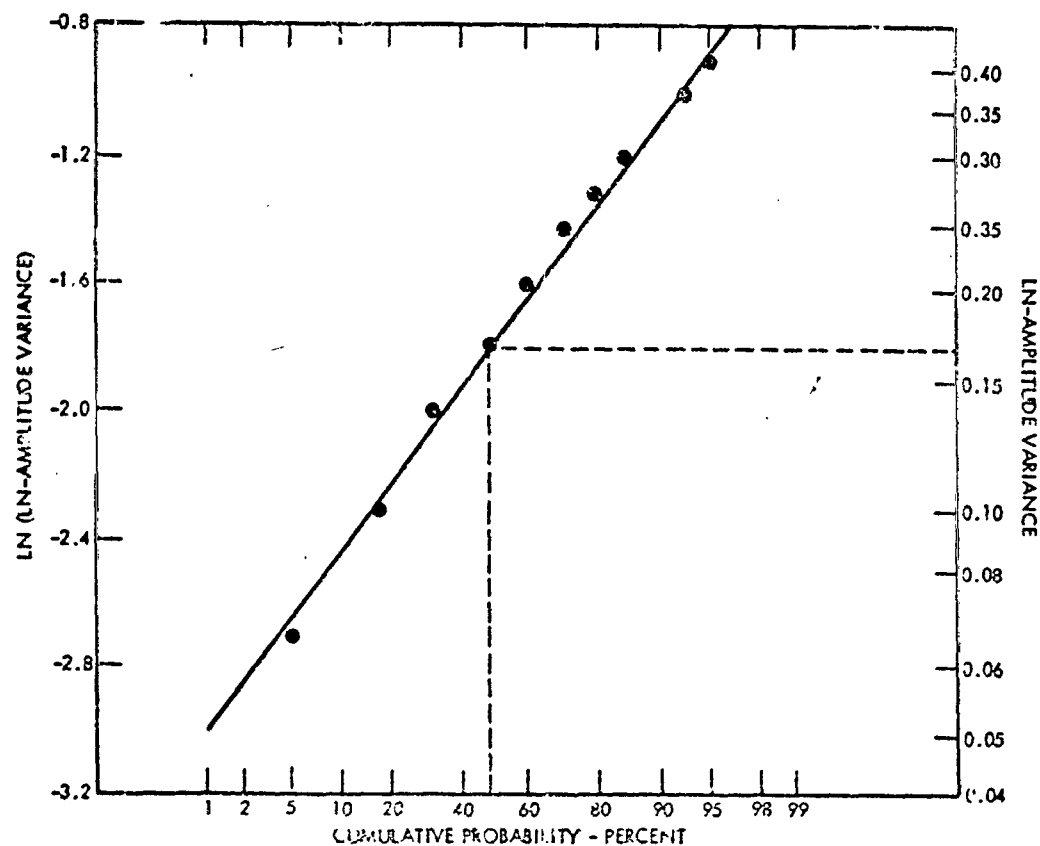
$$\frac{\text{Median}[C_1(0)]_{0.5145 \mu\text{m}}}{\text{Median}[C_1(0)]_{10.6 \mu\text{m}}} = \frac{e^{-1.8}}{e^{-5.4}} = 36.9 \quad (27)$$

The mean $C_1(0)$ from the data are*

$$\overline{C_1(0)} = e^{-1.8 + \frac{1}{2}(.6)^2} = e^{-16.2} = 0.198 \quad (0.5145 \mu\text{m}) \quad (28a)$$

$$\overline{C_1(0)} = e^{-5.4 + \frac{1}{2}(.6)^2} = e^{-5.22} = 0.0054 \quad (10.6 \mu\text{m}) \quad (28b)$$

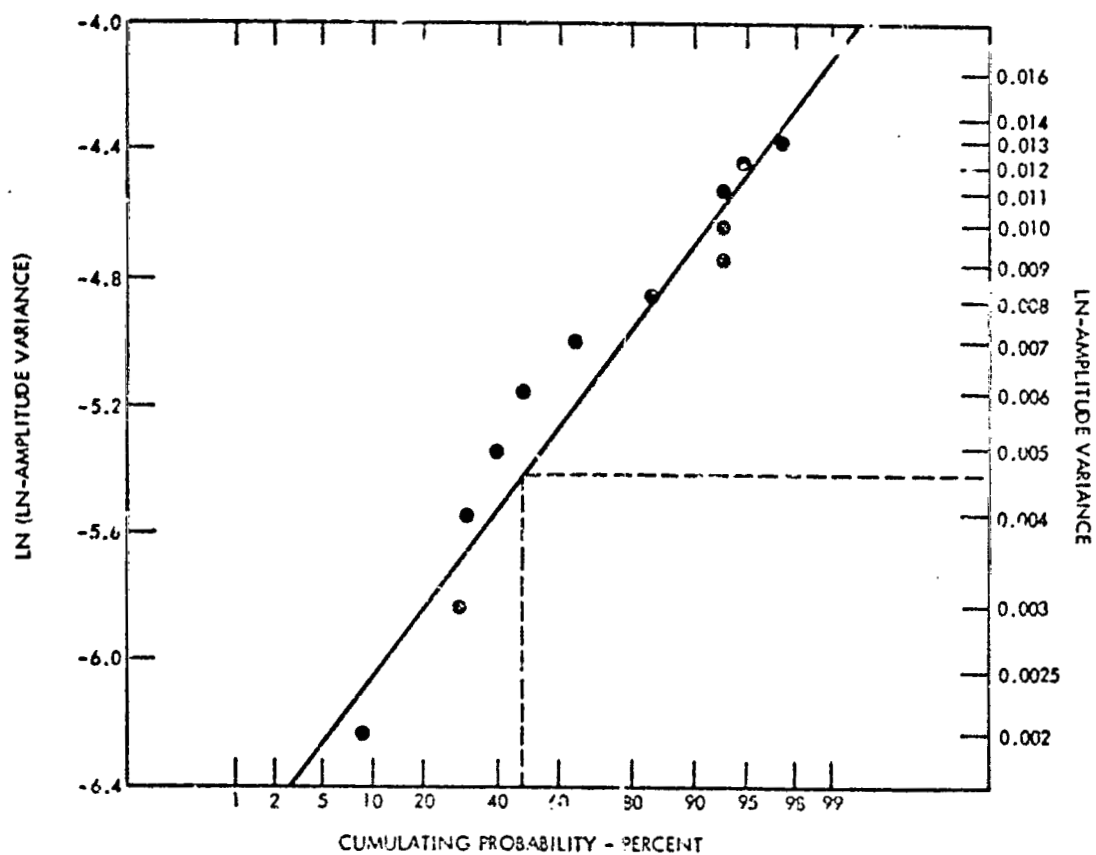
*For a log-normal variable $\mu = \exp \left[k + \frac{\lambda^2}{2} \right]$ where μ is the mean of the log-normal variable and k and λ^2 are the mean variance of the corresponding normal variables.



CUMULATIVE PROBABILITY* OF LOG-AMPLITUDE VARIANCE FOR ARGON WAVELENGTH (5145 Å) FOR A 2½ HOUR PERIOD, 4:30 - 7:00 AM MST 21 OCTOBER 1970 AT HOLLOMAN AFB, NEW MEXICO. BAPE I EXPERIMENT

*DATA PLOTTED ON NORMAL PROBABILITY SCALE. STRAIGHT LINE INDICATES NORMAL DISTRIBUTION.

Figure 6-5. Cumulative Probability of Log-amplitude Variance for Argon Wavelength



CUMULATIVE PROBABILITY* OF LOG-AMPLITUDE VARIANCE FOR CO₂ WAVELENGTH (10.6 micrometers) FOR A 2½ HOUR PERIOD, 4:30 - 7:00 AM MST 21 OCTOBER 1970 AT HOLLOMAN AFB, NEW MEXICO. BASE I EXPERIMENT

*DATA PLOTTED ON NORMAL-L PROBABILITY SCALE. STRAIGHT LINE INDICATES NORMAL DISTRIBUTION.

Figure 6-6. Cumulative Probability of Log-amplitude Variance for CO₂ Wavelength

Experimental values of $C_1(0)$ determined by optical measurement are compared to values computed from the turbulence profile in the following table:

	<u>Experimental</u>	<u>Computed</u>	<u>Exp/Computed</u>
$C_1(0) 0.5145 \mu m$	0.198	0.232	0.854
$C_1(0) 10.6 \mu m$	0.00540	0.00697	0.775

The central-limit theorem predicts that the distribution of irradiance should be log-normal. This was checked in Figures 6-7 and 6-8 by plotting the cumulative probability of the logarithm of a normalized signal on a normal distribution scale. The straight line behavior of both of these graphs again indicates a log-normal distribution.

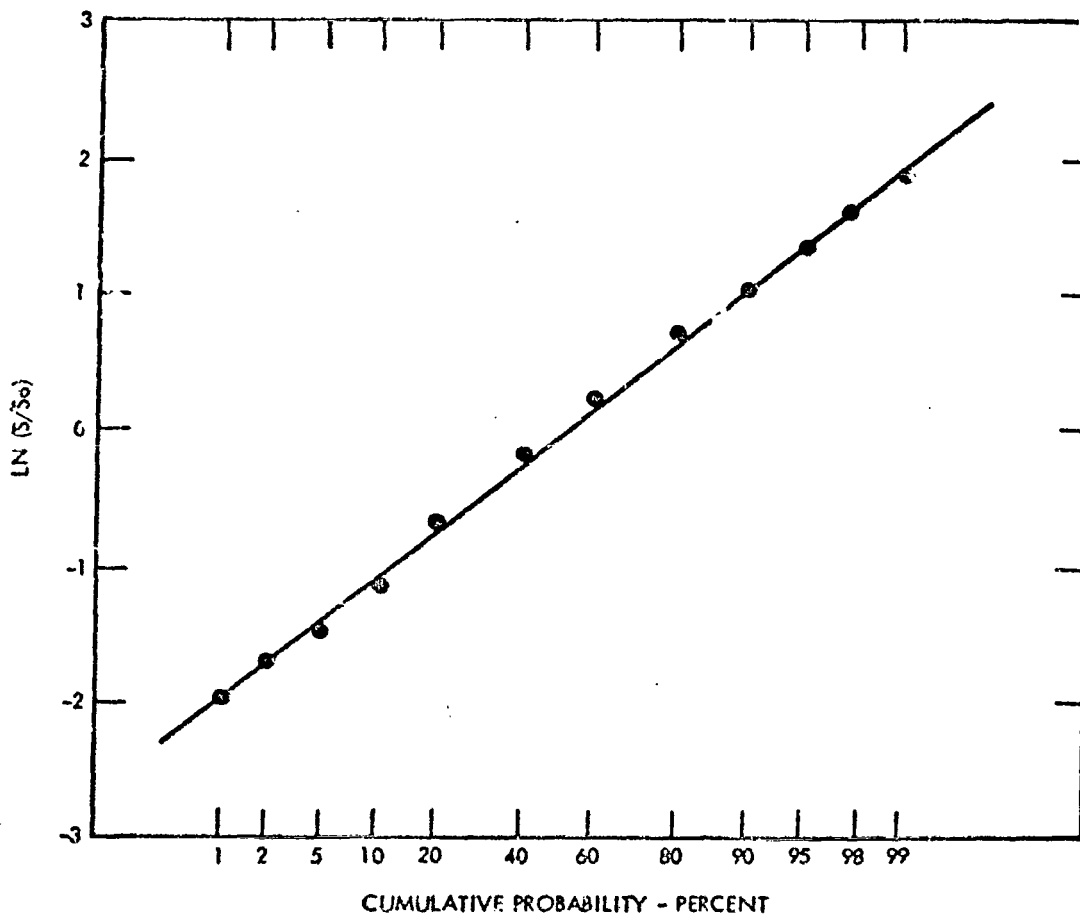
In order to assure that the experimental values of variance were not causing a scatter of the results due to insufficient sample lengths, an analysis of the statistical error was performed.

Standard statistical techniques provide a means to estimate the effect of finite data sample length. For a number, N , of independent observations of a normally distributed random variable, x , it is known that the sample variance obeys a chi-square distribution with n degrees of freedom.

$$\frac{n S^2}{\sigma_x^2} = \chi_n^2 \quad \begin{array}{l} n = N - 1 \\ S^2 = \text{sample variance} \\ \sigma_x^2 = \text{actual variance} \\ \chi_n^2 = \text{chi-square random variable} \end{array} \quad (29)$$

of chi-square determine the $1 - \alpha$ confidence interval for sample variance,

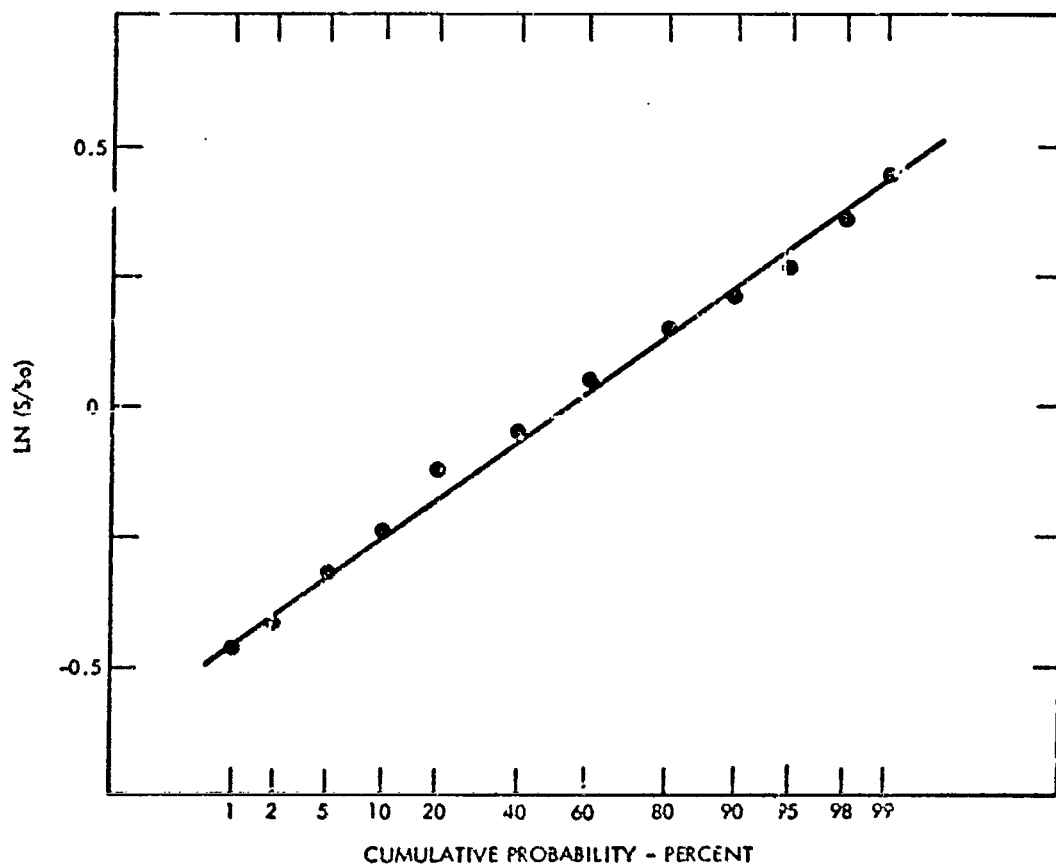
$$\frac{n}{\chi_{n; \alpha/2}^2} S^2 \leq \sigma_x^2 \leq \frac{n}{\chi_{n; 1-\alpha/2}^2} S^2 \quad (30)$$



THE LOGARITHM OF NORMALIZED RECEIVED SIGNAL(S) FOR THE ARGON WAVELENGTH (5145 Å) AS A FUNCTION OF CUMULATIVE PROBABILITY ON NORMAL PROBABILITY PAPER. 7:49:05 MST 21 OCTOBER 1970 AT HOLLOMAN AFB, NEW MEXICO. BAPE I EXPERIMENT

VARIANCE 0.72
 LOG-AMPLITUDE VARIANCE ≈ 0.18
 S_0 - MEAN SIGNAL LEVEL

Figure 6-7. Logarithm of Normalized Received Signals for Argon Wavelength



THE LOGARITHM OF NORMALIZED RECEIVED SIGNAL(S) FOR THE CO₂ WAVELENGTH (10.6 micrometers) AS A FUNCTION OF CUMULATIVE PROBABILITY ON NORMAL PROBABILITY PAPER. 6:47:30 AM MST 21 OCTOBER 1970 AT HOLLOMAN AFB, NEW MEXICO. BAPE I EXPERIMENT

VARIANCE 0.04
 LOG-AMPLITUDE VARIANCE ≈ 0.01
 S_0 - MEAN SIGNAL LEVEL

Figure 6-8. Logarithm of Normalized Received Signals for CO₂ Wavelength

that is, the actual variance σ_x^2 is known to fall within the above interval with a confidence of 100 (1 - α) percent. The key parameter that determines the above interval is N , the number of independent samples.

$$N = 2B_{eq} T \quad (31)$$

where

B_{eq} = equivalent white noise bandwidth

T = record length

B_{eq} in turn can be estimated from

$$B_{eq} = \frac{R_x(0)}{2 \int_{-\infty}^{\infty} R_x(\gamma) d\gamma} \quad (32)$$

where

$R_x(\gamma)$ = autocorrelation for random variable

Typical values of $R_x(\gamma)$ for argon and CO_2 data lead to estimates for B_{eq} and in turn N for a given sample record length, T . The value of chi-square for a particular N and is obtained from standard tables. Results are given below for a 90-percent confidence interval for each signal and a sample record length of 30 seconds.

Statistical Error Analysis

Data	B_{eq} (Hz)	N	α	$\chi_n^2; \alpha/2$	$\chi_n^2; 1-\alpha/2$
Argon	150	10,500	0.1	10,740	10,263
CO_2	35	2,100	0.1	2,208	1,995

99% confidence intervals

Argon	$0.98 S^2 \leq \sigma_1^2 \leq 1.02 S^2$
CO_2	$0.95 S^2 \leq \sigma_1^2 \leq 1.05 S^2$

Therefore the argon variance has error bars of $\pm 2\%$ and CO_2 has $\pm 5\%$ for 99% confidence and 30-second record length.

REFERENCES

1. Fried, D.L., Proc. IEEE, Vol. 55, No. 1 (Jan 1967), p.57.
2. Schmeltzer, R.A., Quart. Appl. Math, Vol. 24 (1967), p.339.
3. Kolmogorov, A.N., The Local Structure of Turbulence in Incompressible Viscous Fluid for Very Large Reynolds Numbers, Doklady Akad. Nauk SSSR 30:301 (1941). German translation in Sammelband zur Statistischen Theorie der Turbulenz, Akademie-Verlag, Berlin (1958), p.71.
4. Tatarski, V.I., Wave Propagation in a Turbulent Medium, McGraw-Hill, New York (1961).
5. Minott, P.O., Scintillation in an Earth-to-Space Propagation Path, J. Optical Soc. Am., Vol. 62 (July 1972).
6. Fried, D.L., J. Optical Soc. Am., Vol. 57 (1967), p.980.
7. Hufnagel, R.E., Restoration of Atmospherically Degraded Images, Woods Hole Summer Study, Vol. 2, Appendix 3 (1966), p. 15.

6.3 CORRELATION COEFFICIENT

The covariance of irradiance is defined as

$$C_I(\rho) \equiv \langle (I_1 - \bar{I}_1) (I_2 - \bar{I}_2) \rangle \quad (1)$$

where the angle brackets denote an ensemble average of all pairs of points in the receiving plane separated by a distance ρ . The variance of irradiance is simply the variance for zero separation

$$C_I(0) = \langle (I - \bar{I})^2 \rangle$$

In order to obtain a measure of the independence of the scintillation at two points in the receiving plane, the covariance is usually divided by the variance to obtain the irradiance-correlation coefficient

$$\gamma(\rho) = \frac{C_I(\rho)}{C_I(0)} = \frac{\langle (I_1 - \bar{I}_1) (I_2 - \bar{I}_2) \rangle}{\langle (I - \bar{I})^2 \rangle} \quad (2)$$

Fitzmaurice¹ has shown, that the irradiance-correlation coefficient may be related to log-amplitude statistics

$$\gamma(\rho) = \frac{\exp [4C_I(\rho)] - 1}{\exp [4C_I(0)] - 1} \quad (3)$$

$$\text{where } C_I(\rho) = \langle (I_1 - \bar{I}_1) (I_2 - \bar{I}_2) \rangle \quad (4)$$

If we define the log-amplitude correlation coefficient as $F(\rho)$,

$$\begin{aligned} \text{then } F(\rho) &= \frac{C_I(\rho)}{C_I(0)} \\ \gamma(\rho) &= \frac{\exp [4C_I(0) F(\rho)] - 1}{\exp [4C_I(0)] - 1} \end{aligned} \quad (6)$$

For weak turbulence,

$$\gamma(\rho) \approx F(\rho) \quad (7)$$

From Fried²,

$$C_I^s(\rho) = \frac{8.16k^2 C_N^2 T(\frac{5}{6})}{4\pi^{5/6}} \operatorname{Re} \left(\int_0^z \left(\frac{s\rho}{z} \right)^{5/3} / [2^{8/3} \Gamma(11/6)] \right)$$

$$-\frac{1}{2} \left[\frac{s(z-s)}{kz} \right]^{5/6} \times {}_1F_1 \left[-\frac{5}{6}; 1; \frac{ik\rho_s^2}{4(z-s)z} \right] ds \quad (8)$$

For a propagation path over which $C_N^2 = 0$ for all s except for a thin layer of turbulence of thickness $\Delta s \ll s$ this may be replaced by

$$C_1^s(\rho) = \frac{8 \cdot 16k^2 C_N^2 \Gamma(-5/6) \Delta s}{4^n} \operatorname{Re} \left[\frac{(\frac{s\rho}{z})^{5/3}}{2^{5/3} \Gamma(11/6)} - \frac{1}{2} \left\{ \frac{s(z-s)}{kz} \right\}^{5/6} \right. \\ \left. \times {}_1F_1 \left[-\frac{5}{6}; 1; \frac{ik\rho^2 s}{4(z-s)z} \right] \right] \quad (9)$$

Furthermore the turbulence need not be constant and therefore $C_N^2 \Delta s$ may be replaced by

$$\int_{\Delta s} C_N^2(s) ds \quad (10)$$

The log-amplitude correlation coefficient becomes

$$F(\rho) = \frac{\left[\left(\frac{s\rho}{z} \right)^{5/3} / [2^{5/3} \Gamma(11/6)] \right] - \frac{1}{2} \left[\frac{s(z-s)}{kz} \right]^{5/6}}{\operatorname{Re} \left\{ \frac{5/6}{1} {}_1F_1 \left[-\frac{5}{6}; 1; \frac{ik\rho^2 s}{4(z-s)z} \right] \right\}} \\ - \frac{1}{2} \left[\frac{s(z-s)}{kz} \right]^{5/6} \operatorname{Re} \left(\rho^{5/6} \right) \\ = 3.86 \operatorname{Re} \left\{ \right\} - \frac{\left(\frac{s\rho}{z} \right)^{5/3}}{\operatorname{Re}(\rho^{5/6}) 2^{5/3} \Gamma(11/6)} \left[\frac{kz}{s(z-s)} \right]^{5/6} \quad (11)$$

which reduces to

$$F(\rho) = 3.86 \operatorname{Re} \left\{ \right\} - 4.09 \left[\frac{k\rho^2}{4(z-s)z} \right]^{5/6} \quad (12)$$

The function ${}_1F_1 \left[-\frac{5}{6}; 1; \frac{ik\rho^2 s}{4(z-s)z} \right]$ is a confluent hypergeometric function with an imaginary argument.

Let

$$x = \frac{k \theta^2 s}{4(z-s)z} = \left[\frac{\rho}{\sqrt{\frac{4(z-s)z}{k s}}} \right]^2 = \left[\frac{\rho}{\sqrt{\lambda L}} \right]^2 \quad (13)$$

Then the hypergeometric function may be evaluated by a Kummer's³ function

$${}_1F_1(a; b; ix) = 1 + \frac{a}{b} (ix) + \frac{(a)_2 (ix)^2}{(b)_2 2!} + \dots + \frac{(a)_n (ix)^n}{(b)_n n!} \quad (14)$$

$$\text{where } (a)_n = a(a+1)(a+2)\dots(a+n-1) \quad (a)_0 = 1 \quad (15)$$

$$(b)_n = b(b+1)(b+2)\dots(b+n-1) \quad (b)_0 = 1 \quad (16)$$

If $a = -5/6$ and $b = 1$, then

$$\begin{aligned} {}_1F_1\left[-\frac{5}{6}; 1; ix\right] &= 1 - 5/6 (ix) + \frac{5}{144} x^2 + \frac{35}{7776} ix^3 \\ &\quad + \frac{91}{122,880} x^4 - \frac{1729}{186,624} ix^5 + \dots \\ &= 1 - 0.833 ix + 0.0347x^2 + 0.00450 ix^3 + 0.619x^4 \\ &\quad - 0.0000772x^5 + \dots \end{aligned} \quad (17)$$

We may normalize equation 12 by replacing ρ by $\rho/\sqrt{\lambda L}$, obtaining

$$F\left(\frac{\rho}{\sqrt{\lambda L}}\right) = 3.86 \operatorname{Re}\left\{\right\} - 4.09 [x]^{5/6} \quad (18)$$

Using this equation, we evaluate $\rho / \sqrt{\lambda L}$, $\text{Re} \left\{ \right\}$,
and $F\left(\frac{\rho}{\sqrt{\lambda L}}\right)$ as a function of x in the following:*

x	$\frac{\rho}{\sqrt{\lambda L}}$	$\text{Re} \left\{ i^{5/6} {}_1F_1 \left[-\frac{5}{6}; 1; ix \right] \right\}$	$F\left(\frac{\rho}{\sqrt{\lambda L}}\right)$
0	0	0.259	1.000
1/4	0.500	0.431	0.486
1/2	0.707	0.663	0.256
1	1.000	1.068	0.020
2	1.414	1.970	-0.094

The log-amplitude correlation coefficient is shown as a function of the normalized parameter $\rho / \sqrt{\lambda L}$ in Figure 6-9. The normalizing factor is known as the correlation length and corresponds to the separation for which $x = 1$.

Using the relationship of equation 6 between $\gamma\left(\rho / \sqrt{\lambda L}\right)$ and $F\left(\rho / \sqrt{\lambda L}\right)$, we can calculate the theoretical dependence of irradiance-correlation coefficient:

$F\left(\frac{\rho}{\sqrt{\lambda L}}\right)$	$\sigma_1^2=0$	$\sigma_1^2=0.20$	$\sigma_1^2=0.40$
0	0	0	0
0.2	0.2	0.13	0.1
0.4	0.4	0.31	0.22
0.6	0.6	0.50	0.39
0.8	0.8	0.73	0.65
1.0	1.00	1.00	1.00

In order to evaluate the actual correlation coefficient, we must analyze the turbulence as though it is made up of thin layers of turbulence of varying strengths and at varying distances from the source.

Because the thermosonde measurement showed only one layer of turbulence and from other measurements we know that turbulence exists at the tropopause, we will use a two-layer model of the atmosphere, although the results of the analysis will make apparent how more complicated models can be handled.

*See more complete table in Appendix B

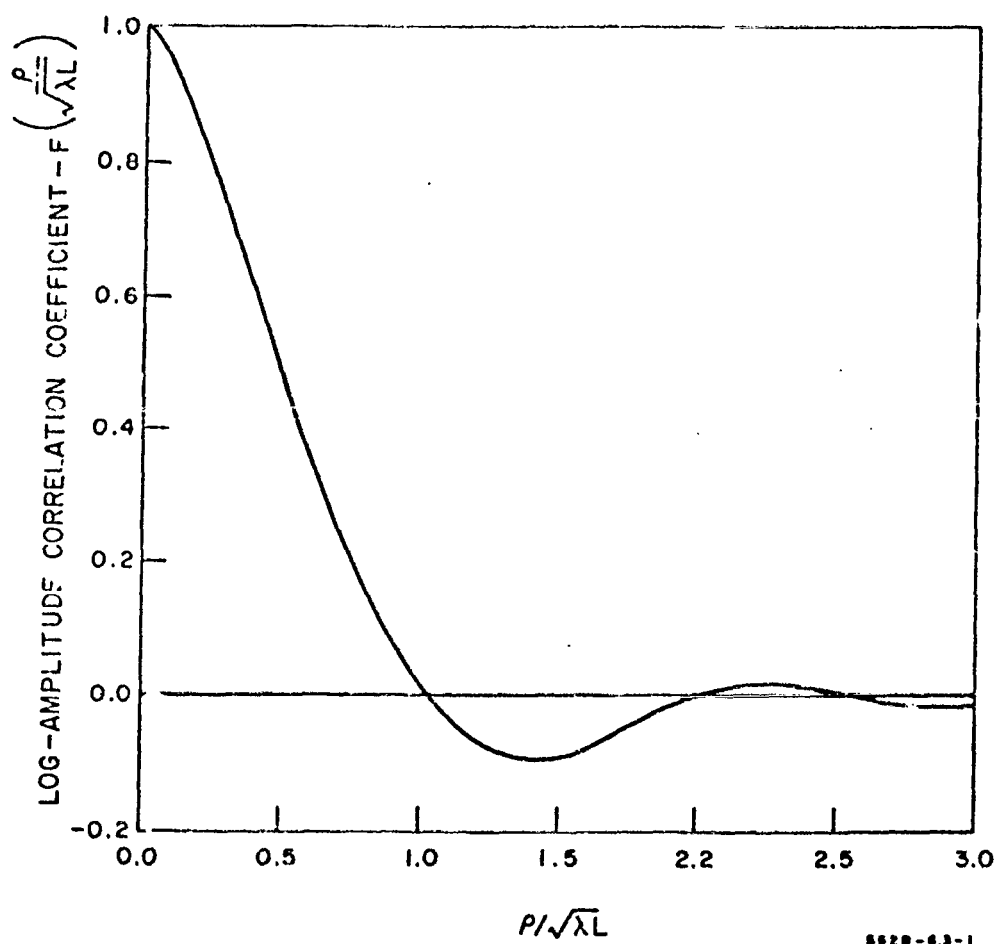


Figure 6-9. Log-Amplitude Correlation Coefficient

For a single layer of turbulence,

$$C_1^s(\rho) = \frac{8.16 k^2 \Gamma(-5/6)}{4\pi} C_N^2 \Delta s \operatorname{Re} \left[\frac{\left(\frac{s\rho}{z} \right)^{5/3}}{2^{8/3} \Gamma(11/6)} - \frac{1}{2} \left\{ \frac{s z}{k z} \right\}^{5/6} \right] \\ \times {}_1F_1 \left[-\frac{5}{6}; 1; \frac{ik\rho^2 s}{4(z-s)z} \right] \quad (19)$$

(for $s \ll z$)

Let

$$A = \frac{8.16 k^2 \Gamma(-5/6)}{4\pi} \quad B = \frac{(s/z)^{5/3}}{2^{8/3} \Gamma(11/6)}$$

$$C = \frac{1}{2} \left\{ \frac{1}{k} \right\}^{5/6} \quad D = \operatorname{Re} \left\{ {}_1F_1 \left[\begin{matrix} - \\ 1 \end{matrix} \right] \right\}$$

Then $C_N^* = C_N^2 \Delta s$

$$C_1^s(\rho) = A C_N^* \left[B s^{5/3} - C D s^{5/6} \right]$$

Also $C_1^s(\rho) = -A C_N^* C D s^{5/6} \quad D = 0.26$ (20)

$$= -0.26 A C_N^* C s^{5/6} \quad C_N^* = C_N^2 \Delta s s^{5/6} = C_N^2 \Delta s s^{5/6}$$

$$= -0.26 A C_N^* C$$

For a two layer turbulence model,

$$C_1^s(\rho) = A C_{N1}^* \left[B s_1^{5/3} - C D_1 s_1^{5/6} \right] + A C_{N2}^* \left[B s_2^{5/3} - C D_2 s_2^{5/6} \right] \quad (21)$$

If

$$s_1 \ll s_2 \quad D_1 = 0.26$$

Therefore

$$C_1^s(\rho) = A C_{N1}^* \left[B s_1^{5/3} - 0.26 C s_1^{5/6} \right] + A C_{N2}^* \left[B s_2^{5/3} - C D_2 s_2^{5/6} \right] \quad (22) \\ = A C_{N1}^* \left[B s_1^{5/6} - 0.26 C \right] + A C_{N2}^* \left[B s_2^{5/6} - C D_2 \right]$$

Defining $F(\rho) = C_1^s(\rho)/C_1^s(0)$, we have for the single layer model

$$F(\rho)_1 = \frac{AC_N^+ [Bs_1^{5/6} - C]}{-0.26 AC_N^+ C} = \frac{CD_1 - Bs_1^{5/6}}{0.26 C}$$

For the two layer model,

$$\begin{aligned} F(\rho)_{1+2} &= \frac{AC_{N1}^+ [Bs_1^{5/6} - 0.26C] + AC_{N2}^+ [Bs_2^{5/6} - CD_2]}{-0.26 AC [C_{N1}^+ + C_{N2}^+]} \\ &= \frac{C_{N1}^+ [Bs_1^{5/6} - CD_1] + C_{N2}^+ [Bs_2^{5/6} - CD_2]}{-0.26 C [C_{N1}^+ + C_{N2}^+]} \quad (23) \end{aligned}$$

If $C_{N1}^+ \gg C_{N2}^+$

$$\begin{aligned} F(\rho)_{1+2} &= \frac{C_{N1}^+ [CD_1 - Bs_1^{5/6}] + C_{N2}^+ [CD_2 - Bs_2^{5/6}]}{+0.26 C C_{N1}^+} \\ &= \frac{[CD_1 - Bs_1^{5/6}]}{0.26 C} + \frac{C_{N2}^+}{C_{N1}^+} \cdot \frac{[CD_2 - Bs_2^{5/6}]}{0.26 C} \\ &= F(\rho)_1 + \frac{C_{N2}^+}{C_{N1}^+} F(\rho)_2 \quad (24) \end{aligned}$$

If $C_{N1}^+ \approx C_{N2}^+$

$$F(\rho)_{1+2} = \left[\frac{C_{N1}^+}{C_{N1}^+ + C_{N2}^+} \right] F(\rho)_1 + \left[\frac{C_{N2}^+}{C_{N1}^+ + C_{N2}^+} \right] F(\rho)_2 \quad (25)$$

and for weak scintillation

$$\gamma_{1+2} = \left[\frac{C_{N1}^+}{C_{N1}^+ + C_{N2}^+} \right] \gamma_1 + \left[\frac{C_{N2}^+}{C_{N1}^+ + C_{N2}^+} \right] \gamma_2 \quad (26)$$

From this result, the method of analysis for multilayer models is apparent.

$$F(\rho) = \sum_{n=1}^k \left[\frac{C_{N1}^+}{C_{NT}^+} \right] F(\rho_1) + \left[\frac{C_{N2}^+}{C_{NT}^+} \right] F(\rho_2) + \dots + \left[\frac{C_{Nk}^+}{C_{NT}^+} \right] F(\rho_k) \quad (27)$$

where C_{NT}^+ is the integrated value of C_N^+ from 0 to ∞

From Figure 6-10, the correlation length for a particular altitude can be obtained.

Using this length, γ_1 and γ_2 can be calculated and, using the measured values of C_{N1}^+ and C_{N2}^+ from the experiment, a theoretical shape for $F(\rho)$ may be obtained.

This has been done graphically in Figure 6-11 using the correlation coefficient curve of Figure 6-9 and the following paragraphs

	<u>h(m)</u>	<u>Argon</u> $\sqrt{\lambda L}$	<u>CO₂</u>	<u>C_N⁺/C_{NT}⁺</u>
Boundary Layer	700	0.70	3.18	0.40
Tropopause	13,200	0.12	0.55	0.60

The experimental values of correlation coefficient are plotted in Figure 6-12 and recorded in Table 6-2. Using the results of Figure 6-12 and converting $F(\rho)$ to γ through Table 6-2, the theoretical log-irradiance correlation coefficient for various values of log-amplitude variance are shown for comparison.

The experimental and theoretical fit show excellent agreement indicating that the theory appears to give an accurate prediction of correlation coefficient.

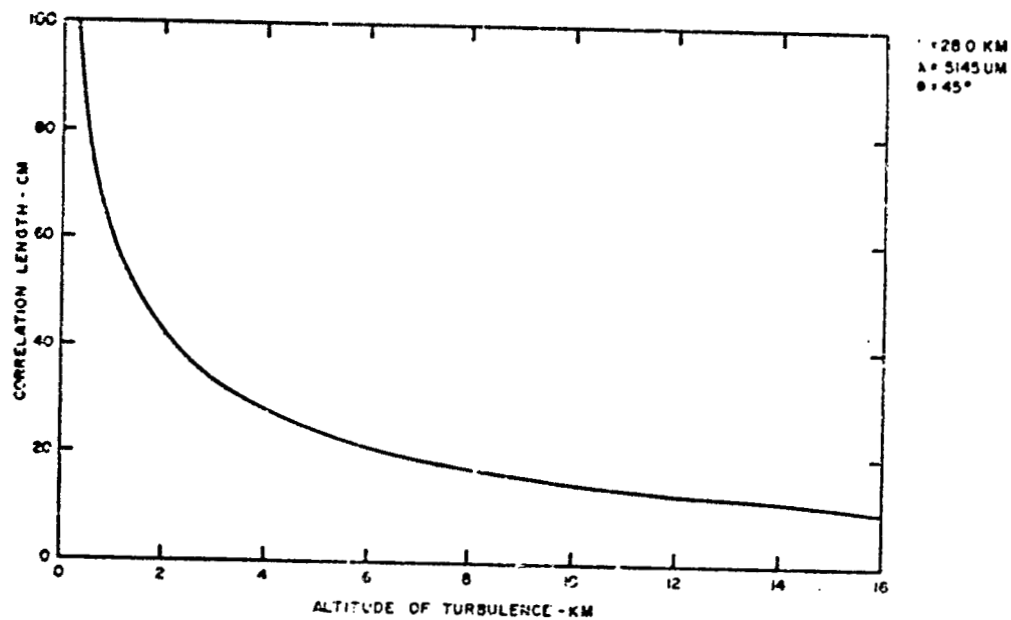
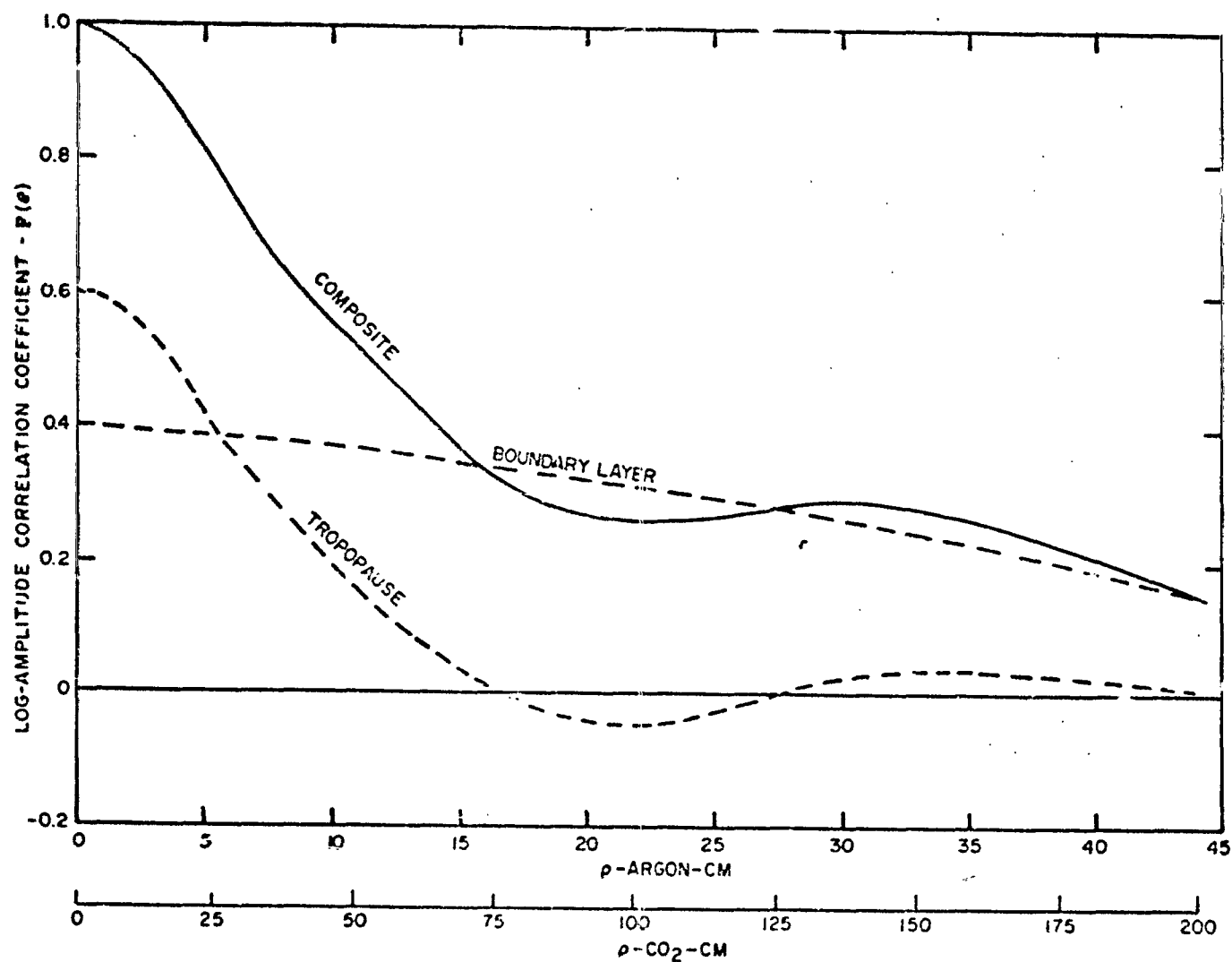


Figure 6-10. Correlation Length for Specific Altitude

Figure 6-11. Theoretical Shape of $F(\rho)$

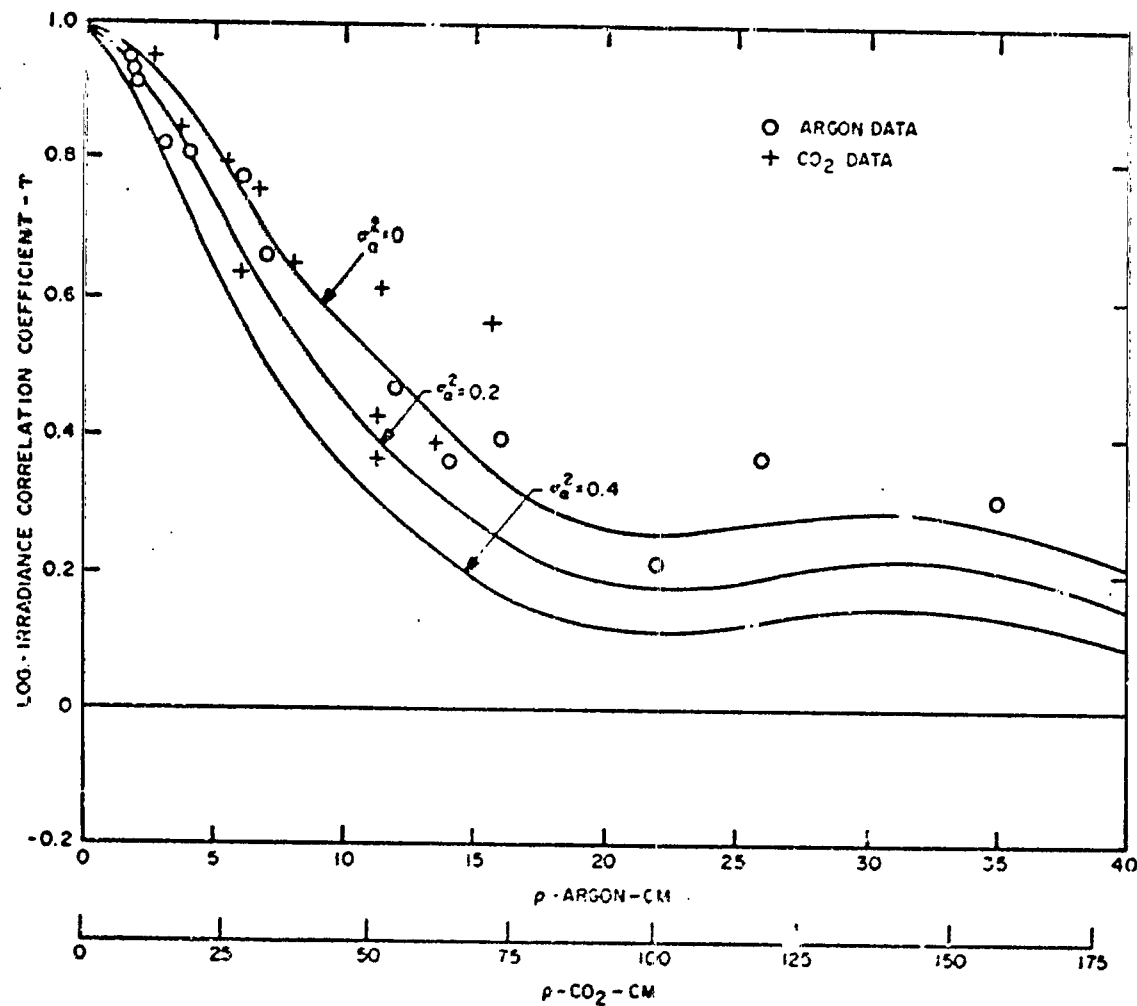


Figure 6-12. Experimental Values of Correlation Coefficient

Table 6-2
Table of Experimental Irradiance Correlation Coefficients

Argon Data				Carbon-Dioxide Data			
Time (GMT)		ρ (CM)	γ	Time (GMT)		ρ (CM)	γ
1.	13 29 16	2	0.949	1.	13 32 40	5	0.915
2.	13 27 00	2	0.939	2.	13 20 10	6	0.989
3.	13 25 45	2	0.921	3.	13 38 00	7	0.896
4.	13 23 00	3	0.811	4.	13 17 10	8	0.943
5.	13 20 10	4	0.803	5.	13 08 30	14	0.338
6.	13 17 10	6	0.772	6.	13 46 15	18	0.829
7.	13 14 50	8	0.665	7.	13 48 45	28	0.789
8.	13 12 55	12	0.477	8.	13 09 30	28	0.639
9.	13 12 15	14	0.352	9.	11 50 00	32	0.758
10.	13 08 30	16	0.400	10.	11 49 05	37	0.644
11.	13 47 30	22	0.212	11.	11 51 32	52	0.631
12.	13 09 30	26	0.367	12.	11 58 50	52	0.416
13.	12 06 07	35	0.307	13.	13 53 20	52	0.379
				14.	13 55 00	62	0.397
				15.	13 57 20	72	0.563

REFERENCES

1. Fitzmaurice, M.W., Experimental Investigations of Optical Propagation in Atmospheric Turbulence, NASA TR R-370 (Aug 1971).
2. Fried, D.L. J. Optical Soc. Am., Vol. 57 (1967), p. 191.
3. Abramowitz, M., and Stegun, I., Handbook of Mathematical Functions, Dover, New York (1964), p. 504.

6.4 APERTURE AVERAGING OF SCINTILLATION

Scintillation is a problem mainly to laser communications systems working in the visible or near infrared. Far-infrared wavelengths, because of the $7/6$ power of wave-number dependence, are only slightly affected. There are only two methods to avoid scintillation. The first, selection of a site which has low turbulence, is partially effective, but since nearly half of the scintillation is due to tropopause which is too high to be affected by terrain changes, only small reductions can be made through site selection. Hulet¹ notes that astronomers, at many different locations around the world, observe nearly identical levels of scintillation.

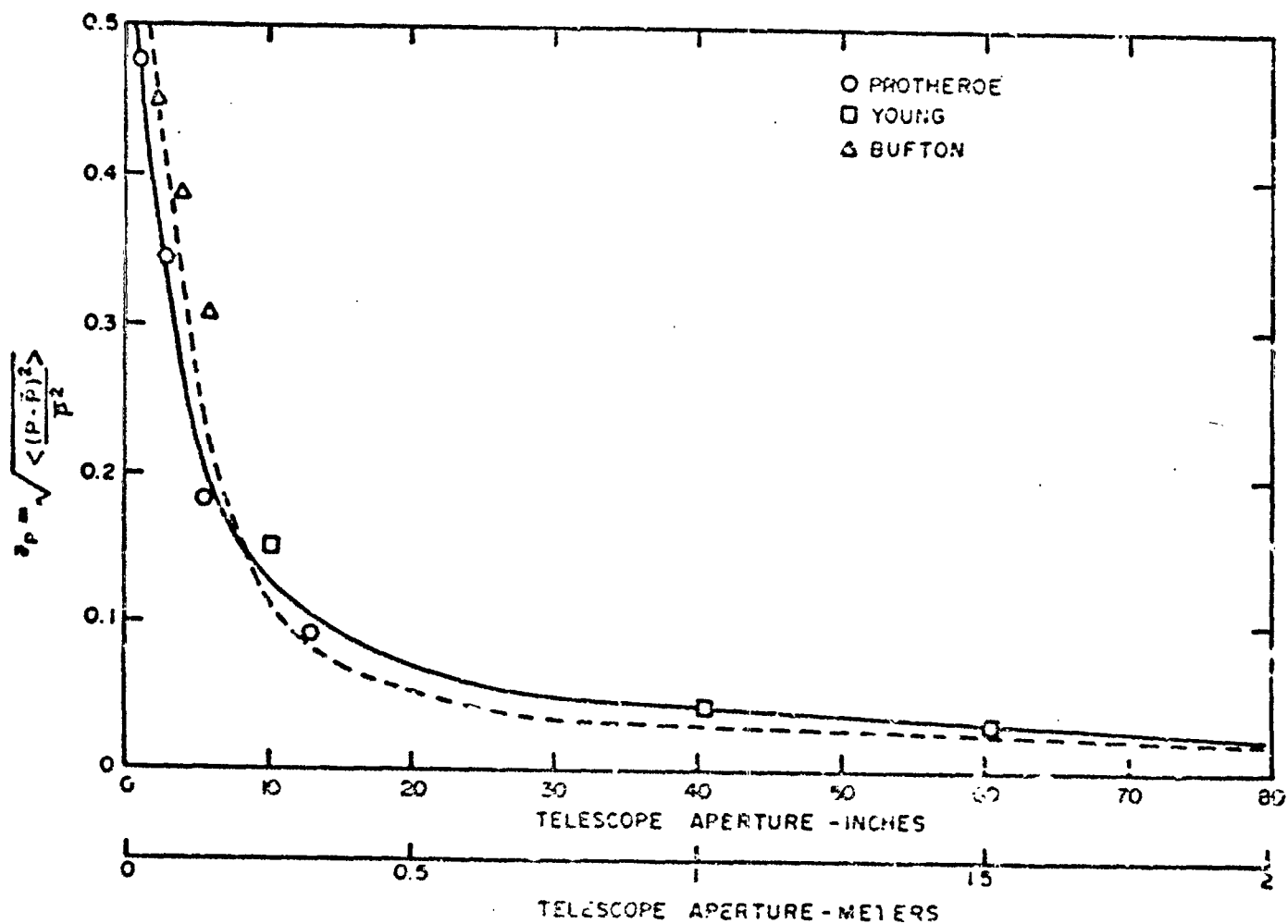
The second method of reducing scintillation is through the use of large apertures to average out the intensity of the fluctuations. Since the intensity in the receiving plane, as has been shown in section 6.3, is not well correlated over separations larger than a few tens of cm, the aperture of a large receiver will be divided into many small cells which scintillate independently from adjacent cells. Because of this behavior, the scintillation as measured by

$$\sigma_p = \frac{\sqrt{\langle (P - \bar{P})^2 \rangle}}{\bar{P}} \quad (1)$$

for apertures containing many independent cells should be proportional to $1/\sqrt{n}$ where n is the number of independent areas. Also, if on the average all of these areas are the same size, the \sqrt{n} is proportional to the diameter of the receiver (D) so that for large apertures σ_p is proportional to $1/D$.

Figure 6-13 shows the aperture dependence of the average value of $\bar{\sigma}_p$ as measured by Bufton², Protheroe³, and Young⁴. For very small apertures at wavelengths in the blue and green portion of the visible spectrum ($\lambda \approx 0.500 \pm 0.100 \mu\text{m}$) the magnitude of $\bar{\sigma}_p$ is approximately 0.55. As the aperture is increased, $\bar{\sigma}_p$ decreases rapidly until an aperture of about 25 cm (10 inches) is reached. Beyond 25 cm, the rate of decrease in scintillation is much slower, and approaches the theoretical $1/D$ dependence for large apertures. For $D \approx 50$ cm (20 inches)

$$\bar{\sigma}_p \approx \frac{0.045}{D} \quad (2)$$



1062-64-1

Figure 6-13. Aperture Dependence of $\bar{\sigma}_p$

REFERENCES

1. Hulett, H.R., J. Optical Soc. Am., Vol. 57 (1967), p.1335.
2. Bufton, J.L., An Investigation of Atmospheric Turbulence by Stellar Observations, NASA TR R-369 (Aug 1971).
3. Proetheroe, W.M., Preliminary Report on Stellar Scintillation, Contrib. Perkins Observ. Ser. 2, No. 447 (1955).
4. Young, J., Astronomical Journal (Aug 1967), P. 747.

6.5 AUTOCORRELATION OF IRRADIANCE AND POWER SPECTRAL DENSITY*

The autocorrelation of irradiance is defined as

$$R_I(\tau) = \langle [I(t) - \bar{I}] [I(t + \tau) - \bar{I}] \rangle = C_I(\tau) \quad (1)$$

where $I(t)$ is the irradiance at time t , $I(t + \tau)$ is the irradiance at the same point at time $t + \tau$, and \bar{I} is the average irradiance. This is usually normalized by dividing by the variance of irradiance to obtain the irradiance-correlation coefficient

$$\gamma(\tau) = \frac{C_I(\tau)}{C_I(0)} = \frac{\langle [I(t) - \bar{I}] [I(t + \tau) - \bar{I}] \rangle}{\langle (I - \bar{I})^2 \rangle} \quad (2)$$

where the coefficient is now a function of time delay τ rather than of spatial displacement (ρ) as in equation 2 of section 6.3. For a single layer of turbulence at distance s from the source, a displacement ρ' corresponds to a displacement

$$\rho' = \rho' \left[\frac{z}{s} \right] \quad (3)$$

in the detector plane at z from the projection shown in Figure 6-14. If ρ is replaced by the correlation length $\sqrt{\lambda L}$ in the detector plane,

$$\rho' = \sqrt{\lambda L} \left[\frac{s}{z} \right] \quad (4)$$

The time necessary for a turbulon to traverse this distance is

$$\tau_0 = \frac{\sqrt{\lambda L}}{v_n} \left[\frac{s}{z} \right] \quad (5)$$

where v_n is the wind velocity normal to the propagation path.

Therefore if Taylor's hypothesis¹ of frozen-in turbulence is assumed, τ_0 is the time required for a turbulon in the plane of turbulence at s to traverse the correlation length ($\sqrt{\lambda L}$) in the receiver plane, and is therefore simply the correlation time. Taylor's hypothesis is valid whenever $\sqrt{\lambda L} \ll L_0$, that is when the correlation length is less than the outer scale of turbulence. From Fried², the outer scale of turbulence

*Data processed only for the argon wavelength.

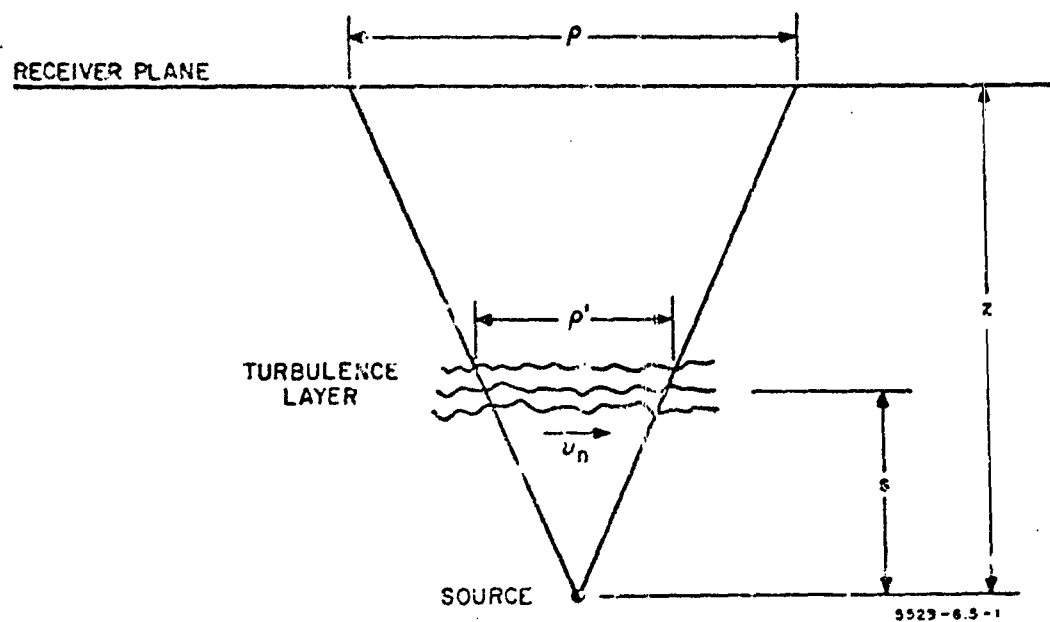


Figure 6-14

at 700 m altitude (lowest layer of turbulence) is 40 m which is much larger than the correlation length for that altitude (0.70 m) and therefore the requirements of Taylor's hypothesis are met for all the turbulence layers since correlation length decreases with altitude while outer scale increases.

The wind speed corresponding to the tropopause (14.4 km) is 24.7 ms^{-1} and the correlation length corresponding to this height is 0.087 meters. Therefore from equation 5, the correlation time is

$$\tau_o = \frac{0.087}{24.7} \left[\frac{14.4 \times 10^3}{23.4 \times 10^3} \right] = 2.17 \times 10^{-3} \text{ sec}$$

For the low altitude barrier layer turbulence, we get the altitude of the turbulence directly from thermosonde measurements and find it to be approximately 700 meters, with a wind speed of 10.1 ms^{-1} (19.6 knots). The correlation length for this altitude is approximately 0.70 meters, therefore

$$\tau_o = \frac{0.70}{10.1} \left[\frac{0.70 \times 10^3}{23.4 \times 10^3} \right] = 2.08 \times 10^{-3} \text{ sec}$$

In making this computation the velocity of the wind has been used without correction for its azimuth since by fortuitous circumstance the wind vector for both layers of turbulence was precisely at right angles to the propagation path at the time of the measurement (1313 GMT). Had the wind been at another azimuth (ϕ_w) the normal component of the wind velocity could have been computed by the following relationship from Young⁴

$$v_n = \frac{v}{\sec \Theta_T} \left[1 + \tan^2 \Theta_T \sin^2 (\phi_T - \phi_w) \right]^{1/2}$$

where Θ_T is the zenith angle of the target and ϕ_T is the azimuth angle. Since the barrier layer turbulence and tropopause turbulence were of approximately the same strength, we would expect the correlation time to be approximately

$$\tau_o = \frac{(2.08 + 2.17) \times 10^{-3}}{2} = 2.13 \times 10^{-3} \text{ sec.}$$

The actual correlation time from measurement (Figure 6-15) was 2.40×10^{-3} seconds. The difference between predicted and measured correlation time is therefore

$$\frac{\tau_{OE} - \tau_{OP}}{\tau_{OE}} = \frac{(2.40 - 2.13) \times 10^{-3}}{2.40 \times 10^{-3}} = 11.2\%$$

which is well within the accuracy of the wind speed measurement.

The normalized power spectral density of irradiances calculated from the auto-correlation of irradiance data by Fourier transform methods is shown in Figure 6-16. Since the power spectral density of irradiance is proportional to wavenumber ($k = \frac{2\pi}{\lambda}$), by scaling the frequency axis, the same curve may be used for other wavelengths. Carbon dioxide scintillation for example would have frequencies

$$\sqrt{\frac{0.5145 \cdot 10^{-6}}{10.6 \times 10^{-6}}} = 0.22$$

times as great as the argon wavelength. The correlation curve can also be used for carbon dioxide by multiplying the time axis by $1/0.22$.

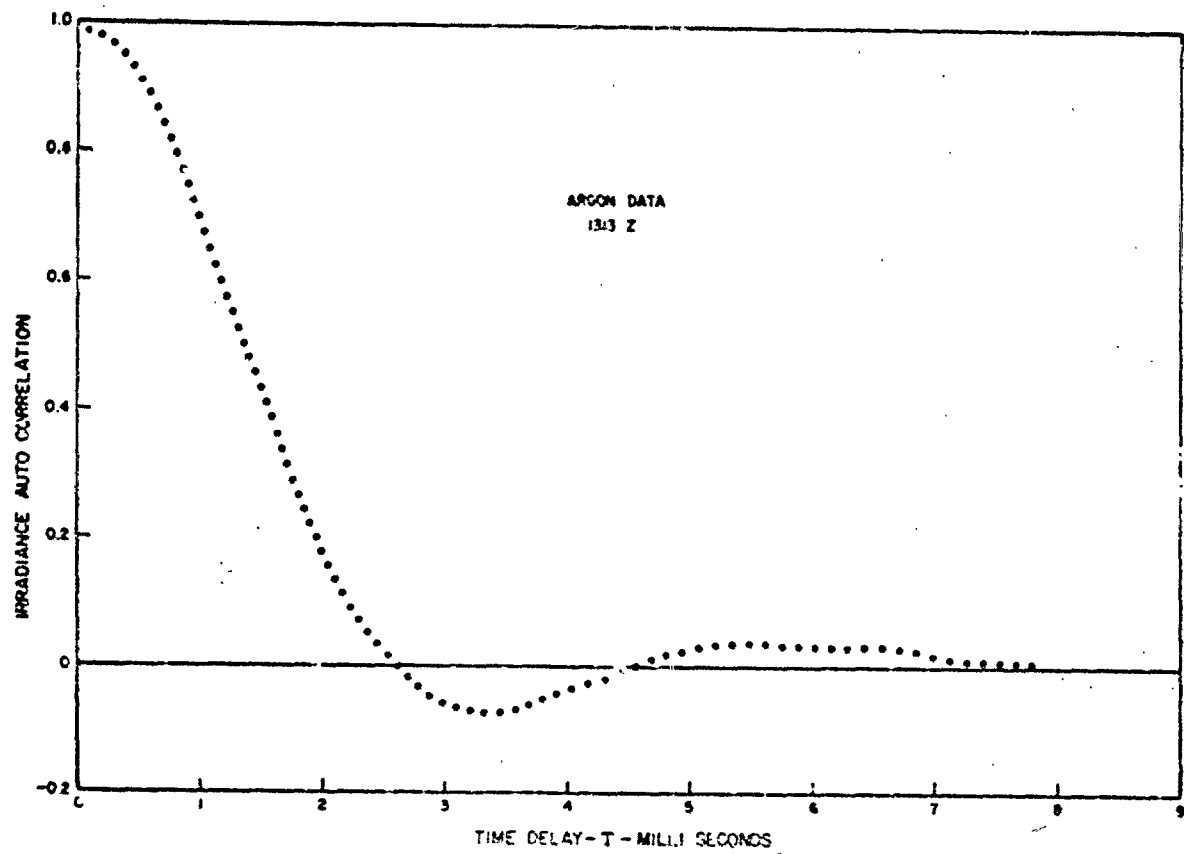


Figure 6-15

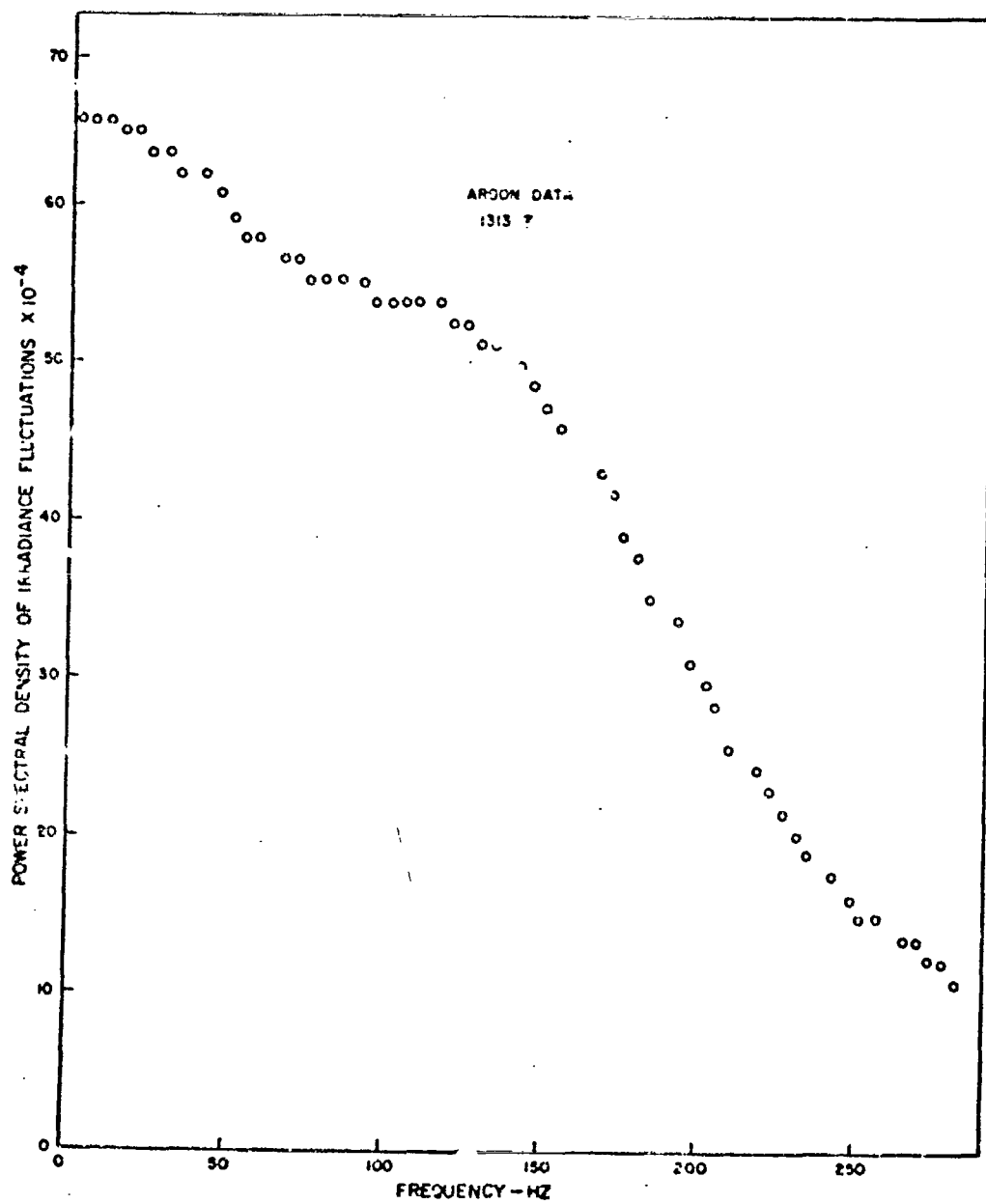


Figure 6-16

Table 6-3
Log-Irradiance Autocorrelation

τ	γ	τ	γ	τ	γ
0	1.00	2.0	0.17	4.0	-0.04
0.1	0.99	2.1	0.14	4.2	-0.03
0.2	0.98	2.2	0.10	4.4	-0.02
0.3	0.97	2.3	0.07	4.6	0
0.4	0.94	2.4	0.04	4.8	0.02
0.5	0.91	2.5	0.02	5.0	0.02
0.6	0.89	2.6	0	5.2	0.03
0.7	0.83	2.7	-0.02	5.4	0.03
0.8	0.80	2.8	-0.03	5.6	0.03
0.9	0.75	2.9	-0.05	5.8	0.03
1.0	0.69	3.0	-0.06	6.0	0.03
1.1	0.65	3.1	-0.07	6.2	0.03
1.2	0.59	3.2	-0.07	6.4	0.03
1.3	0.54	3.3	-0.07	6.6	0.03
1.4	0.48	3.4	-0.08	6.8	0.02
1.5	0.43	3.5	-0.07	7.0	0.01
1.6	0.38	3.6	-0.07	7.2	0.01
1.7	0.32	3.7	-0.06	7.4	0.01
1.8	0.28	3.8	-0.05	7.6	0.01
1.9	0.23	3.9	-0.05	7.8	0
Wavelength = 0.5145 μm		Time 13:12:55		τ in milliseconds	

REFERENCES

1. Lumley, J.L., and Panofsky, H.A., *The Structure of Atmospheric Turbulence*, Interscience, New York (1964), p. 74.
2. Fried, D.L., *Proc IEEE*, Vol. 55, No. 1 (Jan 1967), p. 57 (fig 5).

7. CONCLUSIONS

In the previous sections of this report we have described the experiment and analyzed its results. In this section we will attempt to synopsize what has been learned, and what can be concluded from the experiment results.

In section 6.1, Figure 6-4, the vertical profile of turbulence in the first 6 km of the atmosphere at the time of the experiment is presented, together with a mathematical model useful for approximating the turbulence distribution. We find that the scale height of the atmosphere is lower than predicted by Fried¹ by a factor of about three to one.

In section 6.2, the log-amplitude variance is analyzed, and it is shown that the strength of scintillation can only be accounted for by strong turbulence above 6 km. On the basis of the wind profile, temperature profile and correlation length, the layer is predicted to be at the tropopause. The distribution of log-amplitude variances is shown to be log-normal with a standard deviation of 0.6. The wavelength dependence ($k^{-7/6}$) of scintillation is confirmed for the two wavelengths used in the test. The irradiance distribution is checked and found to be log-normal. The log-amplitude variance calculated in the basis of the profile of turbulence of section 6.1 is compared and found to be in agreement with the experimental values.

In section 6.3, the log-amplitude correlation coefficient is calculated on the basis of the turbulence model of section 6.1 and shown to be in agreement with the experimentally measured values. The correlation length is found to be proportional to $\sqrt{\lambda}$, and a method of determining the correlation length for multilayer turbulence models is derived.

Based upon the results above, the reduction of scintillation using a large telescope is calculated in section 6.4 and compared to measurements by standard astronomical techniques. The dependence of scintillation frequency on wind speed is tested in section 6.5 and compared with the measured data. Correlation time and power spectral densities are shown to be directly related to wind speeds in the various turbulent layers.

The analysis of the data obtained from the experiment tends to confirm the theoretical predictions of scintillation based upon the turbulence profile. We believe that this is the first experiment in which the optical effects of turbulence upon laser beams

propagating over a vertical path have been tested in a controlled manner. We have found no case in which the data contradicts the theoretical predictions, and have obtained reasonably good confirmations of many of the aspects of the theory. The experiment also has allowed us to develop a technique of measuring the vertical profile through a balloon launched thermosonde device.

Our experiment has essentially tested Schmeltzer's Equation 7.8 for log-amplitude covariance. Because the assumptions made for the log-amplitude covariance equations are largely the same as those for phase covariance (Equation 7.9) the results of the experiment tend to lend credence to the theory for phase statistics as well as for amplitude statistics. The reader should review Schmeltzer's paper to see the remarkable similarity of Equations 7.8 and 7.9, and the fact that they are both based upon the same basic derivation.

Some of the more important results of the experiment are shown in the following table.

Table 7-1
Synopsis of Some of the Major Results of the HAPE I Experiment

1. Vertical Profile of Turbulence (Figure 6-4)	$C_N^2 = C_{N0}^2 h^{-1/3} e^{-h/h_0} + 8(h - h_p) C_{Np}^2$ $C_{N0}^2 = 4 \times 10^{-14} \text{ m}^{-2/3} \quad h_0 \approx 1000 \text{ m}$ $C_{Np}^2 = 4.3 \times 10^{-13} \text{ m}^{-1/3} \quad h_p \approx 13.2 \times 10^3 \text{ m}$
2. Strength of Scintillation	
a. Wavelength dependence (p. 6-14)	$\alpha \lambda^{-7/6}$
b. Distribution (Figures 6-8 and 6-9)	Log-normal
c. Log-Amplitude Variance (Mean)	
1) 0.5145 μm (Figure 6-6)	0.17
2) 10.6 μm (Figure 6-7)	0.005
d. Distribution of Sample Variances	
1) Type (Figures 6-9 and 6-7)	Log-normal
2) Standard Deviation (p. 6-14)	0.6

Table 7-1
Synopsis of Some of the Major Results of the BAPE I Experiment (Cont)

3. Correlation of Intensity	
a. Wavelength Dependence of Correlation Length (Figure 6-13)	$\lambda^{1/2}$
b. Correlation Lengths	
1) 0.5145 μm (Figure 6-13)	22 cm
2) 10.6 μm (Figure 6-13)	100 cm
c. Height Dependence of Correlation Length (p. 6-26)	$\propto \left[\frac{(z - s) z}{s} \right]^{1/2}$
4. Aperture Averaging of Scintillation	
a. Wavelength Dependence (p. 6-36)	$\propto \lambda^{-1/2}$
b. Aperture Dependence (Large Apertures) (Figure 6-14)	$\propto D^{-1}$
c. Standard Deviation of Power (Large Apertures) (p. 6-36)	$\propto \sigma_p = \frac{0.045}{D}$
5. Correlation Time	
a. Wind Speed Dependence (p. 6-44)	$\propto v_n^{-1}$
b. Distance Dependence (p. 6-44)	$\propto s/z$
c. Wavelength Dependence (p. 6-44)	$\propto \lambda^{1/2}$

Let us now consider how the results of the experiment have aided laser communication theory. From the results, we can estimate the time dependence of power received at a ground receiver from a spacecraft, or the power received at a spacecraft from a ground receiver. We can do this for any wavelength, for any size receiver, for any zenith angle, and (using results from BAPE II) for any time of day. This information can be directly applied to the estimation of bit error rate. We can estimate the length of severe dropouts, their frequency, and the percent of time that a laser communications system will operate at its designed bit error rate or signal-to-noise ratio. Because of the multitude of factors affecting the system performance, it is very difficult to present the results in a single graph. Rather, the results must be used to compute system performance for each new system as it is developed. Our new knowledge of the

atmospheric effects of turbulence should enable us to design laser systems which will operate successfully through atmospheric turbulence.

One area which needs further investigation is the frequency and depth of severe intensity dropouts. These dropouts have little effect upon the means and variances but severely effect the bit error rate of pulsed binary laser communications systems. Because of the very high signal-to-noise ratio and dynamic range required to perform this type of measurement, it was beyond the scope of this experiment.

A continuation of the BAPE I flight of 1970 was performed in the fall of 1971. This experiment, BAPE II, has added to the data of this report (particularly in the area of turbulence profiles) and a report on its results is under preparation.

The BAPE system is the only existing equipment capable of measuring the statistics of the optical effects of turbulence upon laser beams propagating from earth to space. While the BAPE I and II flights have provided a great deal of information, many interesting and important experiments remain to be done. The most important of these are the direct measurement of the phase statistics of optical propagation, and the measurement of the frequency of severe amplitude dropouts. Work in these areas should be the next problems of laser propagation to be investigated.

APPENDIX A
UPPER AIR DATA

STATION ALTITUDE 4500.00 FEET MSL
21 OCT. 78 CIG 400 MFT
ASCENTION NO. 136

SIGNIFICANT LEVEL DATA 2000010734 MOLLEMAN

WSTM SITE COORDINATES
575700.00 FEET E
352000.00 FEET N

PRESSURE MILLIBARS	GEOMETRIC ALTITUDE MFT FEET	TEMPERATURE AIR DEGREES CENTIGRADE	REL. HUM. PERCENT
837.5	4500.0	11.9	2.0
837.5	4475.0	10.3	1.2
837.5	4450.0	10.0	2.0
837.5	4425.0	9.4	0.1
837.5	4400.0	8.1	0.0
837.5	4375.0	9.0	1.1
837.5	4350.0	8.0	10.0
837.5	4325.0	7.8	10.0
837.5	4300.0	7.8	10.0
837.5	4275.0	7.8	10.0
837.5	4250.0	7.0	10.0
837.5	4225.0	7.0	10.0
837.5	4200.0	7.0	10.0
837.5	4175.0	7.0	10.0
837.5	4150.0	7.0	10.0
837.5	4125.0	7.0	10.0
837.5	4100.0	7.0	10.0
837.5	4075.0	7.0	10.0
837.5	4050.0	7.0	10.0
837.5	4025.0	7.0	10.0
837.5	4000.0	7.0	10.0
837.5	3975.0	7.0	10.0
837.5	3950.0	7.0	10.0
837.5	3925.0	7.0	10.0
837.5	3900.0	7.0	10.0
837.5	3875.0	7.0	10.0
837.5	3850.0	7.0	10.0
837.5	3825.0	7.0	10.0
837.5	3800.0	7.0	10.0
837.5	3775.0	7.0	10.0
837.5	3750.0	7.0	10.0
837.5	3725.0	7.0	10.0
837.5	3700.0	7.0	10.0
837.5	3675.0	7.0	10.0
837.5	3650.0	7.0	10.0
837.5	3625.0	7.0	10.0
837.5	3600.0	7.0	10.0
837.5	3575.0	7.0	10.0
837.5	3550.0	7.0	10.0
837.5	3525.0	7.0	10.0
837.5	3500.0	7.0	10.0
837.5	3475.0	7.0	10.0
837.5	3450.0	7.0	10.0
837.5	3425.0	7.0	10.0
837.5	3400.0	7.0	10.0
837.5	3375.0	7.0	10.0
837.5	3350.0	7.0	10.0
837.5	3325.0	7.0	10.0
837.5	3300.0	7.0	10.0
837.5	3275.0	7.0	10.0
837.5	3250.0	7.0	10.0
837.5	3225.0	7.0	10.0
837.5	3200.0	7.0	10.0
837.5	3175.0	7.0	10.0
837.5	3150.0	7.0	10.0
837.5	3125.0	7.0	10.0
837.5	3100.0	7.0	10.0
837.5	3075.0	7.0	10.0
837.5	3050.0	7.0	10.0
837.5	3025.0	7.0	10.0
837.5	3000.0	7.0	10.0
837.5	2975.0	7.0	10.0
837.5	2950.0	7.0	10.0
837.5	2925.0	7.0	10.0
837.5	2900.0	7.0	10.0
837.5	2875.0	7.0	10.0
837.5	2850.0	7.0	10.0
837.5	2825.0	7.0	10.0
837.5	2800.0	7.0	10.0
837.5	2775.0	7.0	10.0
837.5	2750.0	7.0	10.0
837.5	2725.0	7.0	10.0
837.5	2700.0	7.0	10.0
837.5	2675.0	7.0	10.0
837.5	2650.0	7.0	10.0
837.5	2625.0	7.0	10.0
837.5	2600.0	7.0	10.0
837.5	2575.0	7.0	10.0
837.5	2550.0	7.0	10.0
837.5	2525.0	7.0	10.0
837.5	2500.0	7.0	10.0
837.5	2475.0	7.0	10.0
837.5	2450.0	7.0	10.0
837.5	2425.0	7.0	10.0
837.5	2400.0	7.0	10.0
837.5	2375.0	7.0	10.0
837.5	2350.0	7.0	10.0
837.5	2325.0	7.0	10.0
837.5	2300.0	7.0	10.0
837.5	2275.0	7.0	10.0
837.5	2250.0	7.0	10.0
837.5	2225.0	7.0	10.0
837.5	2200.0	7.0	10.0
837.5	2175.0	7.0	10.0
837.5	2150.0	7.0	10.0
837.5	2125.0	7.0	10.0
837.5	2100.0	7.0	10.0
837.5	2075.0	7.0	10.0
837.5	2050.0	7.0	10.0
837.5	2025.0	7.0	10.0
837.5	2000.0	7.0	10.0
837.5	1975.0	7.0	10.0
837.5	1950.0	7.0	10.0
837.5	1925.0	7.0	10.0
837.5	1900.0	7.0	10.0
837.5	1875.0	7.0	10.0
837.5	1850.0	7.0	10.0
837.5	1825.0	7.0	10.0
837.5	1800.0	7.0	10.0
837.5	1775.0	7.0	10.0
837.5	1750.0	7.0	10.0
837.5	1725.0	7.0	10.0
837.5	1700.0	7.0	10.0
837.5	1675.0	7.0	10.0
837.5	1650.0	7.0	10.0
837.5	1625.0	7.0	10.0
837.5	1600.0	7.0	10.0
837.5	1575.0	7.0	10.0
837.5	1550.0	7.0	10.0
837.5	1525.0	7.0	10.0
837.5	1500.0	7.0	10.0
837.5	1475.0	7.0	10.0
837.5	1450.0	7.0	10.0
837.5	1425.0	7.0	10.0
837.5	1400.0	7.0	10.0
837.5	1375.0	7.0	10.0
837.5	1350.0	7.0	10.0
837.5	1325.0	7.0	10.0
837.5	1300.0	7.0	10.0
837.5	1275.0	7.0	10.0
837.5	1250.0	7.0	10.0
837.5	1225.0	7.0	10.0
837.5	1200.0	7.0	10.0
837.5	1175.0	7.0	10.0
837.5	1150.0	7.0	10.0
837.5	1125.0	7.0	10.0
837.5	1100.0	7.0	10.0
837.5	1075.0	7.0	10.0
837.5	1050.0	7.0	10.0
837.5	1025.0	7.0	10.0
837.5	1000.0	7.0	10.0
837.5	975.0	7.0	10.0
837.5	950.0	7.0	10.0
837.5	925.0	7.0	10.0
837.5	900.0	7.0	10.0
837.5	875.0	7.0	10.0
837.5	850.0	7.0	10.0
837.5	825.0	7.0	10.0
837.5	800.0	7.0	10.0
837.5	775.0	7.0	10.0
837.5	750.0	7.0	10.0
837.5	725.0	7.0	10.0
837.5	700.0	7.0	10.0
837.5	675.0	7.0	10.0
837.5	650.0	7.0	10.0
837.5	625.0	7.0	10.0
837.5	600.0	7.0	10.0
837.5	575.0	7.0	10.0
837.5	550.0	7.0	10.0
837.5	525.0	7.0	10.0
837.5	500.0	7.0	10.0
837.5	475.0	7.0	10.0
837.5	450.0	7.0	10.0
837.5	425.0	7.0	10.0
837.5	400.0	7.0	10.0
837.5	375.0	7.0	10.0
837.5	350.0	7.0	10.0
837.5	325.0	7.0	10.0
837.5	300.0	7.0	10.0
837.5	275.0	7.0	10.0
837.5	250.0	7.0	10.0
837.5	225.0	7.0	10.0
837.5	200.0	7.0	10.0
837.5	175.0	7.0	10.0
837.5	150.0	7.0	10.0
837.5	125.0	7.0	10.0
837.5	100.0	7.0	10.0
837.5	75.0	7.0	10.0
837.5	50.0	7.0	10.0
837.5	25.0	7.0	10.0
837.5	0.0	7.0	10.0

STATION ALTITUDE 4500.00 FEET MSL
21 OCT. 78 CIG 400 MFT
ASCENTION NO. 136

UPPER AIR DATA 2000010734 MOLLEMAN

WSTM SITE COORDINATES
575700.00 FEET E
352000.00 FEET N

GEOMETRIC ALTITUDE MFT FEET	PRESSURE MILLIBARS	TEMPERATURE AIR DEGREES CENTIGRADE	REL. HUM. PERCENT	DENSITY GRAMS PER CUBIC METER	SPEED OF WIND KNOTS	WIND DATA DIRECTION DEGREES (T)	WIND DATA SPEED KNOTS	INDEX OF REFRACTION
4500.0	837.5	11.9	2.0	1049.9	450.0	1.0	8.0	1.000279
4475.0	837.5	11.9	2.0	1059.9	460.0	1.0	8.7	1.000283
4450.0	837.5	11.9	2.0	1069.9	470.0	1.0	9.0	1.000287
4425.0	837.5	11.9	2.0	1079.9	480.0	1.0	9.0	1.000291
4400.0	837.5	11.9	2.0	1089.9	490.0	1.0	9.0	1.000295
4375.0	837.5	11.9	2.0	1099.9	500.0	1.0	9.0	1.000299
4350.0	837.5	11.9	2.0	1109.9	510.0	1.0	9.0	1.000303
4325.0	837.5	11.9	2.0	1119.9	520.0	1.0	9.0	1.000307
4300.0	837.5	11.9	2.0	1129.9	530.0	1.0	9.0	1.000311
4275.0	837.5	11.9	2.0	1139.9	540.0	1.0	9.0	1.000315
4250.0	837.5	11.9	2.0	1149.9	550.0	1.0	9.0	1.000319
4225.0	837.5	11.9	2.0	1159.9	560.0	1.0	9.0	1.000323
4200.0	837.5	11.9	2.0	1169.9	570.0	1.0	9.0	1.000327
4175.0	837.5	11.9	2.0	1179.9	580.0	1.0	9.0	1.000331
4150.0	837.5	11.9	2.0	1189.9	590.0	1.0	9.0	1.000335
4125.0	837.5	11.9	2.0	1199.9	600.0	1.0	9.0	1.000339
4100.0	837.5	11.9	2.0	1209.9	610.0	1.0	9.0	1.000343
4075.0	837.5	11.9	2.0	1219.9	620.0	1.0	9.0	1.000347
4050.0	837.5	11.9	2.0	1229.9	630.0	1.0	9.0	1.000351
4025.0	837.5	11.9	2.0	1239.9	640.0	1.0	9.0	1.000355
4000.0	837.5	11.9	2.0	1249.9	650.0	1.0	9.0	1.000359
3975.0	837.5	11.9	2.0	1259.9	660.0	1.0	9.0	1.000363
3950.0	837.5	11.9	2.0	1269.9	670.0	1.0	9.0	1.000367
3925.0	837.5	11.9	2.0	1279.9	680.0	1.0	9.0	1.000371
3900.0	837.5	11.9	2.0	1289.9	690.0	1.0	9.0	1.000375
3875.0	837.5	11.9	2.0	1299.9	700.0	1.0	9.0	1.000379
3850.0	837.5	11.9	2.0	1309.9	710.0	1.0	9.0	1.000383
3825.0	837.5	11.9	2.0	1319.9	720.0	1.0	9.0	1.000387
3800.0	837.5	11.9	2.0	1329.9	730.0	1.0	9.0	1.000391
3775.0	837.5	11.9	2.0	1339.9	740.0	1.0	9.0	1.000395
3750.0	837.5	11.9	2.0	1349.9	750.0	1.0	9.0	1.000399
3725.0	837.5	11.9	2.0	1359.9	760.0	1.0	9.0	1.000403
3700.0	837.5	11.9	2.0	1369.9	770.0	1.0	9.0	1.000407
3675.0	837.5	11.9	2.0	1379.9	780.0	1.0	9.0	1.000411
3650.0	837.5	11.9	2.0	1389.9	790.0	1.0	9.0	1.000415
3625.0	837.5	11.9	2.0	1399.9	800.0	1.0	9.0	1.000419
3600.0	837.5	11.9	2.0	1409.9	810.0	1.0	9.0	1.000423
3575.0	837.5	11.9	2.0	1419.9	820.0	1.0	9.0	1.000427
3550.0	837.5	11.9	2.0	1429.9	830.0	1.0	9.0	1.000431
3525.0	837.5	11.9	2.0	1439.9	840.0	1.0	9.0	1.000435
3500.0	837.5	11.9	2.0	1449.9	850.0	1.0	9.0	1.000439
3475.0	837.5	11.9	2.0	1459.9	860.0	1.0	9.0	1.000443

STATION ALTITUDE 4500.00 FEET MSL
21 OCT. 78 CTD NOS HST
ASCENSION NO. 174

UPPER AIR DATA
240010174
MOLLEMAN

WIND SITE COORDINATES
575700.00 FEET E
352000.00 FEET N

GEOMETRIC ALTITUDE MSL FEET	PRESSURE MILLIBARS	TEMPERATURE AIR DEWPOINT CENTIGRADE	REL. HUM. PERCENT	DENSITY GPM/CUBIC METER	SPEED UP SUMO KNOTS	WIND DATA DIRECTION DEGREES (T)	SPEED KNOTS	INDEX UP REFRACTION	
28770.0	911.1	-1.9	27.0	17.0	755.5	035.7	250.0	28.0	1.000107
28760.0	911.2	-1.9	27.0	17.0	756.2	035.5	250.5	28.0	1.000108
28750.0	911.4	-1.9	27.0	17.2	757.4	035.1	250.0	28.2	1.000109
28740.0	911.5	-1.9	27.0	17.0	758.0	034.6	250.0	28.1	1.000110
28730.0	911.7	-1.9	27.0	16.8	758.7	034.0	249.5	27.9	1.000111
28720.0	911.8	-1.9	27.0	16.5	759.4	033.0	248.5	27.0	1.000112
28710.0	911.9	-1.9	27.0	16.2	760.1	032.0	247.5	27.0	1.000113
28700.0	912.0	-1.9	27.0	15.9	760.7	031.0	246.5	27.0	1.000114
28690.0	912.1	-1.9	27.0	15.6	761.4	030.0	245.5	27.0	1.000115
28680.0	912.2	-1.9	27.0	15.3	762.1	029.0	244.5	27.0	1.000116
28670.0	912.3	-1.9	27.0	15.0	762.7	028.0	243.5	27.0	1.000117
28660.0	912.4	-1.9	27.0	14.7	763.4	027.0	242.5	27.0	1.000118
28650.0	912.5	-1.9	27.0	14.4	764.0	026.0	241.5	27.0	1.000119
28640.0	912.6	-1.9	27.0	14.1	764.7	025.0	240.5	27.0	1.000120
28630.0	912.7	-1.9	27.0	13.8	765.4	024.0	239.5	27.0	1.000121
28620.0	912.8	-1.9	27.0	13.5	766.1	023.0	238.5	27.0	1.000122
28610.0	912.9	-1.9	27.0	13.2	766.7	022.0	237.5	27.0	1.000123
28600.0	913.0	-1.9	27.0	12.9	767.4	021.0	236.5	27.0	1.000124
28590.0	913.1	-1.9	27.0	12.6	768.1	020.0	235.5	27.0	1.000125
28580.0	913.2	-1.9	27.0	12.3	768.7	019.0	234.5	27.0	1.000126
28570.0	913.3	-1.9	27.0	12.0	769.4	018.0	233.5	27.0	1.000127
28560.0	913.4	-1.9	27.0	11.7	770.1	017.0	232.5	27.0	1.000128
28550.0	913.5	-1.9	27.0	11.4	770.7	016.0	231.5	27.0	1.000129
28540.0	913.6	-1.9	27.0	11.1	771.4	015.0	230.5	27.0	1.000130
28530.0	913.7	-1.9	27.0	10.8	772.1	014.0	229.5	27.0	1.000131
28520.0	913.8	-1.9	27.0	10.5	772.7	013.0	228.5	27.0	1.000132
28510.0	913.9	-1.9	27.0	10.2	773.4	012.0	227.5	27.0	1.000133
28500.0	914.0	-1.9	27.0	9.9	774.0	011.0	226.5	27.0	1.000134
28490.0	914.1	-1.9	27.0	9.6	774.7	010.0	225.5	27.0	1.000135
28480.0	914.2	-1.9	27.0	9.3	775.4	009.0	224.5	27.0	1.000136
28470.0	914.3	-1.9	27.0	9.0	776.1	008.0	223.5	27.0	1.000137
28460.0	914.4	-1.9	27.0	8.7	776.7	007.0	222.5	27.0	1.000138
28450.0	914.5	-1.9	27.0	8.4	777.4	006.0	221.5	27.0	1.000139
28440.0	914.6	-1.9	27.0	8.1	778.1	005.0	220.5	27.0	1.000140
28430.0	914.7	-1.9	27.0	7.8	778.7	004.0	219.5	27.0	1.000141
28420.0	914.8	-1.9	27.0	7.5	779.4	003.0	218.5	27.0	1.000142
28410.0	914.9	-1.9	27.0	7.2	780.1	002.0	217.5	27.0	1.000143
28400.0	915.0	-1.9	27.0	6.9	780.7	001.0	216.5	27.0	1.000144
28390.0	915.1	-1.9	27.0	6.6	781.4	000.0	215.5	27.0	1.000145
28380.0	915.2	-1.9	27.0	6.3	782.1	000.0	214.5	27.0	1.000146
28370.0	915.3	-1.9	27.0	6.0	782.7	000.0	213.5	27.0	1.000147
28360.0	915.4	-1.9	27.0	5.7	783.4	000.0	212.5	27.0	1.000148
28350.0	915.5	-1.9	27.0	5.4	784.0	000.0	211.5	27.0	1.000149
28340.0	915.6	-1.9	27.0	5.1	784.7	000.0	210.5	27.0	1.000150
28330.0	915.7	-1.9	27.0	4.8	785.4	000.0	209.5	27.0	1.000151
28320.0	915.8	-1.9	27.0	4.5	786.1	000.0	208.5	27.0	1.000152
28310.0	915.9	-1.9	27.0	4.2	786.7	000.0	207.5	27.0	1.000153
28300.0	916.0	-1.9	27.0	3.9	787.4	000.0	206.5	27.0	1.000154
28290.0	916.1	-1.9	27.0	3.6	788.1	000.0	205.5	27.0	1.000155
28280.0	916.2	-1.9	27.0	3.3	788.7	000.0	204.5	27.0	1.000156
28270.0	916.3	-1.9	27.0	3.0	789.4	000.0	203.5	27.0	1.000157
28260.0	916.4	-1.9	27.0	2.7	790.1	000.0	202.5	27.0	1.000158
28250.0	916.5	-1.9	27.0	2.4	790.7	000.0	201.5	27.0	1.000159
28240.0	916.6	-1.9	27.0	2.1	791.4	000.0	200.5	27.0	1.000160
28230.0	916.7	-1.9	27.0	1.8	792.1	000.0	199.5	27.0	1.000161
28220.0	916.8	-1.9	27.0	1.5	792.7	000.0	198.5	27.0	1.000162
28210.0	916.9	-1.9	27.0	1.2	793.4	000.0	197.5	27.0	1.000163
28200.0	917.0	-1.9	27.0	0.9	794.0	000.0	196.5	27.0	1.000164
28190.0	917.1	-1.9	27.0	0.6	794.7	000.0	195.5	27.0	1.000165
28180.0	917.2	-1.9	27.0	0.3	795.4	000.0	194.5	27.0	1.000166
28170.0	917.3	-1.9	27.0	0.0	796.1	000.0	193.5	27.0	1.000167
28160.0	917.4	-1.9	27.0	-0.3	796.7	000.0	192.5	27.0	1.000168
28150.0	917.5	-1.9	27.0	-0.6	797.4	000.0	191.5	27.0	1.000169
28140.0	917.6	-1.9	27.0	-0.9	798.1	000.0	190.5	27.0	1.000170
28130.0	917.7	-1.9	27.0	-1.2	798.7	000.0	189.5	27.0	1.000171
28120.0	917.8	-1.9	27.0	-1.5	799.4	000.0	188.5	27.0	1.000172
28110.0	917.9	-1.9	27.0	-1.8	800.1	000.0	187.5	27.0	1.000173
28100.0	918.0	-1.9	27.0	-2.1	800.7	000.0	186.5	27.0	1.000174
28090.0	918.1	-1.9	27.0	-2.4	801.4	000.0	185.5	27.0	1.000175
28080.0	918.2	-1.9	27.0	-2.7	802.1	000.0	184.5	27.0	1.000176
28070.0	918.3	-1.9	27.0	-3.0	802.7	000.0	183.5	27.0	1.000177
28060.0	918.4	-1.9	27.0	-3.3	803.4	000.0	182.5	27.0	1.000178
28050.0	918.5	-1.9	27.0	-3.6	804.0	000.0	181.5	27.0	1.000179
28040.0	918.6	-1.9	27.0	-3.9	804.7	000.0	180.5	27.0	1.000180
28030.0	918.7	-1.9	27.0	-4.2	805.4	000.0	179.5	27.0	1.000181
28020.0	918.8	-1.9	27.0	-4.5	806.1	000.0	178.5	27.0	1.000182
28010.0	918.9	-1.9	27.0	-4.8	806.7	000.0	177.5	27.0	1.000183
28000.0	919.0	-1.9	27.0	-5.1	807.4	000.0	176.5	27.0	1.000184
27990.0	919.1	-1.9	27.0	-5.4	808.1	000.0	175.5	27.0	1.000185
27980.0	919.2	-1.9	27.0	-5.7	808.7	000.0	174.5	27.0	1.000186
27970.0	919.3	-1.9	27.0	-6.0	809.4	000.0	173.5	27.0	1.000187
27960.0	919.4	-1.9	27.0	-6.3	810.1	000.0	172.5	27.0	1.000188
27950.0	919.5	-1.9	27.0	-6.6	810.7	000.0	171.5	27.0	1.000189
27940.0	919.6	-1.9	27.0	-6.9	811.4	000.0	170.5	27.0	1.000190
27930.0	919.7	-1.9	27.0	-7.2	812.1	000.0	169.5	27.0	1.000191
27920.0	919.8	-1.9	27.0	-7.5	812.7	000.0	168.5	27.0	1.000192
27910.0	919.9	-1.9	27.0	-7.8	813.4	000.0	167.5	27.0	1.000193
27900.0	920.0	-1.9	27.0	-8.1	814.0	000.0	166.5	27.0	1.000194
27890.0	920.1	-1.9	27.0	-8.4	814.7	000.0	165.5	27.0	1.000195
27880.0	920.2	-1.9	27.0	-8.7	815.4	000.0	164.5	27.0	1.000196
27870.0	920.3	-1.9	27.0	-9.0	816.1	000.0	163.5	27.0	1.000197
27860.0	920.4	-1.9	27.0	-9.3	816.7	000.0	162.5	27.0	1.000198
27850.0	920.5	-1.9	27.0	-9.6	817.4	000.0	161.5	27.0	1.000199
27840.0	920.6	-1.9	27.0	-9.9	818.1	000.0	160.5	27.0	1.000200
27830.0	920.7	-1.9	27.0	-10.2	818.7	000.0	159.5	27.0	1.000201
27820.0	920.8	-1.9	27.0	-10.5	819.4	000.0	158.5	27.0	1.000202
27810.0	920.9	-1.9	27.0	-10.8	820.1	000.0	157.5	27.0	1.000203
27800.0	921.0	-1.9	27.0	-11.1	820.7	000.0	156.5	27.0	1.000204
27790.0	921.1	-1.9	27.0	-11.4	821.4	000.0	155.5	27.0	1.000205
27780.0	921.2	-1.9	27.0	-11.7	822.1	000.0	154.5	27.0	1.000206
27770.0	921.3	-1.9	27.0	-12.0	822.7	000.0	153.5	27.0	1.000207
27760.0	921.4	-1.9	27.0	-12.3	823.4	000.0	152.5	27.0	1.000208
27750.0	921.5	-1.9	27.0	-12.6	824.0	000.0	151.5	27.0	1.000209
27740.0	921.6	-1.9	27.0	-12.9	824.7	000.0	150.5	27.0	1.000210
27730.0	921.7	-1.9	27.0	-13.2	825.4	000.0	149.5	27.0	1.000211
27720.0	921.8	-1.9	27.0	-13.5	826.1	000.0	148.5	27.0	1.000212
27710.0	921.9	-1.9	27.0	-13.8	826.7	000.0	147.5	27.0	1.000213
27700.0	922.0	-1.9	27.0	-14.1	827.4	000.0	146.5	27.0	1.000214
27690.0	922.1	-1.9	27.0	-14.4	828.1	000.0	145.5	27.0	1.000215
27680.0	922.2	-1.9	27.0	-14.7	828.7	000.0	144.5	27.0	1.000216
27670.0	922.3	-1.9	27.0	-15.0	829.4	000.0	143.5	27.0	1.000217
27660.0	922.4	-1.9	27.0	-15.3	830.1	000.0	142.5	27.0	1.000218
27650.0	922.5	-1.9	27.0	-15.6	830.7	000.0	141.5	27.0	1.000219
27640.0	922.6	-1.9	27.0	-15.9	831.4	000.0	140.5	27.0	1.000220
27630.0	922.7	-1.9	27.0	-16.2	832.1	000.0</			

057M 3178 LAMARCA, RUTH
979700, JCB 3617 P
10-10-68

[illegible]

0374 5174 66661487
575700.00 4217
334014.04 4217

[illegible]

STATION ALTITUDE 4550.00 FEET MSL
21 OCT. 70
ASCENDING NO. 174

UPPER AIR DATA
2940010734
WALLMAN

WIND DIRECTION COORDINATES
575700.00 FEET F
575400.00 FEET N

BAROMETRIC PRESSURE	TEMPERATURE	REL. HUM.	DENSITY	SPEED OF	WIND DATA	WIND
INCHES	DEGREES	PERCENT	GRAMS PER CUBIC	WIND	DIRECTION	SPEED
MSL FEET	FAHRENHEIT		GRAMS PER CUBIC	WIND	DIRECTION	SPEED
4550.00	47.2	-77.2	99.9	570.0	134.0	8.7
4450.00	46.4	-78.6	99.9	570.0	250.0	7.0
4350.00	45.9	-79.9	99.9	570.0	260.0	8.0
4250.00	45.2	-80.4	99.9	570.0	260.0	10.0
4150.00	44.7	-81.3	99.9	570.0		
4050.00	44.2	-82.2	99.9	570.0		
3950.00	43.7	-83.1	99.9	570.0		
3850.00	43.2	-84.0	99.9	570.0		
3750.00	42.7	-84.9	99.9	570.0		
3650.00	42.2	-85.8	99.9	570.0		
3550.00	41.7	-86.7	99.9	570.0		
3450.00	41.2	-87.6	99.9	570.0		
3350.00	40.7	-88.5	99.9	570.0		
3250.00	40.2	-89.4	99.9	570.0		
3150.00	39.7	-90.3	99.9	570.0		
3050.00	39.2	-91.2	99.9	570.0		
2950.00	38.7	-92.1	99.9	570.0		
2850.00	38.2	-93.0	99.9	570.0		
2750.00	37.7	-93.9	99.9	570.0		
2650.00	37.2	-94.8	99.9	570.0		
2550.00	36.7	-95.7	99.9	570.0		
2450.00	36.2	-96.6	99.9	570.0		

STATION ALTITUDE 4550.00 FEET MSL
21 OCT. 70
ASCENDING NO. 174

PARATEPA LEVELS
2940010734
WALLMAN

WIND DIRECTION COORDINATES
575700.00 FEET F
575400.00 FEET N

BAROMETRIC PRESSURE	TEMPERATURE	REL. HUM.	DENSITY	SPEED OF	WIND DATA	WIND
INCHES	DEGREES	PERCENT	GRAMS PER CUBIC	WIND	DIRECTION	SPEED
MSL FEET	FAHRENHEIT		GRAMS PER CUBIC	WIND	DIRECTION	SPEED
4550.00	47.2	-77.2	99.9	570.0	134.0	8.7
4450.00	46.4	-78.6	99.9	570.0	250.0	7.0
4350.00	45.9	-79.9	99.9	570.0	260.0	8.0
4250.00	45.2	-80.4	99.9	570.0	260.0	10.0
4150.00	44.7	-81.3	99.9	570.0		
4050.00	44.2	-82.2	99.9	570.0		
3950.00	43.7	-83.1	99.9	570.0		
3850.00	43.2	-84.0	99.9	570.0		
3750.00	42.7	-84.9	99.9	570.0		
3650.00	42.2	-85.8	99.9	570.0		
3550.00	41.7	-86.7	99.9	570.0		
3450.00	41.2	-87.6	99.9	570.0		
3350.00	40.7	-88.5	99.9	570.0		
3250.00	40.2	-89.4	99.9	570.0		
3150.00	39.7	-90.3	99.9	570.0		
3050.00	39.2	-91.2	99.9	570.0		
2950.00	38.7	-92.1	99.9	570.0		
2850.00	38.2	-93.0	99.9	570.0		
2750.00	37.7	-93.9	99.9	570.0		
2650.00	37.2	-94.8	99.9	570.0		
2550.00	36.7	-95.7	99.9	570.0		
2450.00	36.2	-96.6	99.9	570.0		
2350.00	35.7	-97.5	99.9	570.0		
2250.00	35.2	-98.4	99.9	570.0		
2150.00	34.7	-99.3	99.9	570.0		
2050.00	34.2	-100.2	99.9	570.0		
1950.00	33.7	-101.1	99.9	570.0		
1850.00	33.2	-102.0	99.9	570.0		
1750.00	32.7	-102.9	99.9	570.0		
1650.00	32.2	-103.8	99.9	570.0		
1550.00	31.7	-104.7	99.9	570.0		
1450.00	31.2	-105.6	99.9	570.0		
1350.00	30.7	-106.5	99.9	570.0		
1250.00	30.2	-107.4	99.9	570.0		
1150.00	29.7	-108.3	99.9	570.0		
1050.00	29.2	-109.2	99.9	570.0		
950.00	28.7	-110.1	99.9	570.0		
850.00	28.2	-111.0	99.9	570.0		
750.00	27.7	-111.9	99.9	570.0		
650.00	27.2	-112.8	99.9	570.0		
550.00	26.7	-113.7	99.9	570.0		
450.00	26.2	-114.6	99.9	570.0		
350.00	25.7	-115.5	99.9	570.0		
250.00	25.2	-116.4	99.9	570.0		
150.00	24.7	-117.3	99.9	570.0		
50.00	24.2	-118.2	99.9	570.0		

NO AT LEAST ONE RELATIVE HUMIDITY VALUE WAS USED IN THE INTERPOLATIONS.

APPENDIX B
EVALUATION OF LOG-AMPLITUDE CORRELATION COEFFICIENT

APPENDIX B EVALUATION OF LOG-AMPLITUDE CORRELATION COEFFICIENT

COEFFICIENTS OF THE KUMMER'S FUNCTION ARE:

0.10000000 01	-0.83333333 00	-0.34722222 01
-0.43010288 02	-0.60951432 03	-0.77209147 02
-0.69357809 05	-0.54220819 06	-0.93730850 07
-0.80324703 08	-0.65598573 09	-0.49695884 10
-0.35086218 11	-0.23183201 12	-0.14177333 13
-0.84213605 15	-0.46602581 16	-0.24456949 17
-0.12203313 18	-0.56030527 20	-0.23155310 21

THE A1, A2 COEFFICIENT VALUES ARE:

0.38637033 01 0.41074568 01

X	PALL	RE	F
0.0	0.0	0.259	1.003
0.250	0.500	0.461	0.480
0.500	0.707	0.663	0.256
1.000	1.000	1.068	0.020
2.000	1.414	1.870	-0.074

X	PALL	RE	F	X	PALL	RE	F
0.0	0.0	0.259	1.003	0.059	0.240	0.305	0.799
0.000	0.010	0.259	0.993	0.063	0.250	0.309	0.787
0.000	0.020	0.259	0.995	0.068	0.260	0.313	0.775
0.001	0.030	0.260	0.991	0.073	0.270	0.318	0.764
0.002	0.040	0.260	0.995	0.078	0.280	0.322	0.752
0.003	0.050	0.261	0.993	0.084	0.290	0.327	0.743
0.004	0.060	0.262	0.973	0.090	0.300	0.331	0.729
0.005	0.070	0.263	0.966	0.096	0.310	0.336	0.716
0.006	0.080	0.264	0.959	0.102	0.320	0.341	0.704
0.008	0.090	0.265	0.951	0.109	0.330	0.347	0.692
0.010	0.100	0.267	0.943	0.116	0.340	0.352	0.680
0.012	0.110	0.269	0.934	0.123	0.350	0.358	0.667
0.014	0.120	0.270	0.923	0.130	0.360	0.363	0.655
0.017	0.130	0.272	0.916	0.137	0.370	0.369	0.643
0.020	0.140	0.275	0.903	0.144	0.380	0.375	0.631
0.023	0.150	0.277	0.896	0.152	0.390	0.381	0.619
0.026	0.160	0.279	0.886	0.160	0.400	0.388	0.606
0.029	0.170	0.282	0.875	0.168	0.410	0.394	0.594
0.032	0.180	0.285	0.865	0.176	0.420	0.401	0.582
0.036	0.190	0.288	0.854	0.185	0.430	0.408	0.573
0.040	0.200	0.291	0.844	0.194	0.440	0.415	0.558
0.044	0.210	0.294	0.832	0.203	0.450	0.422	0.546
0.048	0.220	0.298	0.821	0.212	0.460	0.430	0.534
0.053	0.230	0.301	0.810	0.221	0.470	0.437	0.522

X	P/L	RE	F	X	P/L	RE	F
0.230	0.480	0.445	0.510	1.254	1.120	1.274	-0.019
0.240	0.490	0.453	0.499	1.277	1.130	1.292	-0.043
0.250	0.500	0.461	0.486	1.300	1.140	1.310	-0.067
0.260	0.510	0.469	0.474	1.323	1.150	1.329	-0.091
0.270	0.520	0.477	0.462	1.346	1.160	1.347	-0.094
0.281	0.530	0.486	0.450	1.369	1.170	1.366	-0.057
0.292	0.540	0.494	0.439	1.392	1.180	1.385	-0.061
0.303	0.550	0.503	0.427	1.416	1.190	1.404	-0.064
0.314	0.560	0.512	0.415	1.440	1.200	1.423	-0.066
0.325	0.570	0.521	0.404	1.464	1.210	1.443	-0.069
0.336	0.580	0.530	0.393	1.488	1.220	1.462	-0.072
0.348	0.590	0.540	0.381	1.513	1.230	1.482	-0.074
0.360	0.600	0.550	0.370	1.538	1.240	1.502	-0.076
0.372	0.610	0.559	0.359	1.563	1.250	1.522	-0.079
0.384	0.620	0.569	0.348	1.588	1.260	1.542	-0.081
0.397	0.630	0.579	0.337	1.613	1.270	1.562	-0.082
0.410	0.640	0.590	0.326	1.638	1.280	1.582	-0.094
0.423	0.650	0.600	0.316	1.664	1.290	1.603	-0.085
0.436	0.660	0.611	0.305	1.690	1.300	1.624	-0.097
0.449	0.670	0.622	0.294	1.716	1.310	1.644	-0.099
0.462	0.680	0.633	0.284	1.742	1.320	1.665	-0.093
0.476	0.690	0.644	0.274	1.769	1.330	1.686	-0.091
0.490	0.700	0.655	0.264	1.796	1.340	1.708	-0.092
0.504	0.710	0.666	0.253	1.823	1.350	1.729	-0.092
0.518	0.720	0.678	0.243	1.850	1.360	1.751	-0.093
0.533	0.730	0.690	0.234	1.877	1.370	1.772	-0.094
0.548	0.740	0.702	0.224	1.904	1.380	1.794	-0.094
0.563	0.750	0.714	0.214	1.932	1.390	1.816	-0.094
0.578	0.760	0.726	0.205	1.960	1.400	1.838	-0.094
0.593	0.770	0.738	0.196	1.988	1.410	1.860	-0.094
0.608	0.780	0.751	0.186	2.016	1.420	1.883	-0.094
0.624	0.790	0.764	0.177	2.045	1.430	1.905	-0.094
0.640	0.800	0.777	0.168	2.074	1.440	1.928	-0.094
0.656	0.810	0.790	0.160	2.103	1.450	1.951	-0.094
0.672	0.820	0.803	0.151	2.132	1.460	1.973	-0.093
0.689	0.830	0.816	0.142	2.161	1.470	1.996	-0.093
0.706	0.840	0.830	0.134	2.190	1.480	2.020	-0.092
0.723	0.850	0.843	0.126	2.220	1.490	2.043	-0.091
0.740	0.860	0.857	0.118	2.250	1.500	2.066	-0.090
0.757	0.870	0.871	0.110	2.280	1.510	2.090	-0.089
0.774	0.880	0.885	0.102	2.310	1.520	2.113	-0.088
0.792	0.890	0.900	0.094	2.341	1.530	2.137	-0.087
0.810	0.900	0.914	0.087	2.372	1.540	2.161	-0.086
0.828	0.910	0.929	0.080	2.403	1.550	2.185	-0.085
0.846	0.920	0.944	0.072	2.434	1.560	2.209	-0.083
0.865	0.930	0.959	0.065	2.465	1.570	2.233	-0.082
0.884	0.940	0.974	0.058	2.496	1.580	2.258	-0.081
0.903	0.950	0.989	0.052	2.528	1.590	2.282	-0.079
0.922	0.960	1.005	0.045	2.560	1.600	2.307	-0.077
0.941	0.970	1.020	0.039	2.592	1.610	2.332	-0.076
0.960	0.980	1.036	0.032	2.624	1.620	2.356	-0.074
0.980	0.990	1.052	0.026	2.657	1.630	2.381	-0.072
1.000	1.000	1.068	0.020	2.690	1.640	2.406	-0.073
1.020	1.010	1.085	0.014	2.723	1.650	2.432	-0.069
1.040	1.020	1.101	0.009	2.756	1.660	2.457	-0.067
1.061	1.030	1.118	0.003	2.789	1.670	2.482	-0.065
1.082	1.040	1.134	-0.002	2.822	1.680	2.508	-0.063
1.103	1.050	1.151	-0.007	2.856	1.690	2.533	-0.061
1.124	1.060	1.168	-0.012	2.890	1.700	2.559	-0.059
1.145	1.070	1.186	-0.017	2.924	1.710	2.585	-0.057
1.166	1.080	1.203	-0.022	2.958	1.720	2.611	-0.055
1.188	1.090	1.220	-0.027	2.993	1.730	2.637	-0.053
1.210	1.100	1.238	-0.031	3.028	1.740	2.663	-0.050
1.232	1.110	1.256	-0.035	3.063	1.750	2.689	-0.048

X	PALL	RE	F	X	PALL	RE	F
3.098	1.760	2.716	-0.046	5.712	2.390	4.545	0.013
3.133	1.770	2.742	-0.044	5.760	2.400	4.577	0.012
3.168	1.780	2.768	-0.042	5.808	2.410	4.608	0.011
3.204	1.790	2.795	-0.040	5.856	2.420	4.640	0.010
3.240	1.800	2.822	-0.038	5.905	2.430	4.672	0.010
3.276	1.810	2.849	-0.035	5.954	2.440	4.704	0.009
3.312	1.820	2.876	-0.033	6.003	2.450	4.736	0.008
3.348	1.830	2.903	-0.031	6.052	2.460	4.769	0.007
3.384	1.840	2.930	-0.029	6.101	2.470	4.800	0.006
3.421	1.850	2.957	-0.027	6.150	2.480	4.832	0.005
3.456	1.860	2.984	-0.025	6.200	2.490	4.864	0.005
3.492	1.870	3.011	-0.023	6.250	2.500	4.897	0.004
3.534	1.880	3.039	-0.021	6.300	2.510	4.929	0.003
3.572	1.890	3.066	-0.019	6.350	2.520	4.961	0.002
3.610	1.900	3.094	-0.017	6.401	2.530	4.994	0.001
3.649	1.910	3.122	-0.015	6.452	2.540	5.027	0.000
3.686	1.920	3.150	-0.013	6.503	2.550	5.060	-0.001
3.725	1.930	3.178	-0.011	6.554	2.560	5.093	-0.002
3.764	1.940	3.206	-0.010	6.605	2.570	5.126	-0.002
3.803	1.950	3.234	-0.008	6.656	2.580	5.159	-0.003
3.842	1.960	3.262	-0.006	6.708	2.590	5.192	-0.004
3.881	1.970	3.290	-0.005	6.760	2.600	5.225	-0.005
3.920	1.980	3.319	-0.003	6.812	2.610	5.258	-0.006
3.960	1.990	3.347	-0.001	6.864	2.620	5.292	-0.006
4.000	2.000	3.375	0.000	6.917	2.630	5.325	-0.007
4.040	2.010	3.403	0.002	6.970	2.640	5.359	-0.008
4.080	2.020	3.432	0.003	7.023	2.650	5.393	-0.009
4.121	2.030	3.461	0.004	7.076	2.660	5.426	-0.009
4.162	2.040	3.490	0.006	7.129	2.670	5.460	-0.010
4.203	2.050	3.519	0.007	7.182	2.680	5.494	-0.010
4.244	2.060	3.548	0.008	7.236	2.690	5.528	-0.011
4.285	2.070	3.577	0.009	7.290	2.700	5.563	-0.012
4.326	2.080	3.606	0.010	7.344	2.710	5.597	-0.012
4.367	2.090	3.635	0.011	7.398	2.720	5.631	-0.013
4.410	2.100	3.664	0.012	7.453	2.730	5.666	-0.013
4.452	2.110	3.693	0.013	7.507	2.740	5.700	-0.013
4.494	2.120	3.722	0.014	7.563	2.750	5.735	-0.014
4.537	2.130	3.752	0.014	7.618	2.760	5.770	-0.014
4.580	2.140	3.782	0.015	7.673	2.770	5.804	-0.014
4.623	2.150	3.811	0.016	7.728	2.780	5.839	-0.015
4.666	2.160	3.841	0.016	7.784	2.790	5.874	-0.015
4.709	2.170	3.871	0.017	7.840	2.800	5.909	-0.015
4.752	2.180	3.901	0.017	7.896	2.810	5.945	-0.015
4.796	2.190	3.931	0.017	7.952	2.820	5.980	-0.015
4.840	2.200	3.961	0.018	8.009	2.830	6.015	-0.015
4.884	2.210	3.991	0.018	8.066	2.840	6.051	-0.015
4.928	2.220	4.021	0.018	8.123	2.850	6.086	-0.015
4.973	2.230	4.051	0.018	8.180	2.860	6.123	-0.015
5.018	2.240	4.081	0.018	8.237	2.870	6.158	-0.015
5.063	2.250	4.112	0.018	8.294	2.880	6.194	-0.015
5.108	2.260	4.142	0.019	8.352	2.890	6.230	-0.015
5.153	2.270	4.173	0.019	8.410	2.900	6.266	-0.015
5.198	2.280	4.203	0.019	8.468	2.910	6.302	-0.015
5.244	2.290	4.234	0.017	8.526	2.920	6.338	-0.015
5.290	2.300	4.265	0.017	8.585	2.930	6.374	-0.016
5.336	2.310	4.296	0.017	8.644	2.940	6.411	-0.016
5.382	2.320	4.327	0.016	8.703	2.950	6.447	-0.016
5.429	2.330	4.358	0.016	8.762	2.960	6.484	-0.016
5.476	2.340	4.389	0.016	8.821	2.970	6.520	-0.016
5.523	2.350	4.420	0.015	8.880	2.980	6.557	-0.016
5.570	2.360	4.451	0.014	8.940	2.990	6.593	-0.016
5.617	2.370	4.482	0.014	9.000	3.000	6.630	-0.016
5.664	2.380	4.514	0.013				

05/02/72 15-49

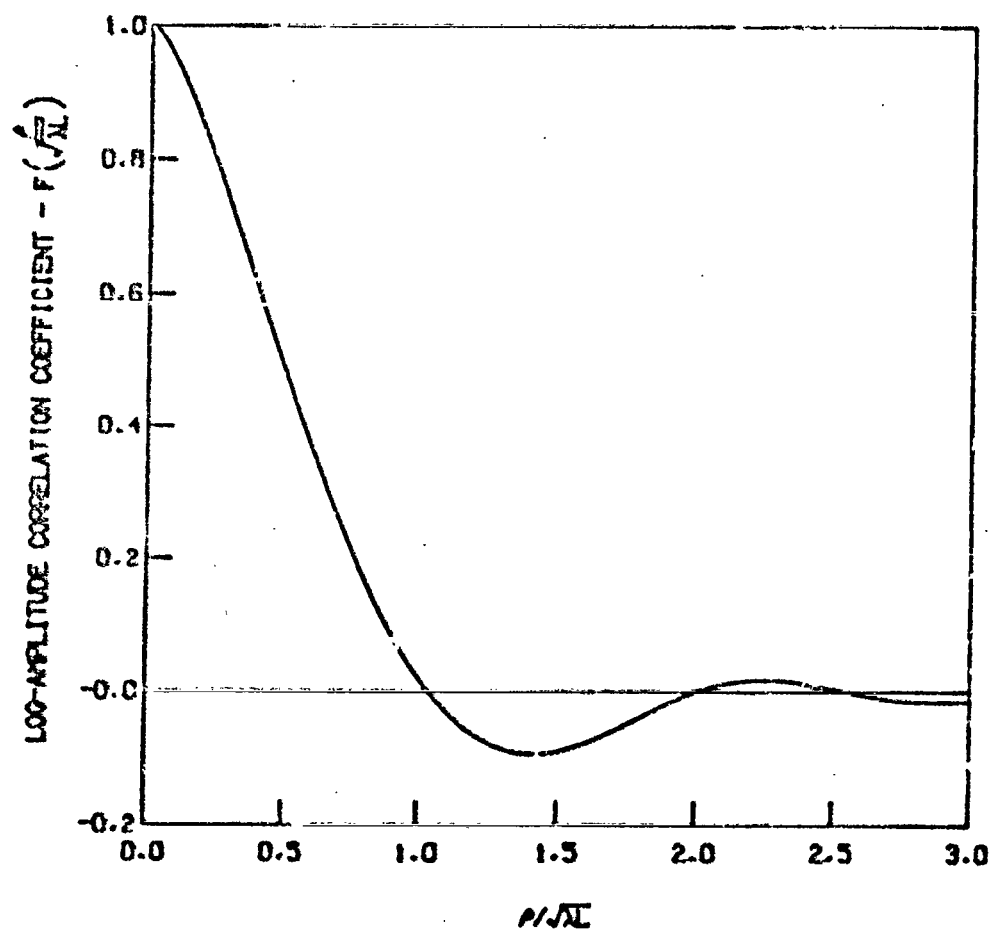


Figure B-1

END

DATE

FILMED

SEP 21 1972